DOCTORAL THESIS

SIMULATION METHODS FOR DURABILITY ASSESSMENT OF CONCRETE STRUCTURES: MULTIFIELD FRAMEWORK AND STRONG DISCONTINUITY EMBEDDED APPROACH

submitted in satisfaction of the requirements for the degree of
Doctor of Science in Civil Engineering
of the Vienna University of Technology, Faculty of Civil Engineering

---

DISSERTATION

BERECHNUNGSMETHODEN FÜR DIE BEWERTUNG DER DAUERHAFTIGKEIT VON BETONSTRUKTUREN: MEHRFELDANSATZ UND EINGEBETTETE, DISKRETE DISKONTINUITÄTEN

ausgeführt zum Zweck der Erlangung des akademischen Grades eines
Doktors der technischen Wissenschaften
eingereicht an der Technischen Universität Wien, Fakultät für Bauingenieurwesen

von

MSc. Yiming Zhang
Matrikelnummer: 0928631
Technikerstraße 19a, 6020 Innsbruck, Österreich

Gutachter: Univ.-Prof. Dipl.-Ing. Dr. techn. Roman Lackner
Materialtechnologie Innsbruck
Universität Innsbruck
Technikerstraße 13, 6020 Innsbruck, Österreich

Gutachter: em.O.Univ.-Prof. Dipl.-Ing. Dr. techn. Dr. h.c.mult. Herbert Mang, Ph.D.
Institut für Mechanik der Werkstoffe und Strukturen
Technische Universität Wien
Karlsplatz 13/202, 1040 Wien, Österreich

Wien, im November 2013 .....

”All is a riddle, and the key to a riddle...is another riddle.”
Ralph Waldo Emerson

Acknowledgements

This thesis is the outcome of my research activities as a university researcher, first at the Institute for Mechanics of Materials and Structures (IMWS) of Vienna University of Technology (TUWien), and then at Material-Technology Innsbruck (MTI) of the University of Innsbruck (UIBK). It would have been an impossible task without the support of the following individuals and organizations.

First of all, I want to thank my wife Qiong and my daughter Weina, who have always supported me during my doctoral studies.

I would like to thank Prof. Herbert A. Mang whose knowledge, patience and enthusiasm in research have encouraged me to pursue my research career in Austria.

I am very thankful to Dr. Matthias Zeiml, who always guided me in my research. His deep understanding of fire-loaded concrete, both experimentally and numerically, always inspired not only me but also our whole research group.

I wish to thank Prof. Roman Lackner, who guided me from the macroscopic world to the microscopic universe. His knowledge in plasticity has helped me to pass the jungle of the strong discontinuity embedded approach (SDA) and stress locking, and to find the way to numerical analysis of fracture of concrete.

Many thanks are due to Dr. Christian Pichler, who provided me with a code for multiscale homogenization of early-age concrete and explained the guidelines for working with this code.

I am very grateful to my former colleagues Dr. Aram Amouzandeh and Dr. Thomas Ring of Vienna University of Technology, who shared a big office at the laboratory of IMWS with me for two years. I could always turn to them when I could not solve my problems.

Special thanks go to Prof. Josef Eberhardsteiner and Associate Prof. Bernhard Pichler, who made me focus on my timetable and work efficiently.

Regarding administrative support, I would like to thank: Mag. Martina Pöll, Ms. Gabriele Ostrowski, and Ms. Astrid Schuh from IMWS and Ms. Sabine Riml from MTI.

I gratefully acknowledge financial support by the China Scholarship Coun-

cil and by the Austrian Ministry for Transport, Innovation and Technology (bm.vit) within the KIRAS-project (Austrian security research program) 813794 ”Sicherheit von Hohlraumbauten unter Feuerlast” (”Safety of underground structures under fire loading”).

Last, but not least, I appreciate the selfless help from the research group of MUMPS (MUltifrontal Massively Parallel sparse direct Solver), which allowed me to use their compute program for my work. Without their solver, all simulations would take at least five times longer.

Kurzfassung

Die Dauerhaftigkeit von Betonstrukturen steht in engem Zusammenhang mit (i) dem Massetransport im Zuge von thermischer Belastung und/oder chemischem Angriff und (ii) dem mechanischem Versagen durch Ermüdung oder Rissbildung. Generell sind Massetransport und mechanisches Versagen nicht unabhängig voneinander, wobei das Ausmaß der Wechselwirkung von den jeweiligen Zeit- und Längenmaßstäben abhängt. Simulationsmodelle zur Untersuchung der Dauerhaftigkeit von Betonstrukturen sollten diese Prozesse, aber auch deren Wechselwirkung, numerisch reproduzieren können. Das Ziel dieser Arbeit ist die Entwicklung eines zuverlässigen numerischen Modells, basierend auf der Methode der finiten Elemente, mittels denen Dauerhaftigkeitsprobleme in Betonstrukturen simuliert werden können. Im Detail werden numerische Techniken für die Untersuchung von drei verschiedenen Dauerhaftigkeitsproblemen präsentiert:

- Beton jungen Alters:

  Für Beton jungen Alters wird das Konzept der Mehrskalenmodellierung in ein Mehrphasenmodell zur Simulation von Transportprozessen implementiert, das den Wasser-Zement-Wert als Eingangsgröße erfordert und die zeitliche Veränderung der Materialparameter als Funktion des Hydratationsgrads berücksichtigt. Das präsentierte mikromechanik-basierte Mehrphasenmodell für Beton jungen Alters wird auf die Beurteilung des Rissrisikos von Betonstrukturen mit unterschiedlicher Dicke angewendet.

- Beton unter Brandbelastung:

  Die Dehydratation in temperaturbelastetem Beton wird als Umkehr der Hydratation betrachtet. Dadurch wird die Beschreibung der zeitlichen Veränderung des Biot-Koeffizienten möglich. Für Simulationen brandbelasteter Bauteile wird ein axisymmetrisches Modell betrachtet, das flächige Bauteile wie Platten, Wände und Tunnelschalen repräsentiert. Das zugrunde gelegte Mehrphasenmodell wird zur Bestimmung des Abplatzrisikos von Betonstrukturen verwendet, wobei der Einfluss der Permeabilität und des Sättigungsgrades des Betons auf das Abplatzrisiko untersucht wird.

- Rissbildung:

  Die durch einen Riss induzierten Unstetigkeiten im Verschiebungsverlauf werden mittels des “strong discontinuity embedded approach” auf der Ebene der Finiten Elemente berücksichtigt, die sich wiederum durch quadratische Ansatzfunktionen, die für die Beschreibung von Transportprozessen erforderlich sind, auszeichnen. Für die Bestimmung der Rissausbreitung wird eine energie-basierte Methode vorgestellt, wodurch künstliche Versteifungseffekte (“locking”) vermieden werden. Der präsentierte Ansatz wird anhand von Nachrechnungen eines Dreipunkt-Biegeversuchs, eines L-förmigen Bauteils und eines Bolzen-Ausziehversuchs validiert.

Schlussendlich bilden das präsentierte Mehrskalenmodell und der Ansatz für die Beschreibung der Rissbildung die Basis für Simulationen, die Rissbildung und Massetransport sowie deren Wechselwirkung berücksichtigen. Das Potential der Kombination der entwickelten Ansätze ist anhand eines L-förmigen Bauteils illustriert, der sowohl mechanischer Belastung wie auch einer Gasdruckbelastung ausgesetzt ist.

Abstract

Durability of concrete structures is closely associated with i) the mass-transport process, resulting from thermal loading and/or leading to chemical attack, and ii) the mechanical failure caused by fatigue and fracturing. In general, these two processes interact with each other, depending on the time and length scale of their occurrence. Accordingly, simulation tools for durability assessment of concrete structures should be capable of numerically reproducing these processes as well as capturing the interactions among them.

The aim of this thesis is to develop a reliable numerical tool, based on the finite element method, which is able to simulate and solve durability problems observed in concrete structures. More specifically, numerical techniques for three investigations of concrete durability will be presented. They are as follows:

- Early-age concrete:

  For early-age concrete, multiscale homogenization is introduced into the multifield framework, which requires the water cement ratio as an input parameter and provides material parameters as functions of the hydration degree for the multifield framework. The presented micromechanics-based multifield framework for early-age concrete is adopted for the assessment of the cracking risk of early-age concrete structures with different thickness.

- Fire-loaded concrete:

  For concrete at high temperature, dehydration as the reverse reaction of hydration is introduced, giving access to Biot's coefficient. Further, an axisymmetric model, representing plate-like concrete structures such as slabs, walls and tunnel linings, is considered together with a corresponding damage criterion. The underlying multifield framework is used for an assessment of the spalling risk of concrete structures, considering different values of intrinsic permeability and initial saturation degree.

- Fracturing:

For fracturing of concrete, a strong discontinuity embedded approach for a higher-order element (eight-node quadrilateral element) is developed, considering an energy-based crack-tracking strategy in order to avoid stress-locking. The presented approach is validated by means of a three-point bending test, an L-shaped panel test, and a pull-out test.

Finally, the presented multifield framework and strong discontinuity embedded approach provides the basis for simulation of fracture-permeation problems. This kind of simulation is illustrated by an L-shaped panel, subjected to both mechanical and gas-pressure loading, which demonstrates the potential of the developed approach.

Contents

List of symbols

Multifield framework:

b	[-]	Biot's coefficient
c_p	[J kg^{-1} K^{-1}]	heat capacity of concrete
c_p^g, c_p^w, c_p^s	[J kg^{-1} K^{-1}]	heat capacity of gas, water, solid part of concrete
$\mathbb{C}^{hom}$	[MPa]	homogenized elastic stiffness tensor
D^{eff}	[m^2 s^{-1}]	effective diffusivity of concrete
E	[MPa]	Young's modulus of concrete
f_x	[-]	volume fraction of component x
f_t, f_c	[MPa]	tensile and compressive strength of concrete
h	[J kg^{-1}]	specific enthalpy of vaporization
$\mathbf{1}$	[-]	second-order unity tensor
$\mathbf{k}$	[m^2]	intrinsic-permeability tensor of concrete
K^{hom}, K^s	[MPa]	homogenized bulk modulus and bulk modulus of solid part
k^{rg}, k^{rw}	[-]	relative permeability of gas and liquid phase
l_ξ	[J kg^{-1}]	hydration heat per unit mass of hydration products
$\dot{m}_{vap}$	[kg m^{-3} s^{-1}]	change of vapor mass (rate) per unit volume concrete
$\dot{m}$	[kg m^{-3} s^{-1}]	change of mass (rate) of hydration/dehydration products per unit volume concrete
M_a, M_w, M_g	[kg mol^{-1}]	molar mass of dry air, water, gas mixture
n	[-]	porosity of concrete
p^g, p^w, p^c	[Pa]	gas, water, capillary pressure of concrete
p^{ga}, p^{gw}	[Pa]	air partial pressure and vapor partial pressure in gas
R	[J mol $^{-1}$ K $^{-1}$]	universal constant for ideal gases
S_w	[-]	saturation degree of pores in concrete
T	[K]	absolute temperature in concrete
β_s	[K^{-1}]	thermal expansion coefficient of solid part of concrete
λ, λ^{eff}	[J s^{-1} m^{-1} K^{-1}]	thermal conductivity and effective thermal conductivity coefficient of concrete
ξ	[-]	hydration degree
η^g, η^w	[Pa s]	viscosity of gas, water phase
ρ^g, ρ^w, ρ^s	[kg m^{-3}]	density of gas, water, solid part of concrete
ρ^{ga}, ρ^{gw}	[kg m^{-3}]	density of dry air and water vapor
$\mathbf{E}$	[-]	macroscopic strain tensor
$\mathbf{E}^e$	[-]	macroscopic elastic strain tensor
$\mathbf{E}^T$	[-]	thermal strain tensor
$\mathbf{\Sigma}$	[MPa]	macroscopic stress tensor

Early-age concrete:

$\tilde{A}$	[s^{-1}]	chemical affinity of hydration reaction
a, b, c	[s^{-1}],[-],[-]	parameters defining $\tilde{A}$
E_a	[J mol^{-1}]	activation energy of hydration process
$f_{t,\infty}, f_{c,\infty}$	[MPa]	tensile and compressive strength of mature concrete
$\mathscr{L}$	[m]	structural dimension of heat diffusion
$p_{satb}, p_{sat\infty}$	[Pa]	saturation vapor pressure at the boundary of concrete and in the environment
Rh_b, Rh_∞	[-]	relative humidity at the boundary of concrete and in the environment
S	[-]	moisture boundary coefficient considering surface cover
T_b, T_∞	[K]	temperature at the boundary of concrete and in the environment
v	[m s^{-1}]	wind speed
α_T	[J s^{-1} m^{-2} K^{-1}]	convection coefficient
α_V	[J s^{-1} m^{-2} K^{-1}]	equivalent convection coefficient caused by vaporization
ξ_0	[-]	percolation threshold

Concrete subjected to fire loading:

$f_{t,0}, f_{c,0}$	[MPa]	initial tensile and compressive strength of concrete
f_b	[MPa]	biaxial compression strength of concrete
k^{lits}	[-]	load-induced thermal strain (LITS) parameter
$\mathbf{E}^{LITS}$	[-]	load-induced thermal strain tensor

Strong discontinuity approach:

$\mathbb{C}$	[MPa]	original elastic stiffness tensor
$\mathbb{C}^{eq}$	[MPa]	equivalent stiffness tensor considering crack opening
G_f	[N m^{-1}]	fracture energy of concrete
$\mathbf{n}$	[-]	unit vector perpendicular to crack surface
$\mathbf{t}$	[-]	unit vector parallel to crack surface (2D condition)
T_{eq}	[MPa]	equivalent traction component
T_n, T_t	[MPa]	traction component along $\mathbf{n}$ and $\mathbf{t}$
Ψ	[J]	total energy of deformed body
U	[J]	elastic strain energy of deformed body
W	[J]	work done by the applied load on the deformed body
E	[J]	dissipated energy of the deformed body
β	[-]	parameter governing the contributions of Mode I and Mode II crack opening
ζ_n, ζ_t	[m]	crack opening (width) along $\mathbf{n}$ and $\mathbf{t}$

1 Introduction

1.1 Background

Durability of concrete structures is associated with physical/chemical processes within the concrete material. These processes include deformation, permeation, diffusion, conduction, hydration/dehydration, and fracture, which may be grouped into: i) mass-transport processes and ii) mechanical processes:

- On one hand, considering the mass-transport process inside concrete, the micro-structure of which is illustrated in Figure 1, a numerical model which is capable of simulating the mass-transport process evolving in porous materials is modified and adopted for simulating this process in concrete. Not only general properties of porous materials such as the porosity, the saturation degree, but also properties of cementious materials changing with time in consequence of hydration/dehydration, shall be taken into account. Aiming to simulate the mass-transport process of concrete, a coupled thermo-hydro-chemo-poro-mechanical multifield framework will be presented in this thesis.

- On the other hand, considering fracture processes associated with mechanical loading, concrete exhibits typical quasi-brittle behaviour (the post strength response is characterized by increased deformations with decreasing capability of stress transfer as a result of localization of damage [1]). Plastic deformations within concrete show strong discontinuity characteristics, which can be appropriately modelled by crack-embedded approaches, such as the strong discontinuity embedded approach and the extended finite element method, where material properties such as the fracture energy and yield strength are taken into account. Aiming to simulate the elasto-plastic behaviour and fracture properties (crack position and orientation, crack opening) of concrete, a strong discontinuity embedded approach will be presented in this thesis.

The multifield framework and the strong discontinuity embedded approach, presented in this thesis, are applied to the following engineering tasks associated with concrete durability:

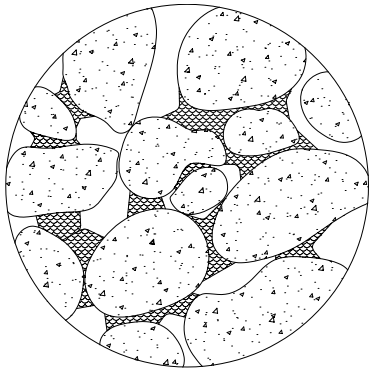

Figure 1: Illustration of micro-structure of concrete: solid skeleton and non-saturated pores

- drying shrinkage of early-age concrete,
- spalling of concrete subjected to high temperature,
- fracturing of concrete members.

The combination of both the multifield framework and the strong-discontinuity embedded approach, as illustrated numerically, considering an L-shaped panel with gas permeation, provides the basis for future investigations of durability problems, considering coupled transport-fracturing processes.

1.2 Outline

The thesis is organized as follows:

- In Section 2, a coupled thermo-hydro-chemo-poro-mechanical multifield framework for porous materials, considering multiscale homogenization will be presented. Modifications of the underlying model formulation, suitable for the analysis of early-age concrete and fire-loaded concrete, will be introduced.
- In Section 3, a strong discontinuity embedded model for higher-order finite element will be presented. An energy-based crack-tracking strategy, originally developed and applied in the frame of XFEM, will be modified and implemented into the model.

- In Section 4, results from engineering applications concerning the durability of concrete structures, such as drying shrinkage of early-age concrete, spalling of concrete subjected to high temperature, and fracturing of concrete members will be presented.
- In Section 5, conclusions from this work will be drawn. An L-shaped panel, experiencing fracturing and gas permeation, will be simulated, showing the potential of the multifield framework combined with the strong-discontinuity approach.

2 Coupled thermo-hydro-chemo-poro-mechanical multifield framework for porous materials

2.1 Background

The behaviour of concrete is greatly influenced by physical and chemical processes inside this material. These processes include permeation, diffusion, conduction, vaporization/condensation (phase change), hydration/dehydration and deformation. Analysis schemes considering these processes in a coupled manner are referred to as multifield methods. The development of multifield methods for porous media mainly started in mid 1990s, corresponding with a period of great improvements in the field of computational mechanics. As regards the analysis of concrete, several multifield analysis models have been applied to the investigation of early-age concrete and of fire-loaded concrete, which are the main issues of this section.

For early-age concrete, multifield analysis models proposed in the literature mainly focus on thermo-chemical coupling [2, 3, 4] and fluid transport [5, 6, 7]. After treatment of thermo-chemical coupling and solution of the transport problem, the total strain theory [5] and the effective stress theory [8, 9] are used to solve the underlying mechanical problem. Concerning applications, the resulting weakly-coupled multifield models enable treatment of thermo-chemical processes, mass-transport processes (which are not always considered), and of the mechanical problem, where frequently mass-transport processes and/or the impact of mass-transport on the temperature field are ignored [10]. More recently, fully-coupled analysis tools, based on thermo-hydro-chemo-mechanical models, were developed [11]. Both weakly-coupled and fully-coupled approaches have been validated and proved to be effective for different types of concrete such as normal concrete (OPC) as well as high performance concrete (HPC) [11, 12]. Whereas the former is more efficient, the latter may be applied to open systems (concrete directly bare to air).

For fire-loaded concrete, multifield models adopted by previous researchers mainly focus on thermo-mechanical [13, 14] and thermo-hydral processes [15, 16, 17], which are the main causes for spalling. Some models of different levels of complexity were presented in [18, 19, 20, 21, 22]. For simplicity, in some numerical models only the gas phase [15] or two phases (liquid and gas, gas

and solid) are considered [21, 23] or an additional constitutive relationship between the gas and the liquid phase [22] is introduced, leading to unreliable results in some applications, as was pointed out in [24]. Hence, a fully-coupled model, considering heat conduction, permeation and diffusion of gas and water and all relevant phase changes is necessary to realistically simulate the thermo-hydral processes that take place in fire-loaded concrete.

In this section, based on the model described in [9, 11, 25, 26, 27, 28, 29], a coupled thermo-hydro-chemo-poro-mechanical multifield framework is proposed, which represents a combination of a fully-coupled multifield model and a multiscale model. The model is presented in a form which is suitable for both early-age concrete and fire-loaded concrete.

2.2 Thermo-hydro-chemical model

2.2.1 Balance equations

The thermo-hydro-chemical model adopted in this thesis was presented e.g. in [9, 11, 25, 26, 27, 28, 29]. In this model, concrete is treated as a multi-phase medium, consisting of a solid, liquid (water), and gas (water vapor and dry air) phase. The governing equations are based on mass and energy conservation, with p^c, p^g, and T as unknowns. These equations read as follows:

- Mass-balance equation for the water phase:

$$
\begin{aligned}
& n(\rho^w - \rho^{gw})\frac{D^s S_w}{Dt} + n(1-S_w)\frac{D^s \rho^{gw}}{Dt} + nS_w\frac{D^s \rho^w}{Dt} \\
& - (1-n)\beta_s\left[\rho^{gw} + (\rho^w - \rho^{gw})S_w\right]\frac{D^s T}{Dt} \\
& - \operatorname{div}\left(\rho^{gw}\frac{\mathbf{k}k^{rg}}{\eta^g}\operatorname{grad}\, p^g\right) - \operatorname{div}\left(\rho^{w}\frac{\mathbf{k}k^{rw}}{\eta^w}\operatorname{grad}\, p^w\right) \\
& - \operatorname{div}\left[\rho^g\frac{M_a M_w}{M_g^2}\mathbf{D}_{eff}\operatorname{grad}\,\left(\frac{p^{gw}}{p^g}\right)\right] \\
& + \frac{(1-n)[\rho^{gw}(1-S_w) + \rho^w S_w]}{\rho^s}\frac{\partial \rho^s}{\partial \xi}\frac{D^s \xi}{Dt} \\
& + [\rho^{gw}(1-S_w) + \rho^w S_w]\frac{\dot{m}}{\rho^s} - \dot{m} = 0.
\end{aligned}
\tag{1}
$$

- Mass-balance equation for the dry-air phase:

$$
\begin{aligned}
&- n\rho^{ga}\frac{D^sS_w}{Dt} + n(1-S_w)\frac{D^s\rho^{ga}}{Dt} - \rho^{ga}(1-n)(1-S_w)\beta_s\frac{D^sT}{Dt} \\
&- \operatorname{div}\left(\rho^{ga}\frac{\mathbf{k}k^{rg}}{\eta^g}\operatorname{grad}\, p^g\right) - \operatorname{div}\left[\rho^g\frac{M_aM_w}{M_g^2}\mathbf{D}_{eff}\operatorname{grad}\,\left(\frac{p^{ga}}{p^g}\right)\right] \\
&+ \frac{(1-n)\rho^{ga}(1-S_w)}{\rho^s}\frac{\partial\rho^s}{\partial\xi}\frac{D^s\xi}{Dt} + \rho^{ga}(1-S_w)\frac{\dot{m}}{\rho^s} = 0.
\end{aligned}
\tag{2}
$$

- Energy-balance equation:

$$
\begin{aligned}
&(\rho c_p)_{eff}\frac{\partial T}{\partial t} - \left(\rho^g c_p^g\frac{\mathbf{k}k^{rg}}{\eta^g}\operatorname{grad}\, p^g + \rho^w c_p^w\frac{\mathbf{k}k^{rw}}{\eta^w}\operatorname{grad}\, p^w\right)\operatorname{grad}\, T \\
&- \operatorname{div}(\lambda_{eff}\operatorname{grad}\, T) + \dot{m}_{vap}h + \dot{m}l_\xi^w = 0,
\end{aligned}
\tag{3}
$$

where $\dot{m}_{vap}$ is determined from

$$
\begin{aligned}
\dot{m}_{vap} &= -n\rho^w\frac{D^sS_w}{Dt} - nS_w\frac{D^s\rho^w}{Dt} + \rho^w(1-n)S_w\beta_s\frac{D^sT}{Dt} \\
&+ \operatorname{div}\left(\rho^w\frac{\mathbf{k}k^{rw}}{\eta^w}\operatorname{grad}\, p^w\right) - \frac{(1-n)\rho^wS_w}{\rho^s}\frac{\partial\rho^s}{\partial\xi}\frac{D^s\xi}{Dt} \\
&- \rho^wS_w\frac{\dot{m}}{\rho^s} + \dot{m}.
\end{aligned}
\tag{4}
$$

In the Equations (1) to (3), $\dot{m}$ denotes an increase of mass caused by hydration in early-age concrete ($\dot{m} > 0$) or a decrease of mass in case of dehydration in fire-loaded concrete ($\dot{m} < 0$).

Each term in the Equations (1) to (3) can be classified as an accumulation, a flux, or a source term. A detailed deduction of these relations and of their finite element implementation can be found in [28, 30, 31].

2.2.2 Moisture state

For determining the moisture state of concrete, it is assumed that the sorption isotherms keep the same shape throughout the hydration process [11]. A formula given in [7] is used, establishing the relationship between the capillary

pressure p^c and the saturation degree S_w [31]:

$$S_w = \left[1 + \left(\frac{E_s}{A_s} p^c\right)^{1/(1-m)}\right]^{-m},$$

with

$$\begin{cases} A_s = p_b^c & \text{for } T \leq 100°\text{C} \\ A_s = B_s + (p_b^c - B_s)\left[2\left(\frac{T-100}{T_{crit}-100}\right)^3 - 3\left(\frac{T-100}{T_{crit}-100}\right)^2 + 1\right] & \text{for } T > 100°\text{C} \end{cases}$$

and

$$\begin{cases} E_s = \left(\frac{T_{crit}-T_0}{T_{crit}-T}\right)^{N_s} & \text{for } T \leq (T_{crit} - Z_s) \\ E_s = E_{s,0}\left(\frac{N_s}{Z_s}T + 1 - \frac{N_s}{Z_s}(T_{crit} - Z_s)\right) & \text{for } T > (T_{crit} - Z_s) \\ E_{s,0} = \left(\frac{T_{crit}-T_0}{Z_s}\right)^{N_s} \end{cases}, \tag{5}$$

where p_b^c is the so-called bubbling pressure (the minimum value of p^c on a drainage capillary pressure curve, at which a continuous gas phase exists in the void space), and m is a constant parameter. As suggested in [7], for OPC, $p_b^c = 18.6$ MPa and $m = 0.44$ are chosen. For HPC, $p_b^c = 46.9$ MPa and $m = 0.48$ are taken. B_s, N_s and Z_s are constant parameters, chosen as $B_s = 30$ MPa, $N_s = 1.2$, $Z_s = 0.5$ °C, and T_{crit} is the critical temperature, taken as 374.15 °C[31].

Kelvin's equation is used for establishing the relationship between the capillary pressure p^c and the relative humidity [6, 10]:

$$\ln(\text{Rh}) = -\frac{M_w\, p^c}{\rho^w\, R\, T}. \tag{6}$$

Once the temperature is known, with Equations (5) and (6) relationships for determination of p^c, Rh, and S_w are available, giving access to the moisture state.

2.3 Thermo-chemo-poro model

2.3.1 Multiscale model for early-age concrete

The degree of hydration $\xi(t)$ of early-age concrete is determined from the volume fraction of cement in the material system, $\mathrm{f}_{cem}(t)$, related to the

respective initial volume fraction, $\mathrm{f}_{cem}^{initial} = \mathrm{f}_{cem}(t=0)$, reading $\xi(t) = 1 - \mathrm{f}_{cem}(t)/\mathrm{f}_{cem}^{initial}$. The evolution of ξ is described by an Arrhenius-type law [4, 32]:

$$\dot{\xi} = \tilde{A}(\xi)\exp\left(-\frac{E_a}{RT}\right), \tag{7}$$

where E_a/R is set equal to 4000 K [33]. A mathematical relation for the chemical affinity $\tilde{A}$ is given by $\tilde{A}(\xi) = a\xi^b(1-\xi)^c$, where a, b, c may be acquired from adiabatic tests [33]. Equation (7) accounts for thermo-chemical coupling, giving an increased hydration rate with increasing temperature, or vice versa. In this thesis, changes in pore water saturation due to drying/wetting are assumed not to affect the hydration kinetics. On the other hand, the hydration reaction cannot continue when free water is exhausted. Hence, the hydration process is assumed to stop when the saturation degree S_w drops below a certain threshold value $\overline{S_w}$, where $\overline{S_w}$ is set equal to 58.6%[1].

As an engineering approximation, the hydration of cement is represented by the hydration stoichiometry of tricalcium silicate (C_3S[2]), which is the main clinker phase in all Portland cement-based material systems [34]:

$$\mathrm{C_3S} + 5.3\,\mathrm{H} \;\rightarrow\; 0.5\,\mathrm{C_{3.4}S_2H_8} + 1.3\,\mathrm{CH}. \tag{8}$$

Using the intrinsic material properties summarized in Table 1, Equation (8) can be written as a mass balance:

$$\begin{aligned} 228 + 5.3 \times 18 \;&\rightarrow\; 0.5 \times 454 + 1.3 \times 74 \qquad \text{in [g]} \\ 323.4 \;&\rightarrow\; 323.2 \qquad \text{in [g]}, \end{aligned} \tag{9}$$

or as a volumetric balance:

$$\begin{aligned} \tfrac{228}{3.15} + 5.3\tfrac{18}{0.998} \;&\rightarrow\; 0.5\tfrac{454}{1.99} + 1.3\tfrac{74}{2.24} \qquad \text{in [cm}^3\text{]} \\ 167.97 \;&\rightarrow\; 157.02 \qquad \text{in [cm}^3\text{]}. \end{aligned} \tag{10}$$

From Equation (9), the water-to-cement mass ratio (w/c) needed for com-

[1] According to [5], hydration stops completely when the relative humidity drops below 80%, with the corresponding saturation degree being about 58.6% at 20°C (see Equation (5)). However, this threshold value does not concern the results of the numerical simulation in this thesis. Because stripping is conducted after 24h and the maximum stress will emerge 3 hours after stripping (the argument for this assumption will be given in Section 4.1), the increase of the hydration degree within these 3 hours is negligible.

[2] Standard cement chemistry abbreviations are used throughout this thesis: C=CaO, S=SiO_2, A=Al_2O_3, F=Fe_2O_3, $\bar{\mathrm{S}}$=SO_3, H=H_20.

pletion of the hydration process, $\overline{\mathrm{w/c}}$, can be determined as

$$\overline{\mathrm{w/c}} = \frac{5.3 \times 18}{228} = 0.418. \tag{11}$$

On the other hand, the chemical shrinkage associated with the stoichiometric relation given in Equation (8) is accessible from Equation (10) as $1 - 157.02/167.97 = 6.52\%$.

Table 1: Density ρ and molar mass $\mathcal{M}$ of different phases in cement paste (taken from [34])

		density ρ [kg/m^3]	molar mass $\mathcal{M}$ [kg/mol]
tricalcium silicate	C_3S	3150	0.228
water	H	998	0.018
calcium hydroxide	CH	2240	0.074
calcium silicate hydrate (saturated)	$C_{3.4}S_2H_8$	1990	0.454

Together with the density of the aggregate phase (taken as $\rho_{agg} = 2650$ kg/m^3 for quartz aggregate) and the mass fraction of cement in the concrete mix design m_{cem} [kg cement/(m^3 concrete)], the stoichiometric model gives access to the volume fractions in the material system. Figure 2 illustrates the volume fractions of three concrete mix designs with different w/c ratios and m_{cem}, all yielding a paste volume fraction of 30%. As presented in [35], the porosity of concrete as a function of ξ is determined by the volume fraction of water, air, and C-S-H gel porosity, with $n(\xi) = \mathrm{f}_{air}(\xi) + \mathrm{f}_{water}(\xi) + 0.373\ \mathrm{f}_{LDC-S-H}(\xi) + 0.237\ \mathrm{f}_{HDC-S-H}(\xi)$ (see Figure 3), and with the gel porosity for LD C-S-H and HD C-S-H, given as 0.373 and 0.237, respectively [35][3]. The multiscale homogenization scheme described in detail in [36] and summarized in Table 2 is employed for determination of effective poroelastic properties of early-age concrete (see Figure 4). The intrinsic elastic material parameters used in the analysis are summarized in Table 3. Whereas the Mori-Tanaka homogenization scheme [37][4] was employed in [36], in this thesis the so-called differential scheme (see

[3]According to [35], the water contained in the gel porosity of C-S-H cannot be considered as structural water. Hence, it has to be considered in the assessment of cement-based materials in the frame of a poromechanics formulation.

[4]The Mori-Tanaka homogenization scheme may be employed for matrix/inclusion-type morphologies with moderate values for the inclusion volume fraction of $<\sim 0.2$.

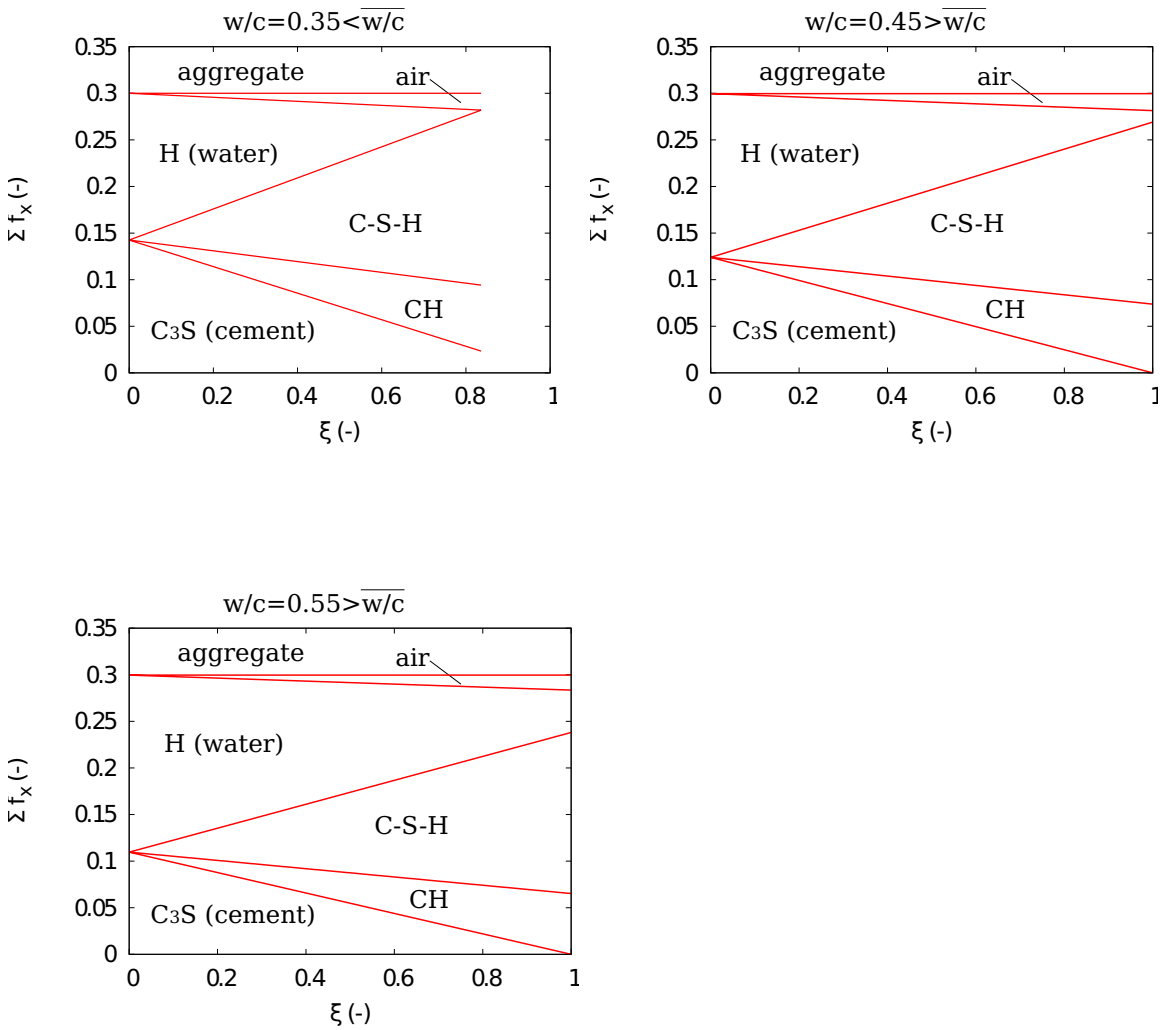

Figure 2: Volume fractions f_x of different phases in a cement-based material system with (a) w/c = 0.35 and m_{cem} = 448.99 kg cement/(m^3 concrete), (b) w/c = 0.45 and m_{cem} = 390.44 kg cement/(m^3 concrete), (c) w/c = 0.55 and m_{cem} = 345.40 kg cement/(m^3 concrete)

[38, 39]; for the extension toward multiple inclusion phases, see [40])[5] is employed for homogenization of representative volume elements, characterized by a matrix/inclusion-type morphology. As compared to the Mori-Tanaka scheme, the differential scheme does not have limitations as regards limited volume fractions of the inclusion phase [40].

Table 2: Multiscale homogenization scheme for determination of poroelastic properties of early-age concrete (RVE ... representative volume element; at homogenization step 0, the volume fraction of LD C-S-H and HD C-S-H was set equal to 0.7 and 0.3 [35], respectively)

homogenization step	composite/RVE denomination	matrix phase	inclusion phase(s)
0	C-S-H	low-density C-S-H (LD C-S-H)	high-density C-S-H (HD C-S-H)
1	porous C-S-H	C-S-H	water H, air
2	cement paste	porous C-S-H	portlandite CH, cement (C_3S)
3	concrete	cement paste	aggregate

Table 3: Intrinsic elastic parameters are taken from [44], accounting for drained conditions (the stiffness values for water and air, the bulk modulus k and the shear modulus μ were set equal to zero)

constituent	Young's modulus [GPa]	Poisson's ratio [–]
C_3S	135	0.3
LD C-S-H	21.7	0.24
HD C-S-H	29.4	0.24
CH	38	0.305
aggregate (quartz)	50	0.3

For determination of Biot's coefficient b^{hom} as a function of ξ, used later on in the constitutive relation of the multifield framework, the mode of upscaling detailed in [35], with

$$\mathrm{b}^{hom} = \sum_r \mathrm{f}_r b_r \langle A \rangle_r \tag{12}$$

[5]The model configuration for the self-consistent scheme [41, 42] is characterized by considering the different material phases as inclusions surrounded by the homogenized medium. The differential scheme represents an incremental formulation of the self-consistent scheme: consideration of a homogeneous medium embedding an inclusion phase with infinitesimal increase of the volume fraction of the latter. After each incremental increase, the effective material behavior, i.e., the behavior of the embedding material phase, is updated using the result of the micromechanical homogenization scheme for dilute defect distributions [43].

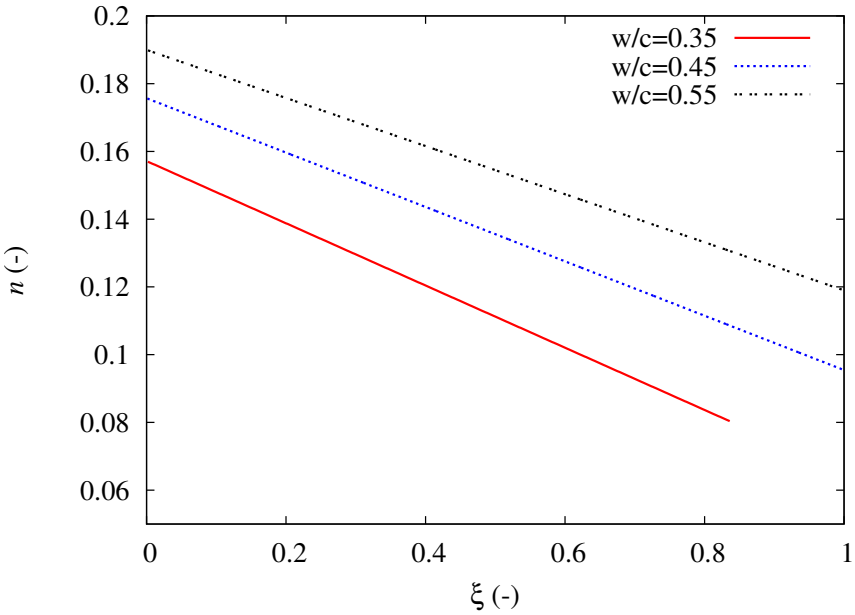

Figure 3: Evolution of the porosity obtained from the multiscale model

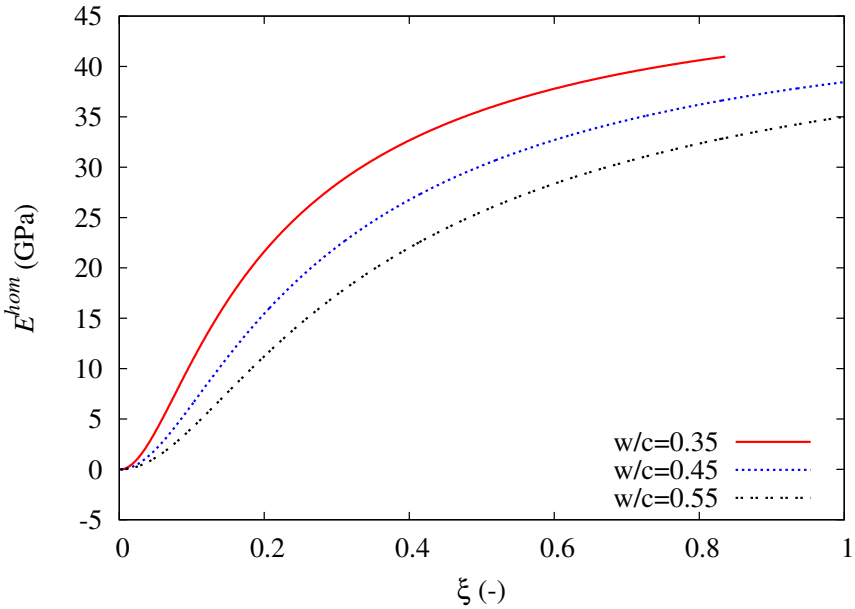

Figure 4: Evolution of the homogenized Young's modulus obtained from the multiscale model

for the isotropic case, is employed. Hereby, $\langle A \rangle_r$ is the volumetric part of the so-called strain localization tensor (in this thesis, in the scope of the differential scheme) of material phase "r". The gel porosity in LD C-S-H and HD C-S-H was taken into account by setting b as 0.71 and 0.61 [35], respectively, for these two material phases in the homogenization scheme. In Figure 5, the result from multiscale homogenization is compared to the classical micro-to-macro relation of poroelasticty (two material phases, solid matrix "s" and porous space), given as:

$$\mathrm{b}^{hom} = 1 - \frac{K^{hom}}{K^s}. \tag{13}$$

where the homogenized bulk modulus, K^{hom}, was determined by means of the multiscale upscaling scheme described above. In Equation (13), K^s is determined by employing the self-consistent scheme for (the theoretical) composite material containing the solid material phases: LD C-S-H and HD C-S-H gel porosity, C_3S, CH, and aggregate. Hereby, the gel porosity for LD C-S-H and HD C-S-H amounts to 0.373 and 0.237 [35], respectively. Hence, the volume fraction of the solid phase in LD C-S-H and HD C-S-H is given as $1 - 0.373 = 0.627$ and $1 - 0.237 = 0.763$, respectively. The intrinsic elastic properties of the solid phase in LD C-S-H and HD C-S-H were set equal to $E = 47.75$ GPa and $\nu = 0.25$ [35].

In this thesis, the heat capacity of concrete is acquired by an empirical law of mixtures, giving the heat capacity of the solid part of concrete c_p^s as a function of ξ from relations reported in [45]:

$$\begin{cases} c_p^{freshpaste} = 0.75 + 3.43 \frac{\mathrm{w/c}}{\mathrm{w/c}+1.0} \\ c_p^{paste} = c_p^{freshpaste} \left(1.0 - A_p \left[1.0 - \exp\left(-B_p\, \xi\right)\right]\right) \\ c_p^s = c_p^{paste}\ M_\mathrm{f}^{paste} + c_p^{agg}\ M_\mathrm{f}^{agg} \end{cases}, \tag{14}$$

where $c_p^{freshpaste}$ is the heat capacity of fresh paste, c_p^{paste} is the heat capacity of the paste in the course of hydration, c_p^{agg} is the heat capacity of the aggregate, M_f^{paste} and M_f^{agg} are the mass fractions of the cement paste and the aggregate, A_p and B_p are parameters provided by experiments, given as $A_p = 0.26$ and $B_p = 2.9$, as suggested in [45]. Figure 7 shows the evolution of the heat capacity in the course of the hydration process. The decrease of the heat

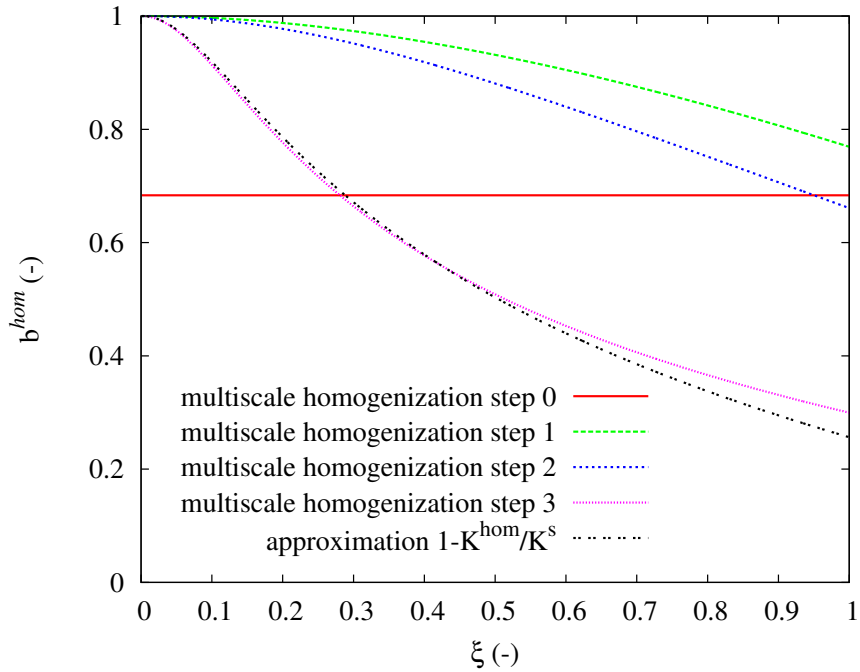

Figure 5: Evolution of the homogenized Biot's coefficient obtained from the multiscale homogenization scheme, compared to the approximation based on the bulk modulus of a "smeared" solid material matrix K^s for w/c = 0.45 (see Table 2, for detailed RVE at different multiscale homogenization steps)

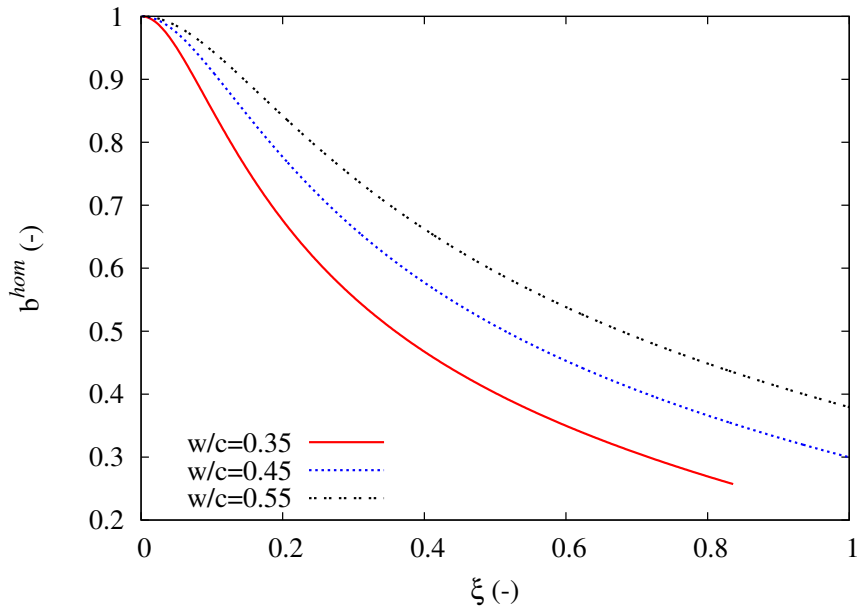

Figure 6: Evolution of homogenized Biot's coefficient obtained from the multiscale model

capacity with increasing hydration degree can be attributed to the decreasing mobility of water molecules [45].

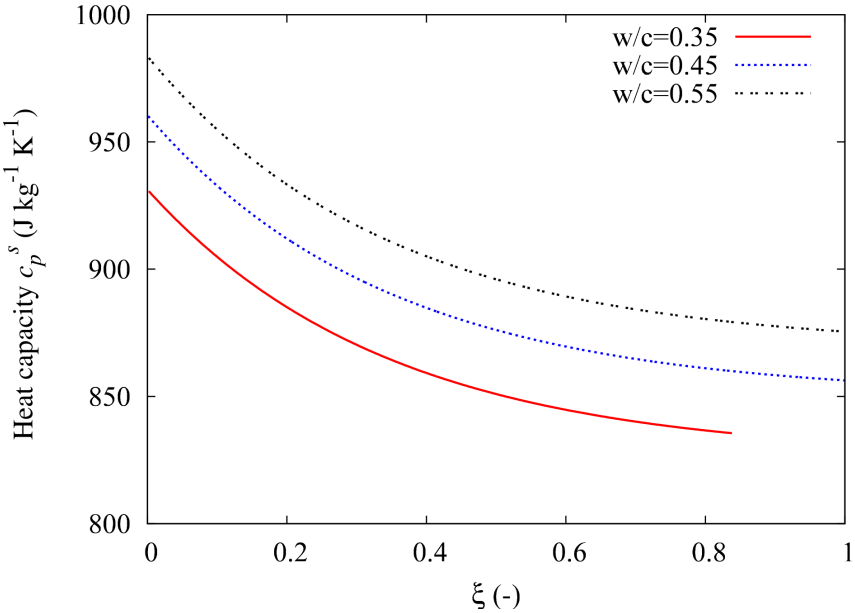

Figure 7: Evolution of heat capacity obtained from the law of mixtures [45] (heat capacity of quartz aggregate is taken as 700 J/(kg K))

The thermal conductivity of concrete is determined by the multiscale model presented in [46], employing a two-scale homogenization procedure (cement-paste/aggregate composite). According to [45], the thermal conductivity of the cement paste is almost independent of the hydration degree (about 1.0 J s^{-1} m^{-1} K^{-1}), giving the thermal conductivity of concrete exclusively as a function of the volume fractions (mix-design).

2.3.2 Simplified model for fire-loaded concrete

In case of temperature loading, the cement paste experiences dehydration which may be viewed as the inversion of hydration. Based on the description of the hydration process in early-age concrete, the macroscopic properties of concrete, such as strength and the elastic modulus, as well as the microscopic properties, such as Biot's coefficient, can be defined as functions of temperature. Whereas the former can also be determined by macroscopic experiments, a temperature-dependent function for the latter is difficult to obtain from experiments, which is necessary for connecting the liquid and the gas phase to the solid phase of porous media (see Subsection 2.4). The

relationship between the hydration degree and the temperature is given by [30]:

$$\begin{cases} \xi(T) = 1.0 & T \leq 105°\text{C}, \\ \xi(T) = \frac{1}{2}\left(1 - \sin\left[\frac{\pi}{2}\left(1 - 2\ e^{-0.004(T-105)}\right)\right]\right) & T > 105°\text{C}. \end{cases} \tag{15}$$

Based on Equation (15), the relationship between Biot's coefficient b^{hom}, the temperature T, and the hydration degree ξ is depicted in Figure 8.

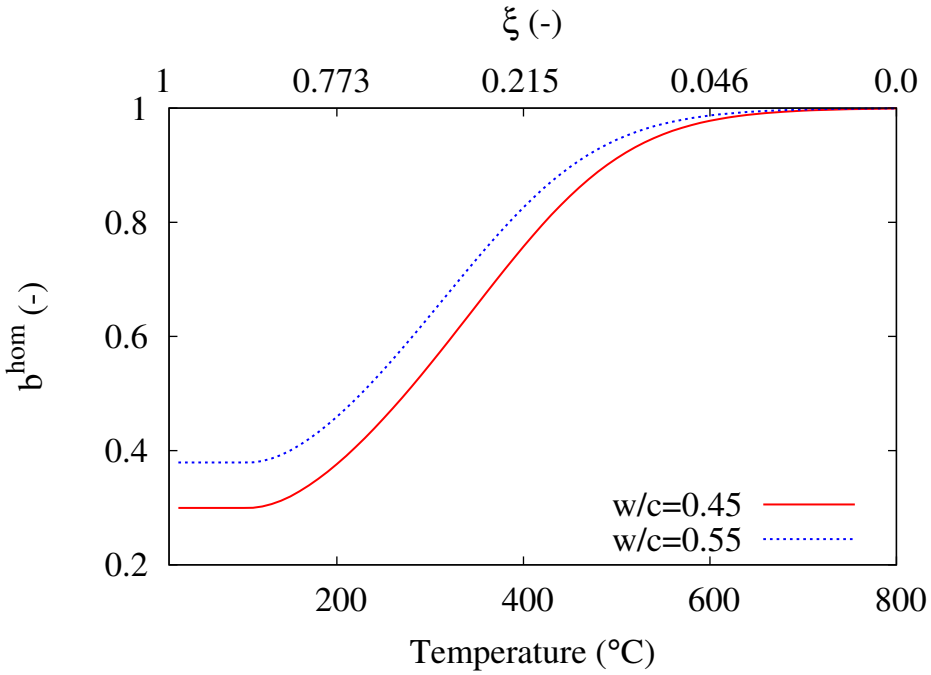

Figure 8: Relationship between Biot's coefficient, the temperature, and the hydration degree

2.4 Thermo-mechanical model

2.4.1 General effective stress formulation

Effective stress theory [8] can be adopted for connecting the thermo-hydro-chemical field (pore pressure) with the mechanical field (displacement). The general effective stress formulation, considering the temperature and the pore pressure is given by[6]

$$\begin{cases} \mathbf{E} = \mathbf{E}^e + \mathbf{E}^T, \\ \mathbf{\Sigma} = \mathbb{C} : \mathbf{E}^e - \mathbf{1}\ \mathrm{b}\left(p^g + \chi\ p^c\right), \end{cases} \tag{16}$$

[6]Plasticity is not considered in this formulation.

where the Bishop's coefficient χ represents the relation between the solid phase and the wetting phase (i.e., water). Specifically, χ is a function of the saturation degree S_w. This function can be obtained by means of upscaling [47] or from experimental results at room temperature [7, 9].

2.4.2 Effective stress formulation for early-age concrete

The differential form of the constitutive equation [33] is used to describe the stress state within early-age concrete, with $\mathbf{\Sigma}_{n+1} = \mathbf{\Sigma}_n + \Delta\mathbf{\Sigma}_{n+1}$[7]. Material parameters such as the elastic modulus and Biot's coefficient are considered as functions of the hydration degree ξ. Bishop's coefficient χ is considered to be equal to the saturation degree S_w. Hence, the effective stress formulation for early-age concrete is given as:

$$\begin{cases} \Delta\mathbf{\Sigma}_{n+1} + \mathbf{1}\ \mathrm{b}_{n+1}\ \Delta(\bar{p})_{n+1} = \Delta(\mathbb{C} : \mathbf{E})_{n+1} \\ \Delta\bar{p} = \Delta p^g - \Delta\left(S_w\ p^c\right) \\ \Delta(\mathbb{C} : \mathbf{E})_{n+1} = \mathbb{C}_{n+1} : \left(\Delta\mathbf{E}_{n+1} - \Delta\mathbf{E}^T_{n+1}\right) \end{cases}, \tag{17}$$

where $\mathbb{C} = \mathbb{C}^{hom}(\xi)$ and $\mathrm{b} = \mathrm{b}^{hom}(\xi)$.

2.4.3 Effective stress formulation for fire-loaded concrete

For concrete subjected to fire-loading, the load-induced thermal strain, $\mathbf{E}^{LITS}$, which represents the strain appearing in concrete when subjected to combined mechanical and thermal loading, is considered[8]. The deformation caused by the capillary pressure p^c, on the other hand, is ignored[9], giving the effective stress formulation for fire-loaded concrete as:

$$\begin{cases} \mathbf{E} = \mathbf{E}^e + \mathbf{E}^T + \mathbf{E}^{LITS}, \\ \mathbf{\Sigma} = \mathbb{C} : \mathbf{E}^e - \mathbf{1}\ \mathrm{b}^{hom} p^g, \end{cases} \tag{18}$$

where $\mathbb{C} = \mathbb{C}(T)$ and $\mathrm{b} = \mathrm{b}^{hom}(T)$.

Numerous experiments have shown that $\mathbf{E}^{LITS}$ depends on the level of loading, i.e., the stress $\mathbf{\Sigma}$. Based on the approach presented in [49], a relationship

[7] $(\cdot)_n$ represents the corresponding parameter at time instant t_n

[8] In this thesis, $\mathbf{E}^{LITS}$ may also be considered as a plastic strain in case of compressive loading.

[9] In fact, in [48] it was shown that drying shrinkage caused by loss of water of fire-loaded concrete has a relatively small influence on the deformation of concrete.

between $\mathbf{E}^{LITS}$ and $\mathbf{\Sigma}$ is given in [50, 51], which reads as:

$$\mathbf{E}^{LITS} = k^{LITS} \frac{\mathbf{\Sigma}}{f_c(T)} \frac{\mathrm{Tr}(\mathbf{E}^T)}{3}, \tag{19}$$

where k^{LITS} is the LITS parameter (in [49], k^{LITS} was suggested as 2.35 for uniaxial loading and as 1.7 for biaxial loading; in [51], it was found that $k^{LITS} = 0.4$ fits well with experimental results). A comparison between the model results (obtained with $k^{LITS} = 0.6$) and experimental results is shown in Figure 9 (see [50] for details).

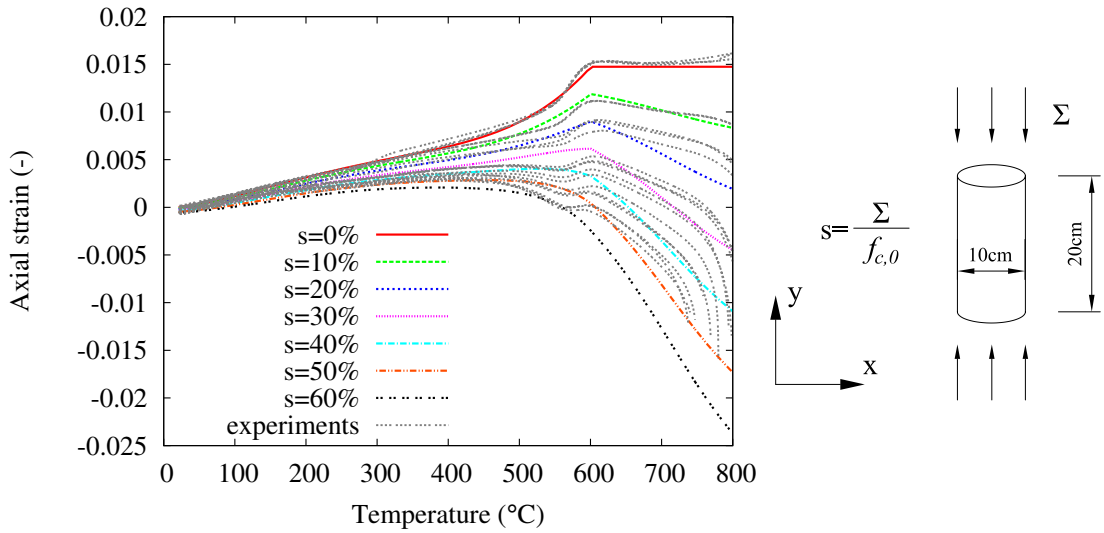

Figure 9: Comparison of model-based axial strain with experimental results [50] (s: level of loading, $f_{c,0}$: initial compressive strength)

2.5 Conclusions

In this section, a micromechanics-based coupled thermo-hydro-chemo-poro-mechanical multifield framework was presented. The framework was given in a form appropriate for early-age concrete and fire-loaded concrete. The main steps of the development of this framework are summarized in the following:

- Accounting for mass and energy conservation, the mathematical relations describing thermal, hydral, chemical processes and their interaction were presented.

- Considering the hydration process of concrete, a multiscale homogenization method for determination of the elastic modulus, porosity and Biot's coefficient was presented.
- By adopting the effective stress theory, the coupled thermo-hydro-chemo-poro processes are connected with the stress and deformation state. Hereby, the differential form of the effective stress formulation suitable for early-age concrete as well as load-induced thermal strains that are essential for fire-loaded concrete are taken into account.

3 Strong discontinuity approach for quasi-brittle materials

3.1 Background

Within the finite element method (FEM), models for simulating fracture of quasi-brittle materials like concrete exist for more than half a century [52, 53]. The traditional approaches include smeared-crack models and discrete-crack models. Within smeared-crack models, fracture is represented by reduction of the local stiffness and strength (at Gauss points). Discrete-crack models, on the other hand, employ interface elements (such as the element proposed in [54, 55]), allowing the cracks to propagate along the boundaries of the finite elements. Though both models have been validated and applied successfully to simulation of fracture of quasi-brittle materials [56, 57], both methods have severe restraints, such as locking and mesh-bias.

In recent years, numerical models with cracks embedded in finite elements were developed, considering either nodal enrichment such as XFEM (extended finite element method) [58] and PUFEM (partition-of-unity finite element method) [59] or elemental enrichment such as SDA (strong discontinuity embedded approach), with both approaches giving similar results. However, nodal enrichment requires more computing time [60, 61, 62].

Considering SDA, elements which locally capture discontinuities were first introduced in [63] and applied in [64, 65, 66, 67]. In [68], the notion of enhanced assumed strains (EAS) was introduced, linking SDA to classical models in plasticity and continuum damage mechanics [69, 70]. In [71], a finite width of the localization zone, h, was introduced, taking into account the experimentally-observed fracture process zone [72, 73, 74]. However, in the course of cracking of quasi-brittle materials, the fracture process zone ($h > 0$) transforms into a macrocrack ($h = 0$) [75], making the SDA a suitable approach to describe the fracture process.

Nevertheless, SDA suffers from stress-locking caused by improper propagation of the crack [76, 77]. To overcome this locking effect, different methods such as rotating cracks [78], multiple cracks [77, 79], delayed embedded crack models [80, 81], and crack-tracking strategies [82, 83] were proposed in the literature. For all of these the models, crack-tracking strategies have proved to

be reliable and robust. They permit prediction of further propagation of the crack, based on the history of mechanical states (stress, strain, displacement, energy), and provide continuous crack paths.

Moreover, most published applications of SDA models adopt simple finite elements, such as constant strain triangles (CST) [84, 85, 60] or bilinear quadrilateral elements [86]. However, higher-order elements are required in coupled displacement-permeation analysis, with quadratic interpolation functions for the displacements assuring a globally continuous distribution of the pressure field (see Figure 10). A reliable SDA framework which applies to higher-order elements (adopting quadratic interpolation functions) will enable future applications of SDA to fracture-permeation coupled analysis.

In this section, SDA is combined with an energy-based crack-tracking strategy [83, 87], using eight-node quadrilateral elements. The performance of the proposed method for the analysis of fracture processes is illustrated by means of numerical benchmarks such as the three-point bending test, the L-shaped panel test, and the pull-out test.

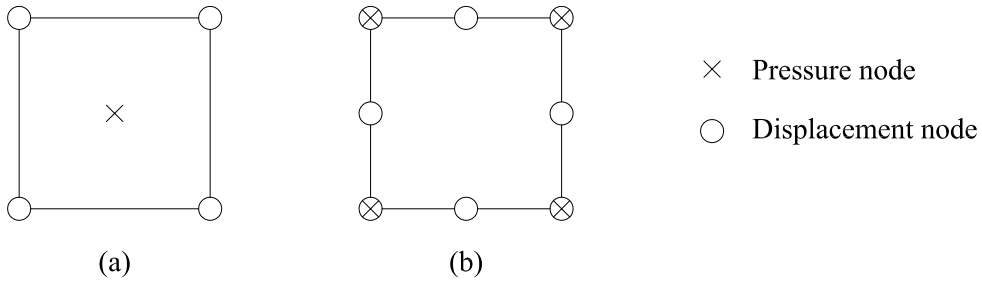

Figure 10: Elements used for displacement-permeation analysis: (a) linear interpolation functions for the displacements (discontinuous pressure field), (b) quadratic interpolation functions for the displacements (continuous pressure field)

3.2 Basics of SDA

3.2.1 Kinematics

The SDA adopted in this section was presented in [78] and applied later in [88, 89, 90]. Figure 11 shows the 2D domain Ω, containing a discontinuity $\mathbf{L}$, which divides the domain into Ω^+ and Ω^-. Parts of the subdomain Ω^+ and Ω^- are taken as the localization zone. They are referred to as Ω^+_φ and Ω^-_φ. The displacement field of Ω can be described as follows:

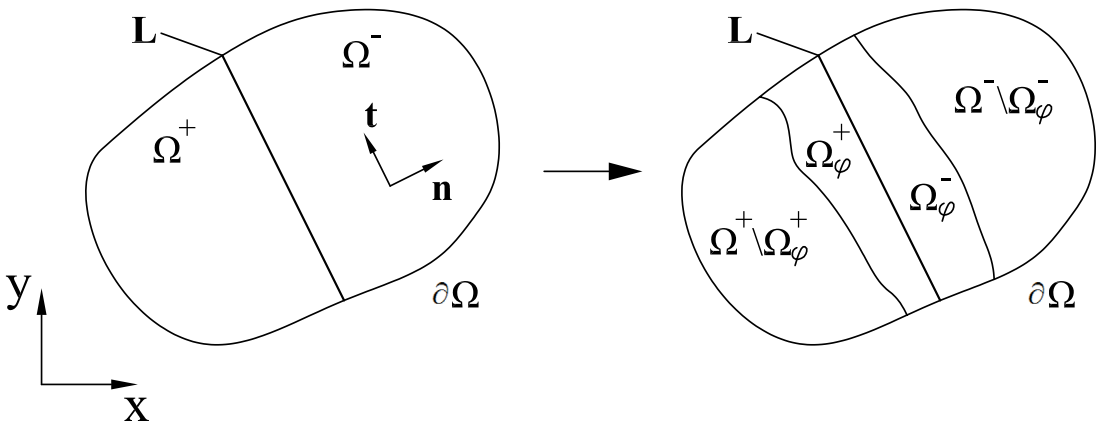

Figure 11: Domain Ω with a discontinuity $\mathbf{L}$

$$\mathbf{u}(\mathbf{x}) = \bar{\mathbf{u}}(\mathbf{x}) + [H_s(\mathbf{x}) - \varphi(\mathbf{x})][\![u]\!], \tag{20}$$

where $\bar{\mathbf{u}}(\mathbf{x})$ is the regular part of the displacement field, $H_s(\mathbf{x})$ is a Heaviside function, and $\varphi(\mathbf{x})$ is a smooth differentiable function ($\nabla\varphi$ exists), with

$$\varphi(\mathbf{x}) = \begin{cases} 0 & \forall x \in \Omega^- \setminus \Omega^-_\varphi, \\ 1 & \forall x \in \Omega^+ \setminus \Omega^+_\varphi, \\ \text{continuous function} & \forall x \in \Omega^-_\varphi \cup \Omega^+_\varphi. \end{cases} \tag{21}$$

Hence, the strain field within Ω is obtained as

$$\boldsymbol{\varepsilon}(\mathbf{x}) = \nabla^S \mathbf{u}(\mathbf{x}) = \underbrace{\nabla^S \bar{\mathbf{u}}(\mathbf{x}) - ([\![u]\!](\mathbf{x}) \otimes \nabla\varphi)^S}_{\bar{\boldsymbol{\varepsilon}}(\mathbf{x}), \forall x \in \Omega \setminus \mathbf{L}} + \underbrace{\delta_{\mathbf{L}}([\![u]\!](\mathbf{x}) \otimes \mathbf{n})^S}_{\boldsymbol{\varepsilon}_\delta(\mathbf{x}), \forall x \in \mathbf{L}}, \tag{22}$$

where $(\cdot)^S$ denotes the symmetric part of the tensor, $\delta_{\mathbf{L}}$ denotes the Dirac-delta distribution, and $\nabla[\![u]\!](\mathbf{x})$ is assumed to be zero [78]. Further, the regular part $\bar{\boldsymbol{\varepsilon}}(\mathbf{x})$ can be decomposed into compatible strains and enhanced strains [68], giving

$$\bar{\boldsymbol{\varepsilon}}(\mathbf{x}) = \underbrace{\nabla^S \bar{\mathbf{u}}(\mathbf{x})}_{\text{compatible strains}} - \underbrace{([\![u]\!](\mathbf{x}) \otimes \nabla\varphi)^S}_{\text{enhanced strains}}, \tag{23}$$

In case the crack direction is known, the normal unit vector $\mathbf{n}$ and the parallel unit vector $\mathbf{t}$ of the failure surface, with $\mathbf{n} \cdot \mathbf{t} = 0$, are known. Ac-

cordingly, the displacement jump at the crack, $[\![u]\!](\mathbf{x})$, can be expressed as $[\![u]\!] = \zeta_n(\mathbf{x})\mathbf{n} + \zeta_t(\mathbf{x})\mathbf{t}$, with $\zeta_n(\mathbf{x})$ and $\zeta_t(\mathbf{x})$ as the amplitudes of the jump along $\mathbf{n}$ and $\mathbf{t}$, respectively. Thus, Equation (23) can be rewritten as

$$\bar{\boldsymbol{\varepsilon}}(\mathbf{x}) = \underbrace{\nabla^S \bar{\mathbf{u}}(\mathbf{x})}_{\boldsymbol{\varepsilon}^t} - \underbrace{\left[(\mathbf{n} \otimes \nabla\varphi)^S \zeta_n(\mathbf{x}) + (\mathbf{t} \otimes \nabla\varphi)^S \zeta_t(\mathbf{x})\right]}_{\boldsymbol{\varepsilon}^p}, \tag{24}$$

where $\boldsymbol{\varepsilon}^t$ is the strain tensor and $\boldsymbol{\varepsilon}^p$ is the part of $\boldsymbol{\varepsilon}^t$ associated with plastic strains. In case the crack direction is fixed, $\dot{\mathbf{n}} = \mathbf{0}$ and $\dot{\mathbf{t}} = \mathbf{0}$. Thus, the strain rate $\dot{\bar{\boldsymbol{\varepsilon}}}(\mathbf{x})$ is determined only by $\dot{\boldsymbol{\varepsilon}}^t$, $\dot{\zeta}_n$, and $\dot{\zeta}_t$.

3.2.2 Finite-element implementation

Considering a uniform displacement jump within the finite element "e", $[\![u]\!](\mathbf{x})$ becomes $[\![u]\!]^{(e)}$, giving the strain field $\bar{\boldsymbol{\varepsilon}}^{(e)}(\mathbf{x})$ as follows:

$$\bar{\boldsymbol{\varepsilon}}^{(e)}(\mathbf{x}) \approx \sum_{i=1}^{n_e} \left(\nabla N_i^{(e)} \otimes \mathbf{u}_i\right)^S - \left[(\mathbf{n} \otimes \nabla\varphi^{(e)})^S \zeta_n^{(e)} + (\mathbf{t} \otimes \nabla\varphi^{(e)})^S \zeta_t^{(e)}\right], \tag{25}$$

where n_e is the number of nodes of element "e", $\mathbf{u}_i$ is the displacement vector of node "i". $\varphi^{(e)}$ and $\nabla\varphi^{(e)}$ are obtained as [78]

$$\varphi^{(e)} = \sum_{i=1}^{n_e+} N_i, \tag{26}$$

$$\nabla\varphi^{(e)} = \frac{1}{V} \int_\Omega \nabla\varphi(\mathbf{x}) d\Omega, \tag{27}$$

with n_e+ representing the number of nodes in Ω_φ^+ [91].

3.2.3 Constitutive relation

According to [87, 92], a mixed-mode traction-separation is considered in this section, with an equivalent amplitude of the displacement jump (or crack opening) ζ_{eq} defined as

$$\zeta_{eq} = \sqrt{\zeta_n^2 + \beta^2 \zeta_t^2}, \tag{28}$$

where β governs the contribution of Mode I and Mode II crack opening, respectively, to ζ_{eq}. For $\beta = 1$, ζ_{eq} is equal to the face-to-face distance of the crack, see Figure 12. According to [93, 94], $\beta = 1$ is well-suited for concrete

and will therefore be considered in this thesis.

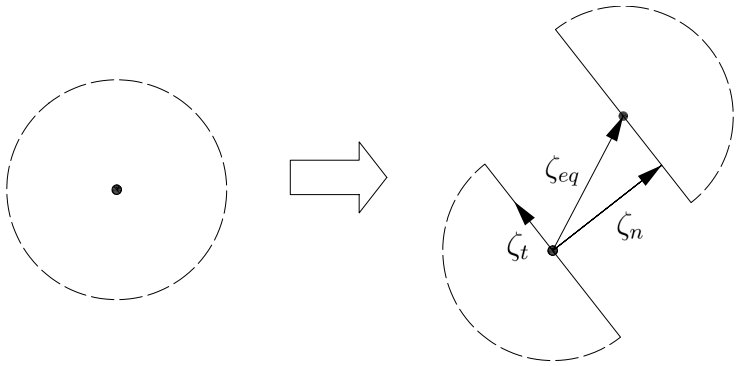

Figure 12: Geometric representation of ζ_n, ζ_t, and ζ_{eq} for $\beta = 1$

The traction components T_n (along $\mathbf{n}$) and T_t (along $\mathbf{t}$) are determined by [87]

$$\begin{aligned} &T_n = \frac{T_{eq}}{\zeta_{eq}}\zeta_n,\ T_t = \beta^2\frac{T_{eq}}{\zeta_{eq}}\zeta_t, \\ &\text{with } T_{eq} = f_t \exp\left(-\frac{f_t}{G_f}\zeta_{eq}\right), \end{aligned} \tag{29}$$

where f_t is the uniaxial tensile strength and G_f is the fracture energy.

For initiation of damage, the Rankine criterion is used, reading $\phi_{RK}(\boldsymbol{\sigma}) = (\mathbf{n} \otimes \mathbf{n}) : \boldsymbol{\sigma} - f_t = 0$. After initiation, the yield functions for mixed-mode failure, given as

$$\begin{aligned} \phi_n(\boldsymbol{\sigma}, \zeta_n) &= (\mathbf{n} \otimes \mathbf{n}) : \boldsymbol{\sigma} - T_n(\zeta_n, \zeta_t) = 0, \\ \phi_t(\boldsymbol{\sigma}, \zeta_t) &= (\mathbf{t} \otimes \mathbf{n}) : \boldsymbol{\sigma} - T_t(\zeta_n, \zeta_t) = 0, \end{aligned} \tag{30}$$

are used for determination of the crack opening (ζ_n, ζ_t).

For iteration step i, the known state variables at a specific Gauss point are $(\boldsymbol{\varepsilon}_i^t, \boldsymbol{\varepsilon}_{i-1}^t, \zeta_{n,i-1}, \zeta_{t,i-1})$, while the unknown state variables are $(\zeta_{n,i}, \zeta_{t,i})$, with $\zeta_{n,i} = \zeta_{n,i-1} + \Delta\zeta_{n,i}$ and $\zeta_{t,i} = \zeta_{t,i-1} + \Delta\zeta_{t,i}$. In the general return-mapping algorithm [95], the trail stress $\boldsymbol{\sigma}^{tr}$ is introduced as

$$\boldsymbol{\sigma}^{tr} = \mathbb{C} : \left[\boldsymbol{\varepsilon}_i^t - (\mathbf{n} \otimes \nabla\varphi^{(e)})^S \zeta_{n,i-1} - (\mathbf{t} \otimes \nabla\varphi^{(e)})^S \zeta_{t,i-1}\right], \tag{31}$$

where $\mathbb{C}$ is the elastic stiffness tensor. Based on the trial state, the unknown state variables $\Delta\zeta_{n,i}$ and $\Delta\zeta_{t,i}$ are determined from the yield function, read-

ing[10]

$$\begin{cases} (\mathbf{n}\otimes\mathbf{n}) : \boldsymbol{\sigma}^{tr} - g_{11}\Delta\zeta_{n,i} - g_{12}\Delta\zeta_{t,i} - T_n = 0 \\ (\mathbf{t}\otimes\mathbf{n}) : \boldsymbol{\sigma}^{tr} - g_{21}\Delta\zeta_{n,i} - g_{22}\Delta\zeta_{t,i} - T_t = 0 \end{cases}, \tag{32}$$

with

$$\begin{array}{ll} g_{11} = (\mathbf{n}\otimes\mathbf{n}) : \mathbb{C} : (\mathbf{n}\otimes\nabla\varphi^{(e)})^S & g_{12} = (\mathbf{n}\otimes\mathbf{n}) : \mathbb{C} : (\mathbf{t}\otimes\nabla\varphi^{(e)})^S \\ g_{21} = (\mathbf{t}\otimes\mathbf{n}) : \mathbb{C} : (\mathbf{n}\otimes\nabla\varphi^{(e)})^S & g_{22} = (\mathbf{t}\otimes\mathbf{n}) : \mathbb{C} : (\mathbf{t}\otimes\nabla\varphi^{(e)})^S \end{array}. \tag{33}$$

For each iteration step, the relation between the differentials of the tractions, dT_n and dT_t, and the crack-opening parameters, $d\zeta_n$ and $d\zeta_t$, is given as [87]

$$\begin{bmatrix} dT_n \\ dT_t \end{bmatrix} = \mathbf{D} \begin{bmatrix} d\zeta_n \\ d\zeta_t \end{bmatrix}, \tag{34}$$

with

$$\begin{cases} \mathbf{D} = -\frac{\beta^2 f_t T_{eq}}{\zeta_{eq}^2} \begin{bmatrix} \frac{\zeta_n^2}{\beta^2 G_f} - \frac{\zeta_t^2}{f_t\zeta_{eq}} & \zeta_n\zeta_t\frac{G_f+f_t\zeta_{eq}}{G_f f_t\zeta_{eq}} \\ \zeta_n\zeta_t\frac{G_f+f_t\zeta_{eq}}{G_f f_t\zeta_{eq}} & \frac{\beta^2\zeta_t^2}{G_f} - \frac{\zeta_n^2}{f_t\zeta_{eq}} \end{bmatrix} \text{ for loading} \\ \\ \mathbf{D} = T_{eq}\begin{bmatrix} 1 & 0 \\ 0 & \beta^2 \end{bmatrix} \text{ for elastic unloading,} \end{cases} \tag{35}$$

leading to the elastoplastic tangent moduli $\mathbb{C}^{ep}$ as

$$\mathbb{C}^{ep} = \frac{d\boldsymbol{\sigma}}{d\boldsymbol{\varepsilon}} = \mathbb{C} - \mathbb{C} : \begin{bmatrix} \mathbf{n}\otimes\mathbf{n} & \mathbf{t}\otimes\mathbf{n} \end{bmatrix} : (\mathbf{G}-\mathbf{D})^{-1} : \begin{bmatrix} \mathbf{n}\otimes\mathbf{n} \\ \mathbf{t}\otimes\mathbf{n} \end{bmatrix} : \mathbb{C}, \tag{36}$$

with

$$\mathbf{G} = \begin{bmatrix} g_{11} & g_{12} \\ g_{21} & g_{22} \end{bmatrix}.$$

As mentioned in [78, 89], condensation of the displacement jump at the material level without a standard static condensation technique allows the use of classical procedures for solving elastoplastic continuum models.

The condition number $\kappa(\mathbf{G})$ of the matrix $\mathbf{G}$ is employed to assess the numerical stability of Equation (32) and, thus, of the SDA model, with high values of $\kappa(\mathbf{G})$ indicating poor numerical stability. According to Equation (33),

[10] For loading, when the condition $(\mathbf{n}\otimes\mathbf{n}) : \boldsymbol{\sigma}^{tr} - T_n > 0$ is fulfilled, Equation (32) is solved by the Newton-Raphson method.

$\kappa(\mathbf{G})$ is a function of Poisson's ratio ν and of the angle between $\mathbf{n}$ and $\nabla\varphi^{(e)}$, denoted as θ. Figure 13 shows the condition number $\kappa(\mathbf{G})$ as a function of θ, indicating that the numerical stability of the SDA model decreases with increasing θ, which has also been reported in [96].

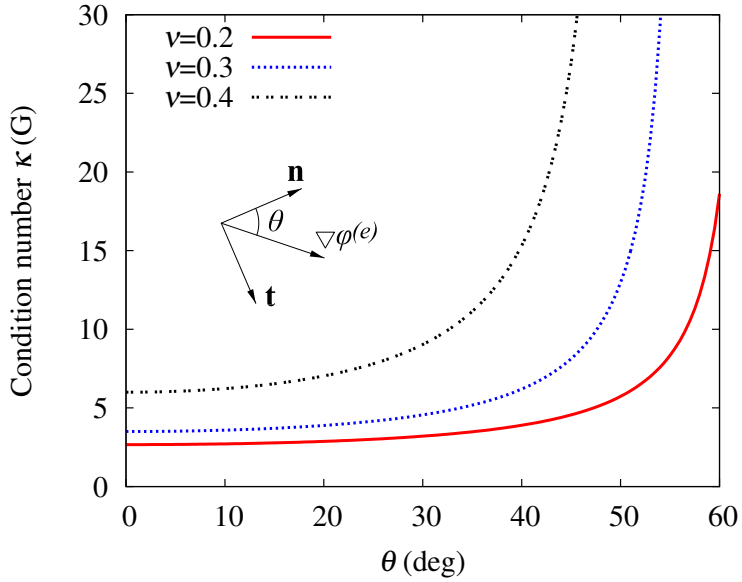

Figure 13: Condition number $\kappa(\mathbf{G})$, with $\kappa(\mathbf{G}) = \|\mathbf{G}^{-1}\|_2 \cdot \|\mathbf{G}\|_2$, as a function of ν and θ

3.2.4 Application of reduced integration for eight-node quadrilateral element

As outlined in [78, 97], in case of higher-order elements, the crack opening has different values at difference Gauss points, with some Gauss points remaining in the elastic state in the course of cracking. This causes stress locking, which cannot be eliminated by tracking strategies, as it occurs at the element level. As a remedy, reduced integration using one Gauss point at the element center will be adopted.

The effect of the underlying integration technique is illustrated by means of two examples, characterized by two different load cases, see Figure 14. For both of them, the crack direction is assumed to be parallel to the y axis. The respective force-displacement curves are shown in Figure 15.

For CASE 1, all Gauss points experience the same stress/strain states, resulting in a crack direction parallel to the y axis. Therefore, full and reduced integration give the same results[11].

[11] Although full integration for CASE 1 gives the same result as reduced integration, the numerical stability

For CASE 2, the stress/strain states vary within the element, leading to different crack directions at different Gauss points for the case of full integration. Assuming one global crack direction for a single element, full integration results in stress locking at the element level.

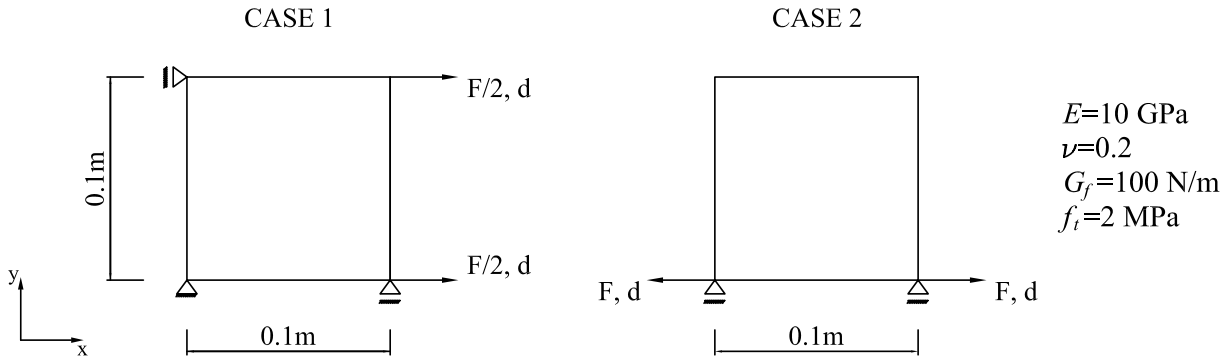

Figure 14: Single-element example: geometrical dimensions, loading conditions, and material properties

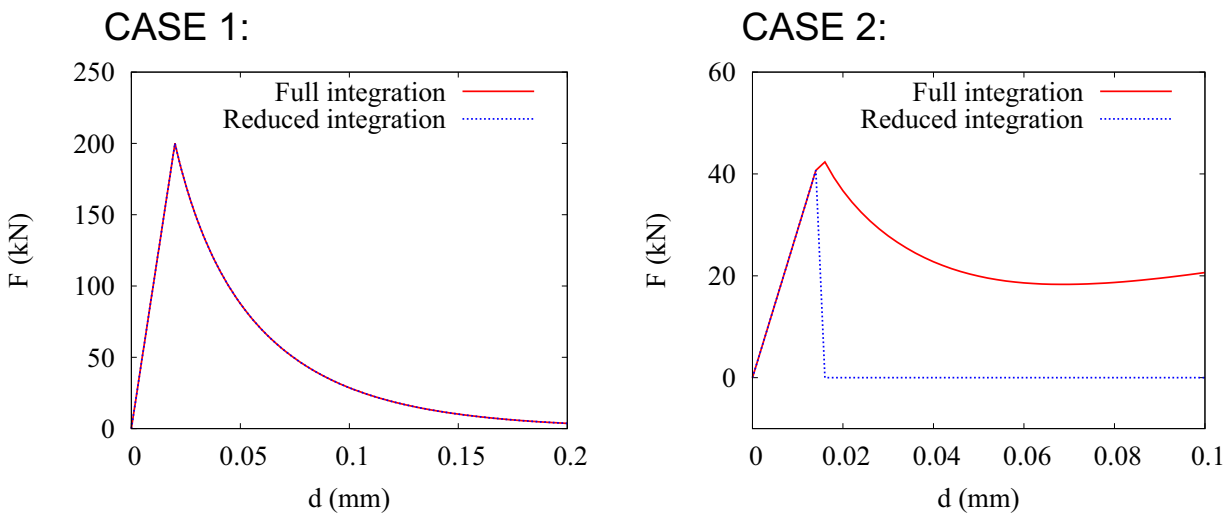

Figure 15: Single-element example: force-displacement curves illustrating the effect of full and reduced integration

of full integration is poorer, since different Gauss points may be loaded differently, which is caused by numerical errors in the course of the iteration process.

3.3 Energy-based crack-tracking strategy for SDA

3.3.1 Introduction of crack-tracking methods

Crack-tracking strategies are used (i) to specify the propagation of the crack and (ii) to smooth the crack path (see Table 4). Comparison of numerical results from different crack-tracking strategies reported in the literature can be found in [83, 98, 99, 100].

While XFEM is able to locate the exact position of crack tips, in case of SDA, cracks propagate from one boundary of an element to another boundary of the element, see Figure 16. Hence, the exact position of the crack tip is

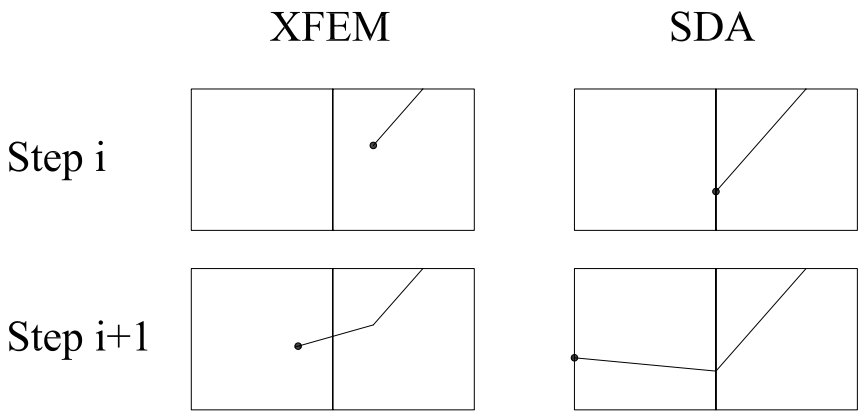

Figure 16: Propagation of crack in XFEM and in SDA

not accessible for SDA, resulting in inexact stress states around the crack tip. Accordingly, the level-set method and the maximum energy release method, which are commonly used in XFEM and highly rely on the stress/strain states around the crack tip, cannot be applied in SDA without considerable modifications.

The local tracking strategy is one of the most widely used tracking strategies. Applying this strategy, stress locking may be encountered. However, this drawback may be overcome by some simple modifications [85]. In any case, a zigzag crack path is almost inevitable.

The global tracking strategy is very powerful. For some examples, this strategy may even give a smooth crack path in the beginning of loading, as observed for the mixed-mode fracture test [83] and the four-point bending test, considering a double-notched beam [101]. However, in some cases, such as the L-shaped panel, the underlying isotherm for predicting the crack path

is varying significantly till the end of loading [83, 100], resulting in a zigzag crack path. The weakness of the global tracking strategy was also discussed in [89].

The partial domain tracking strategy is a modified version of the global tracking strategy, which combines the advantages of the local and the global tracking strategy [89]. However, presently this strategy is only suitable for constant-strain-triangle elements (CST elements)[12].

In summary, most existing crack-tracking strategies used in XFEM and SDA are not suitable for the SDA adopted in this section. Hence, a modified energy-based crack-tracking strategy is adopted, considering the energy of the entire system, which does not require precise information about the stress/strain state around the crack tip.

Table 4: Crack-tracking strategies

	Criterion	Smoothing	Suitable for	Reference
(a)	MPS	Maximum curvature of crack	SDA	[85]
(b)	MPS	Isotherm	SDA & XFEM	[82, 83]
(c)	NMPS	Isotherm	SDA	[88]
(d)	MCS	Level set	XFEM	[102]
(e)	MER	—	XFEM	[99]
(f)	MPE	—	XFEM	[87]

(a): Local tracking
(b): Global tracking
(c): Partial domain crack-tracking
(d): Level-set method
(e): Maximum energy release rate (J-integrals)
(f): Energy-based crack-tracking

MPS: Maximum principal stress/strain
NMPS: Maximum principal nonlocal strain
MCS: Maximum circumferential stress
MER: Maximum energy release rate
MPE: Minimization of total potential energy

[12]The partial domain and the global tracking strategy introduce an unknown on the nodes which is solved in every loading step, with the contour lines of the unknown representing the cracking path. Whereas, [89] only presented corresponding formulas for solving the unknown in CST element

3.3.2 Theory of the energy-based crack-tracking strategy

Early applications of the energy-based crack propagation in finite-element analysis can be found in [103]. Though based on linear-elastic fracture mechanics, unlike the maximum circumferential stress criterion or the maximum energy release rate criterion, the energy-based criterion is capable to predict the direction of crack propagation also for cohesive cracks [87, 99].

Considering a deformed body Ω with the body force $\mathbf{b}$, the surface force $\mathbf{t}$, and a crack with the cohesive force $\mathbf{w}$ at its surface (see Figure 17), the mechanical energy Ψ of the body consists of the elastic strain energy U, and the dissipated energy E, minus the work W done by the applied forces, which is a function of the crack-propagation angle θ and the crack-propagation length l, i.e. $\Psi = \Psi(\theta, l)$. Based on linear-elastic fracture mechanics, θ and l are determined by minimizing Ψ. As in the SDA, the crack propagates from one boundary of an element to another one; Ψ is only a function of θ, i.e. $\Psi = \Psi(\theta)$. Ψ follows from:

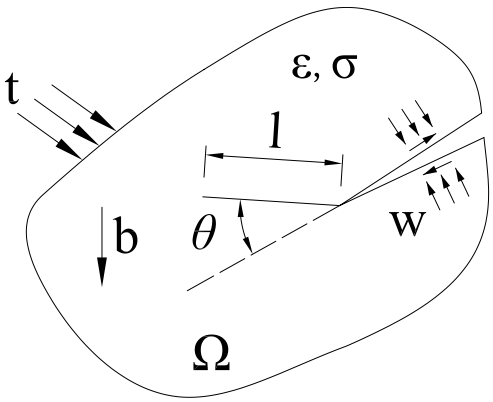

Figure 17: Deformed body with crack

$$
\begin{aligned}
&\Psi = U + E - W, \\
&\text{where} \\
&U = \int_\Omega \left(\int_0^{\boldsymbol{\varepsilon}} \boldsymbol{\sigma}(\boldsymbol{\varepsilon}) : d\boldsymbol{\varepsilon} \right) d\Omega, \\
&E = \int_A \left(\int_0^{\zeta_n} T_n \cdot d\zeta_n + \int_0^{\zeta_t} T_t \cdot d\zeta_t \right) dA, \\
&W = \int_\Omega \left(\int_0^{\mathbf{u}} \mathbf{b}\ d\mathbf{u} \right) d\Omega + \int_{\partial\Omega} \left(\int_0^{\mathbf{u_t}} \mathbf{t}\ d\mathbf{u_t} \right) d\partial\Omega.
\end{aligned}
\tag{37}
$$

where $\mathbf{u}$ is the displacement of a point of the body, $\mathbf{u_t}$ is the displacement of

a point of the surface of the body loaded by $\mathbf{t}$, and A is the surface of the crack.

With a predefined scanning angle γ and an interval angle $\Delta\gamma$ (in [99], $\gamma = 60°$ and $\Delta\gamma = 4°$ were used), the energy Ψ is calculated for different directions of crack propagation. The obtained discrete values of Ψ are fitted[13], giving access to the function $\Psi = \Psi(\theta)$. Then, the value of θ, which defines the angle for further propagation of the crack, is obtained by means of minimization of $\Psi(\theta)$, i.e. with $\partial\Psi/\partial\theta = 0$ and $\partial^2\Psi/\partial\theta^2 > 0$.

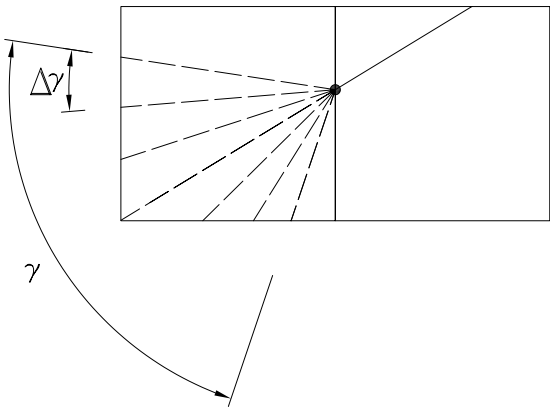

Figure 18: Application of energy-based crack-tracking in SDA

Nevertheless, because of $\Psi = \Psi(\theta) = \Psi(\boldsymbol{\varepsilon}^p)$, with $\boldsymbol{\varepsilon}^p = \boldsymbol{\varepsilon}^p\left[\nabla\varphi(\theta), \theta\right]$, and because the function $\nabla\varphi(\theta)$ is not continuous in SDA, scanning for the minimum value of Ψ within a prescribed angle γ is rather questionable. Figure 19 illustrates this remark, using a triangular constant strain element with a rotating crack. From Case A to Case B, the angle of the crack differs significantly, whereas the vector $\nabla\varphi$ remains the same. On the other hand, from Case B to Case C, with only a slight variation of the crack angle, $\nabla\varphi$ changes significantly as the nodal value of φ has changed.

3.3.3 Modified SDA model

The discontinuity of the total energy Ψ is caused by the sudden change of the nodal value of φ as the crack passes a node (see Figure 19), which may be obviously avoided if the vector $\nabla\varphi$ remains parallel to $\mathbf{n}$[14]. Accordingly,

[13] In [99], fitting with moving least squares was suggested. In [87], it was shown that a polynomial function with order 2-4 gives sufficiently accurate results.

[14] When $\nabla\varphi$ remains parallel to $\mathbf{n}$, the SDA model shows best numerical stability (see Figure 13), which is another accompanying advantage of the modified SDA model.

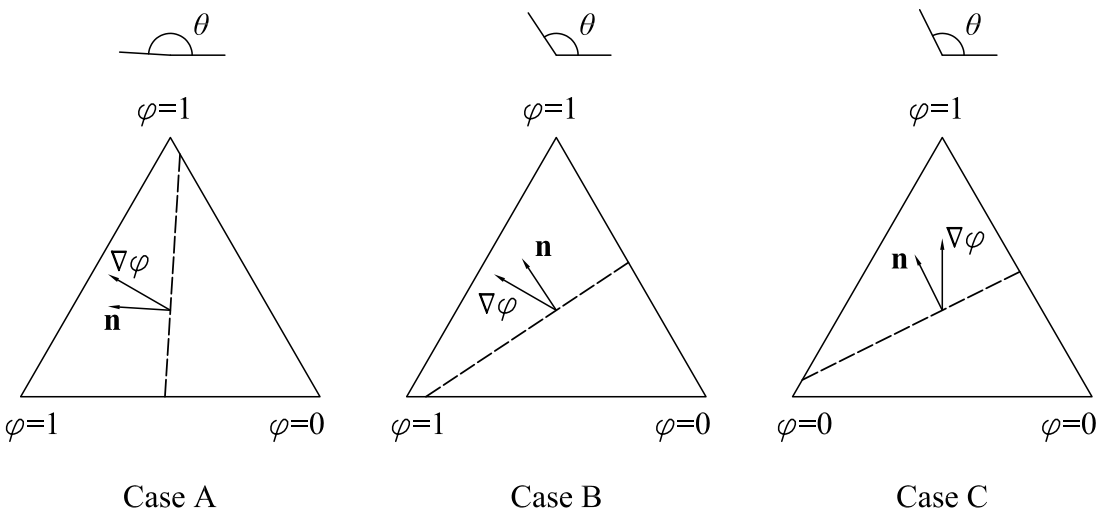

Figure 19: Illustration of noncontinuous function of $\nabla\varphi(\theta)$ for a rotating crack

Equation (27), originally used for determination of $\nabla\varphi$, is replaced by

$$\nabla\varphi = s\ \mathbf{n}, \tag{38}$$

where $s = A/V$ is a scaler quantity; A is the area of the crack and V is the volume of the finite element experiencing cracking. Hereby, the crack area A is obtained from a crack passing through the center Gauss point, accounting for the reduced integration scheme for determination of ζ_n and ζ_t (see Figure 20).

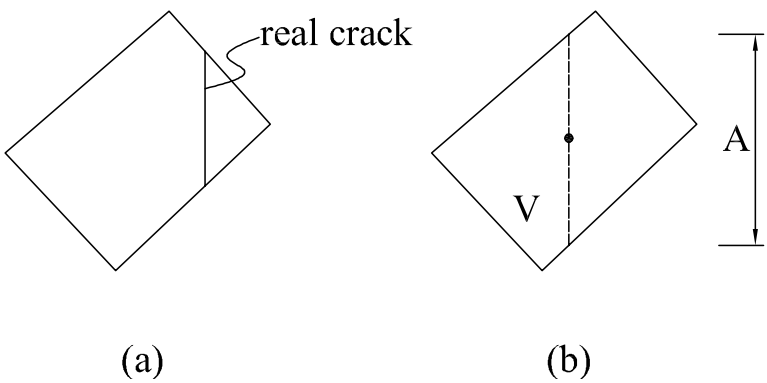

Figure 20: Determination of the crack area A in the modified SDA: (a) element experiencing cracking, (b) determination of A from a crack located at the center Gauss point

In fact, $s = A/V$ corresponds to the condition that the dissipated energy

E is the same as with SDA localization (see Figure 21), reading:

$$E = \int_A \left(\int_0^{\zeta_n} T_n \; d\zeta_n + \int_0^{\zeta_t} T_t \; d\zeta_t \right) dA \stackrel{!}{=} \int_\Omega \left(\int_0^{\boldsymbol{\varepsilon}^p} \boldsymbol{\sigma} : d\boldsymbol{\varepsilon}^p \right) d\Omega. \tag{39}$$

Introducing $\nabla\varphi = s\ \mathbf{n}$ into the expression for $\boldsymbol{\varepsilon}^p$ in Equation (24) yields $\boldsymbol{\varepsilon}^p = s\left[(\mathbf{n}\otimes\mathbf{n})\zeta_n + (\mathbf{t}\otimes\mathbf{n})^S\zeta_t\right]$, finally giving

$$\begin{aligned} E &= A\ \left(\int_0^{\zeta_n} T_n \; d\zeta_n + \int_0^{\zeta_t} T_t \; d\zeta_t \right) \\ &\stackrel{!}{=} V\ s\ \left(\int_0^{\zeta_n} \boldsymbol{\sigma} : (\mathbf{n}\otimes\mathbf{n}) d\zeta_n + \int_0^{\zeta_t} \boldsymbol{\sigma} : (\mathbf{t}\otimes\mathbf{n})^S d\zeta_t \right). \end{aligned} \tag{40}$$

As $T_n = (\mathbf{n}\otimes\mathbf{n}) : \boldsymbol{\sigma}$ and $T_t = (\mathbf{t}\otimes\mathbf{n}) : \boldsymbol{\sigma}$ according to Equation (30)[15], $s = A/V$ can be obtained directly from Equation (40).

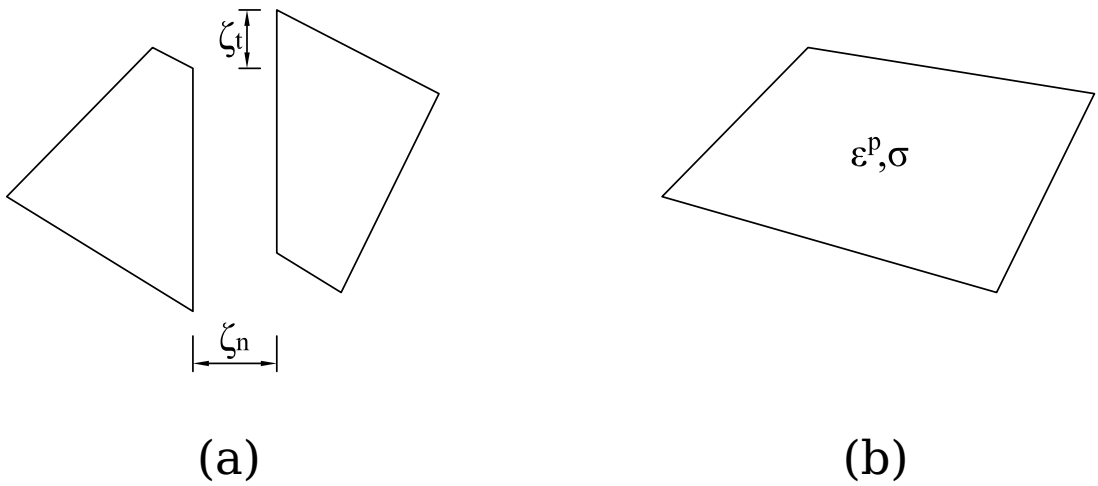

Figure 21: Strain localization: (a) element with a discrete crack, (b) element with SDA localization

The so-obtained modified SDA model corresponds to the statically optimal symmetric (SOS) formulation, where the stiffness matrix remains symmetric [104]. Although stress-locking in the SOS formulation is reported in [104, 105], locking of the quadrilateral element was eliminated, as will be illustrated in the next section.

The CST element[16], subjected to one load step [106], is employed to high-

[15] As $(\boldsymbol{\sigma})^S$ equals $\boldsymbol{\sigma}$, $(\mathbf{t}\otimes\mathbf{n}) : \boldsymbol{\sigma}$ equals $(\mathbf{t}\otimes\mathbf{n})^S : \boldsymbol{\sigma}$.

[16] Even though the CST element in the SOS formulation experiences stress-locking, which cannot be eliminated with tracking-strategy (see next section), this element is employed to illustrate the effect of the crack direction on the evolution of the plastic strains and the strain energy within the original SDA and the

light the beneficial effect of the modified SDA model (see Figure 22). For simplicity, no damage in the shear direction is assumed ($\zeta_t = 0$). Figure 23 shows the components of the plastic strain $\boldsymbol{\varepsilon}^p$ and the strain energy U for the original and the modified SDA model. Both $\boldsymbol{\varepsilon}^p(\theta)$ and $U(\theta)$ are continuous functions in the modified SDA model.

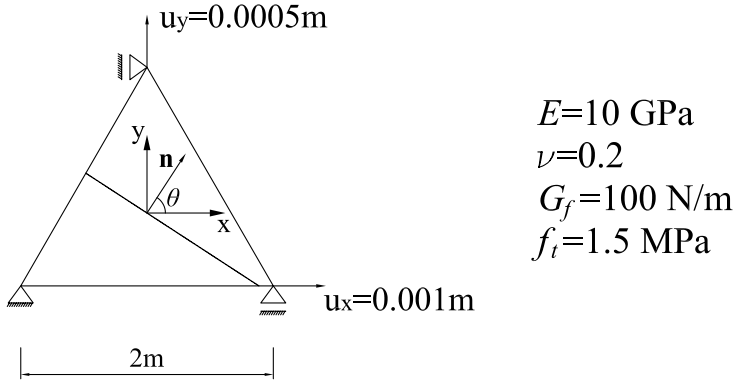

Figure 22: CST model: geometric properties and material parameters

Unlike the XFEM, allowing a continuous propagation of cracks, the energy-based crack-tracking in SDA is characterized by a mesh bias, as the propagation length is always connected to the element size. As a remedy, a smoothing technique (see Figure 24) is employed, using similar changes in the crack direction (see θ_{1S} in Step 2 and θ_{2S} in Step 4) for the two elements closest to the crack tip. Hereby, the change in the crack direction is determined from the mean value of the unsmoothed crack directions.

3.4 Elimination of stress-locking of quadrilateral elements with SOS formulation

The origin and the corresponding elimination of stress-locking in the SDA based on the SOS formulation is discussed, considering CASE 1 shown in Figure 14. The domain is discretized by two elements as illustrated in Figure 25.

Considering Figure 25(a), both CST elements become plastic during loading, whereas the crack area A (see Figure 20) is overestimated, resulting in "a zig-zag pattern" and in stress-locking [104], see the force-displacement curve

modified SDA.

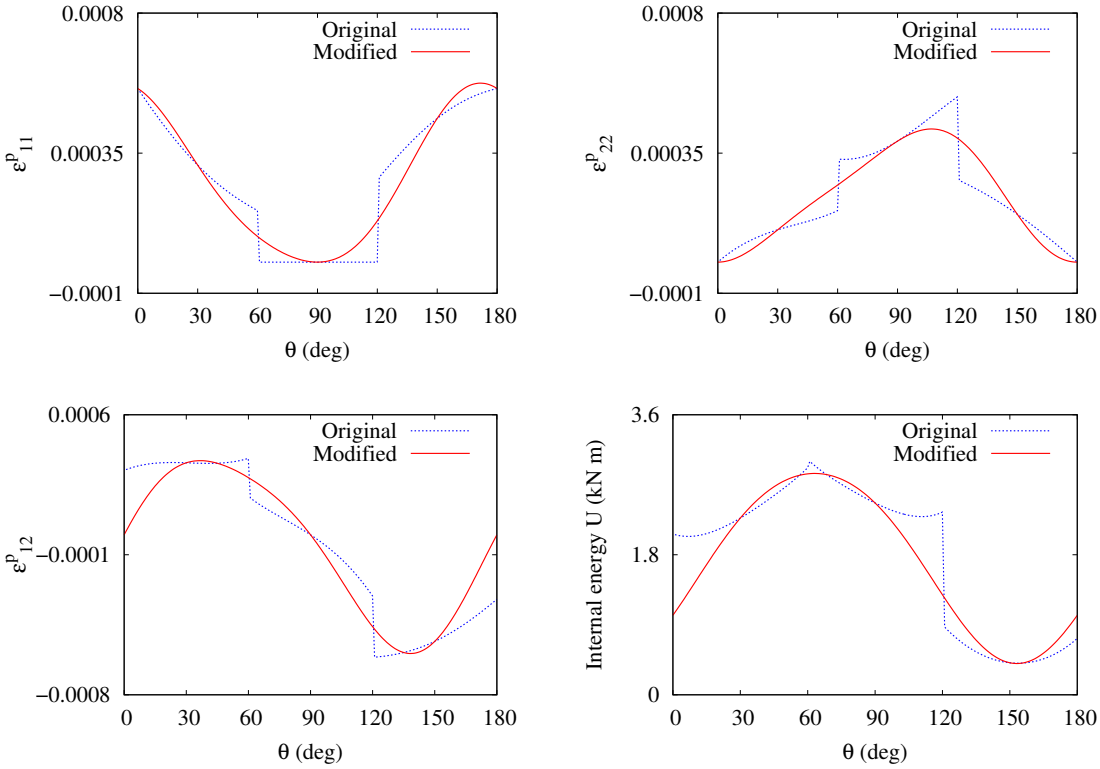

Figure 23: CST model: components of $\boldsymbol{\varepsilon}^p(\theta)$ and strain energy $U(\theta)$ as obtained by means of the original and the modified SDA model

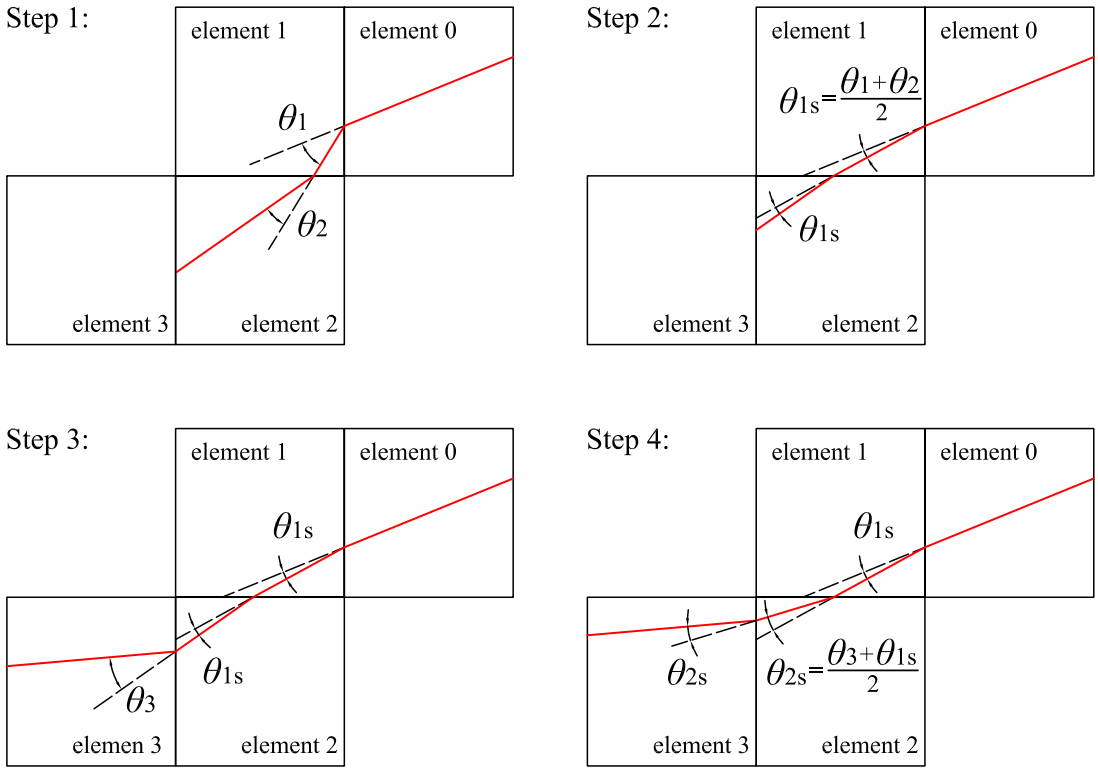

Figure 24: Smoothing technique for energy-based crack-tracking in the SDA

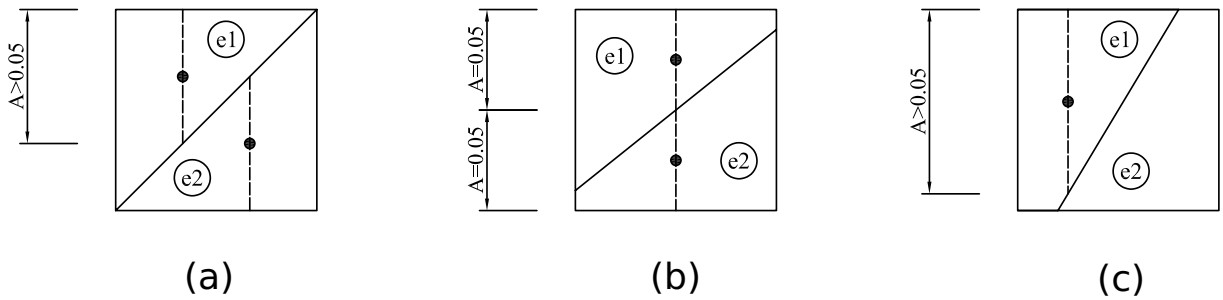

Figure 25: Finite-element discretization: (a) CST elements (b) quadrilateral elements (configuration 1) (c) quadrilateral elements (configuration 2)

in Figure 26. Unfortunately, stress-locking of the CST element cannot be eliminated by the underlying crack-tracking strategy.

Considering Figure 25(b), the crack area A is represented correctly, even in the unsymmetrical case. No stress-locking is encountered, see Figure 27.

Considering Figure 25(c), the crack area A which depends on the aspect ratio of the element, is underestimated. Only one element experiences plastic deformations, while the other one remains elastic. Even though the cohesive stress is underestimated in cases of elements with a large aspect ratio, stress-locking is not encountered, see Figure 28.

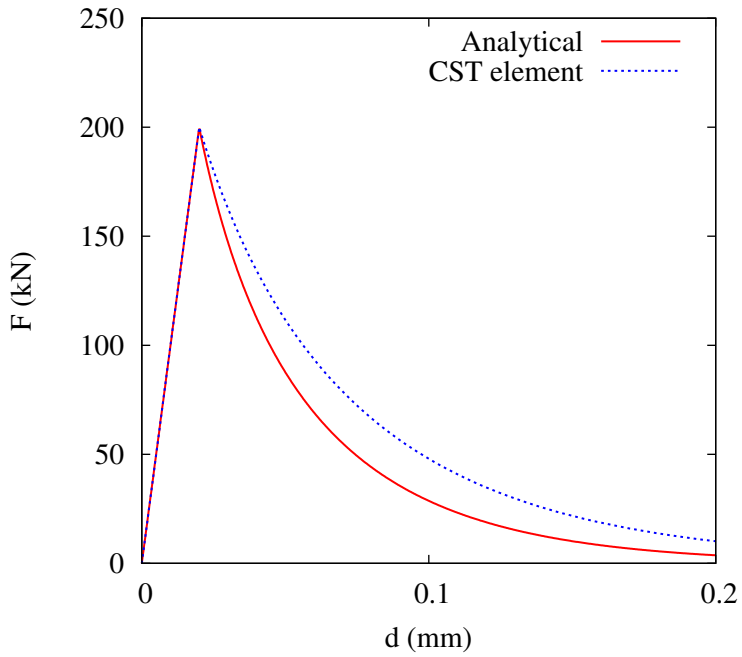

Figure 26: CASE 1 in Figure 14: force-displacement curve when using CST elements

3.5 Conclusions

In this section, a strong discontinuity approach (SDA) was adopted and implemented, using a higher-order element (eight-node quadrilateral element). Since the fixed-crack formulation of the SDA was used, a crack-tracking strategy became necessary in order to avoid stress-locking. For this purpose, the energy-based crack-tracking strategy, which is commonly used in the XFEM, was chosen, setting the orientation of the localized crack equal to the orientation of the real crack, with $\nabla\varphi$ parallel to $\mathbf{n}$, finally leading to the modified

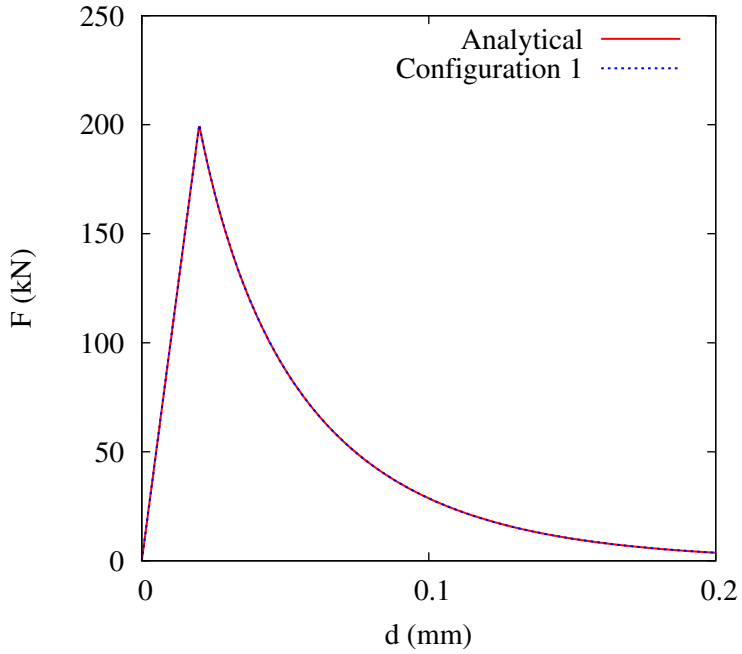

Figure 27: CASE 1 in Figure 14: force-displacement curve when using quadrilateral elements (Configuration 1 in Figure 25)

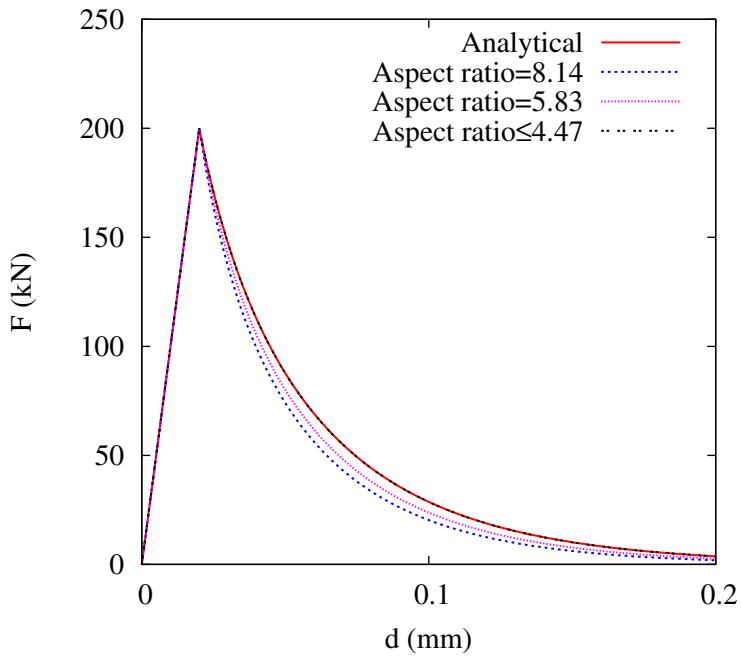

Figure 28: CASE 1 in Figure 14: force-displacement curve when using quadrilateral elements (Configuration 2 in Figure 25)

SDA approach. Moreover, a simple smoothing technique was applied for assisting the tracking strategy.

In summary, the proper combination of models and assumptions, comprising

- reduced integration for determination of stress/strain states of finite elements experiencing cracking,
- the assumption of the orientation of the localized crack and the real crack being parallel, and
- determination of the direction of cracking aiming at minimization of the total energy in the deformed body

yields an SDA approach that is applicable to higher-order elements with a continuous cracking path.

4 Applications

4.1 Removal of formwork of early-age concrete

In this section, the multifield approach is employed for the investigation of the effect of formwork removal (stripping) of early-age concrete, exposing the concrete surface to the outside environment, which may cause early-age cracking of concrete structures. The results from fully-coupled and weakly-coupled models (ignoring mass-transport) are compared. A modified convection coefficient α_V is introduced, in order to obtain similar results for the weakly-coupled and the fully-coupled models. Finally, the cracking risk of concrete members is evaluated with respect to the underlying mix-design, the size of the concrete member, and the stripping time, providing first insight into the influence of these parameters on the cracking risk of early-age concrete.

4.1.1 Simulation model and parameters

The model adopted in this thesis is shown in Figure 29, where H is the height of the model and R is the radius, with R $\gg$ H, in order to avoid boundary effects. The top and the bottom surface experience mass and energy exchange with the environment. The structural response is symmetric with respect to the x-axis (neutral plane). The employed material parameters are listed in

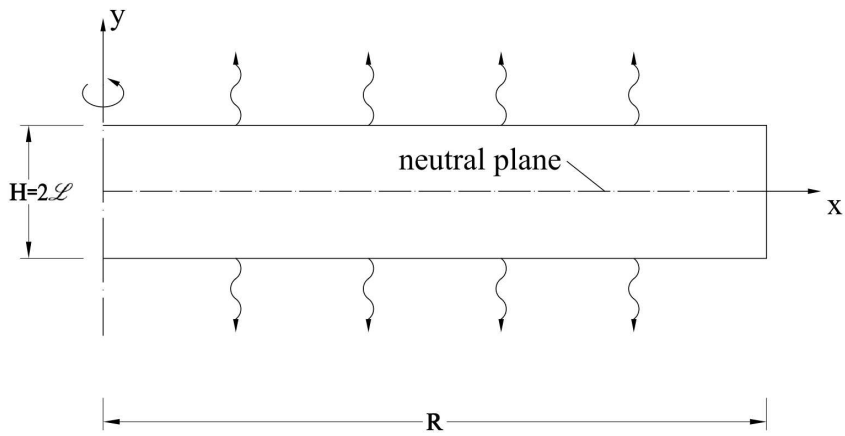

Figure 29: Axisymmetric model ($\mathscr{L}$: structural dimension of heat diffusion [12])

Table 5. The tensile and the compressive strength are taken from [12, 107,

Table 5: Material parameters of concrete employed in the simulation

Parameters	Units	OPC 045	OPC 055
w/c	-	0.45	0.55
m_{cem}	[kg]	390.44	345.40
$f_{t,\infty}$	[MPa]	2.6	2.3
$f_{c,\infty}$	[MPa]	35	30
$(\rho c_p)^{eff}$	[kJ m^{-3} K^{-1}]	2330.7	2330.7
k	[m^2]	$1 \cdot 10^{-18}$	$1 \cdot 10^{-18}$
λ^{eff}	[J s^{-1} m^{-1} K^{-1}]	1.9	1.9
$\partial \mathrm{Tr}(\mathbf{E}^T)/(3\ \partial T)$	[K^{-1}]	$1.2 \cdot 10^{-5}$	$1.2 \cdot 10^{-5}$

108]. The other parameters are taken from [11]. The parameters used in the analytical function for the chemical affinity $\tilde{A}$ are chosen as $a = 48$ s^{-1}, $b = 0.56$, and $c = 2.8$. The hydration heat of the cement is set equal to 340 kJ/(kg cement). The adiabatic temperature rise, measured in experiments taken from [11] (original data are obtained from [109]), is compared to the numerical simulation results in Figure 30, indicating perfect agreement. Information on the evolution of the elastic modulus, the porosity, Biot's coefficient, and the specific heat capacity of early-age concrete as functions of the hydration degree is provided in Figures 3 to 7. The strength of early-age concrete is assumed as a linear function of the hydration degree.

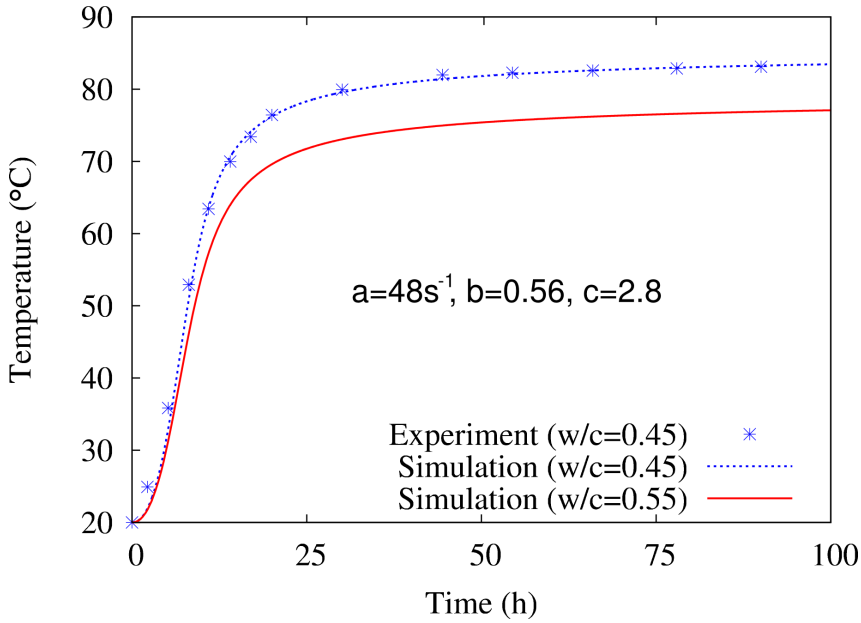

Figure 30: Comparison of adiabatic temperature results

Cauchy boundary conditions are adopted for the analysis of the multi-field processes in early-age concrete. When neglecting radiation, the energy balance equation at the boundary Ω is described by [110]:

$$\left(\lambda \text{grad } T - h\rho^w \frac{\mathbf{k}k^{rw}}{\eta^w} \text{grad } p^w\right)\Bigg|_{\Omega} = \alpha_T(T_b - T_\infty). \tag{41}$$

In order to model the water loss from the wetted concrete surface to the air, Menzel's equation [111] is modified for calculation of the water loss from the unsaturated concrete surface to the air. Hence, the moisture balance equation at the boundary (upper and lower surface in Figure 29) can be described by

$$\begin{aligned}&\left[\left(\rho^{gw}\frac{\mathbf{k}k^{rg}}{\eta^g}\text{grad } p^g\right) - \left(\rho^w \frac{\mathbf{k}k^{rw}}{\eta^w}\text{grad } p^w\right)\right.\\ &\left.-\rho^g \frac{M_a M_w}{M_g^2} D^{eff} \text{grad } \left(\frac{p^{gw}}{p^g}\right)\right]\Bigg|_{\Omega}\\ &= S\ Z_a(Rh_b\ p_{satb} - Rh_\infty\ p_{sat\infty})(Z_b + Z_c\ v),\end{aligned} \tag{42}$$

where $Z_a = 8.65 \cdot 10^{-8}$ kg m^{-2} s^{-1} Pa^{-1}, $Z_b = 0.253$, and $Z_c = 0.215$ s m^{-1} [112]. Though the overestimation of the water loss by Menzel's equation was pointed out in [113, 114], it is used in some research papers such as in [10]. Moreover, the ACI nomograph for estimating rate of evaporation of surface moisture from concrete [115] was obtained with Menzel's equation [112].

If mass-transport processes are neglected (weakly-coupled model), the temperature loss caused by vaporization cannot be considered. However, when considering Equation (42) and the specific enthalpy of vaporization h[17], an equivalent convection coefficient α_V[18] may be introduced as follows:

$$\begin{aligned}&(\lambda \text{grad } T)\Big|_{\Omega} = (\alpha_T + \alpha_V)(T_b - T_\infty),\\ &\text{with}\\ &\alpha_V = \frac{h\ S\ Z_a(Rh_b\ p_{satb} - Rh_\infty\ p_{sat\infty})(Z_b + Z_c\ v)}{T_b - T_\infty}.\end{aligned} \tag{43}$$

[17] In this case, the water loss of concrete surface m_{wl} are assumed to be all caused by vaporization with which the energy loss is obtained as $h\ m_{\text{wl}}$.

[18] α_V is the convection parameter considering the vaporization of water on the concrete surface.

In Equation (43), α_V is a function of the saturated vapor pressure p_{satb} and the relative humidity Rh_b on the concrete surface. The former is a function of the surface temperature T_b, with $p_{satb} = p_{satb}(T_b)$. Although the latter is unknown if mass-transport processes are disregarded, Equation (43) provides access to the range of α_V, considering $Rh_\infty \leq Rh_b \leq 1$. Accordingly, for an environmental temperature of $T_\infty = 20$ °C and an environmental relative humidity of $Rh_\infty = 0.6$, α_V is lying between the two curves shown in Figure 31.

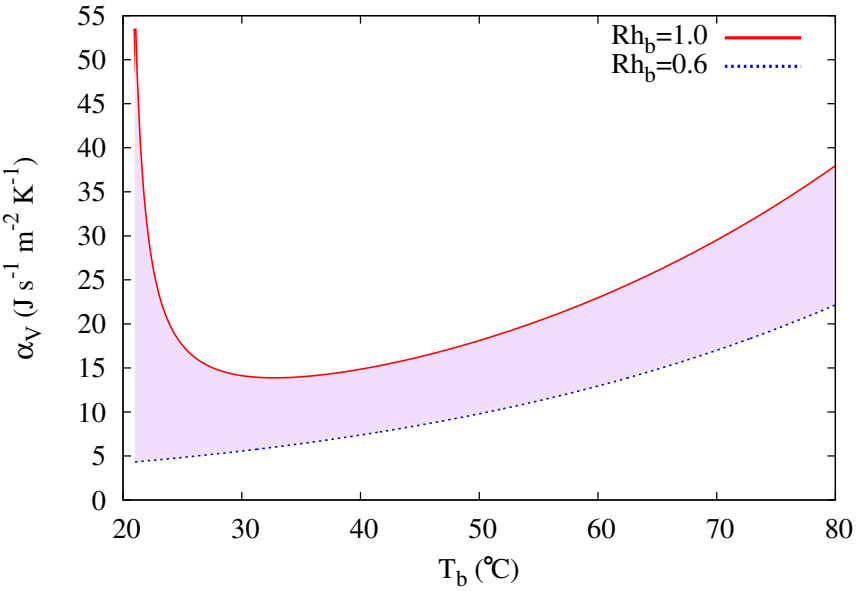

Figure 31: Range of the value of α_V for $T_\infty = 20$°C and $Rh_\infty = 0.6$

The initial temperature of concrete and the environmental temperature are set as $T_0 = T_\infty = 20$ °C. For the considered steel formwork, α_T is set equal to α_T of the free surface (as suggested in [12]), given as 4.0 J s^{-1} m^{-2} K^{-1}. Furthermore, it is assumed that the concrete has no mass exchange with the environment before removal of the formwork ($S = 0$), which is bare to the air after removal of the formwork ($S = 1$). The relative humidity of the environment is assumed constant: $Rh_\infty = 0.6$.

4.1.2 Fully-coupled versus weakly-coupled model

In this subsection, numerical simulations of a concrete member with $\mathscr{L} = 1.0$ m and different stripping times (24 h, 36 h, 48 h) are performed, considering both OPC 045 and OPC 055. Assuming the stress is mainly caused by

the temperature gradient along the y direction, the temperature difference $\Delta T = T(y = 0) - T(y = \mathscr{L})$ is taken for interpretation of the numerical results. According to Figures 32 and 33, the removal of the formwork induces vaporization and, hence, a thermal shock at the concrete surface. Vaporization occurs very fast and lasts for about 3 hours. After that, because of drying at the surface, vaporization stops. OPC 055 shows a larger increase of ΔT, which is explained by its larger w/c ratio, providing more water for vaporization at the surface. The stress is caused not only by the thermal gradient but also by drying shrinkage induced by vaporization, which can be assessed by comparing the different results from the fully-coupled and the weakly-coupled model as shown later.

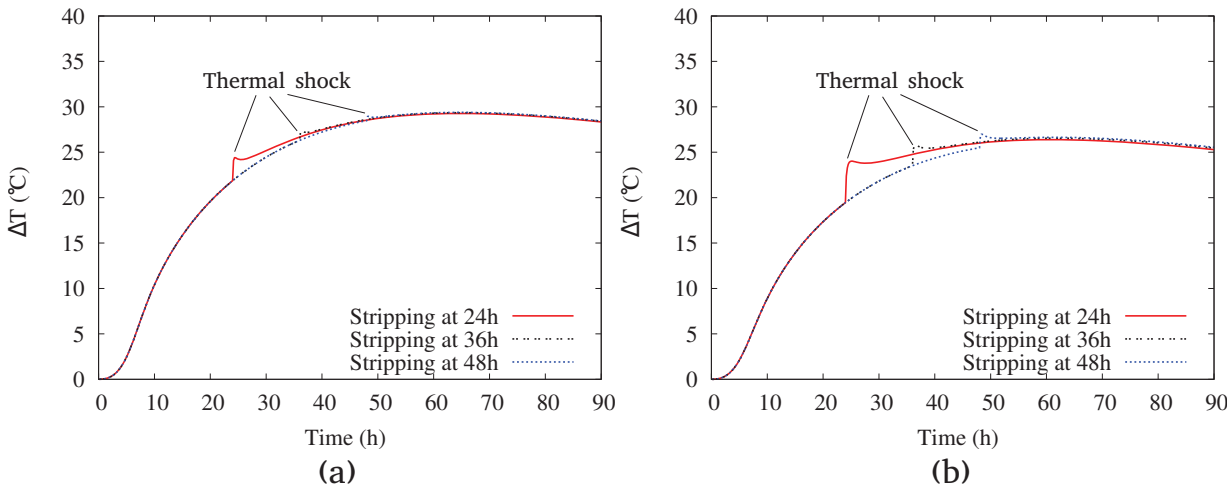

Figure 32: Evolution of ΔT for (a) OPC 045 and (b) OPC 055

Since the numerical results indicate that vaporization lasts for approximately three hours, a linear evolution of α_V with $Rh_b = 1.0$ at stripping and $Rh_b = Rh_\infty$ three hours after stripping is assumed during this time, resulting in the following empirical formula for α_V:

$$\alpha_V = A\,(B - t_s)\,(1 - t_e/3)\,, \tag{44}$$

where t_s [h] is the stripping time, $t_e = t - t_s$ [h] is the time elapsed after stripping, with $t_e \leq 3$ h, and A and B are parameters depending on the concrete type and stripping time: for OPC 045 and $t_s = 24$ h: $A = 225$ J h^{-3} m^{-2} K^{-1}, $B = 56$ h, for OPC 055 and $t_s = 24$ h: $A = 600$ J h^{-3} m^{-2} K^{-1}, $B = 60$ h.

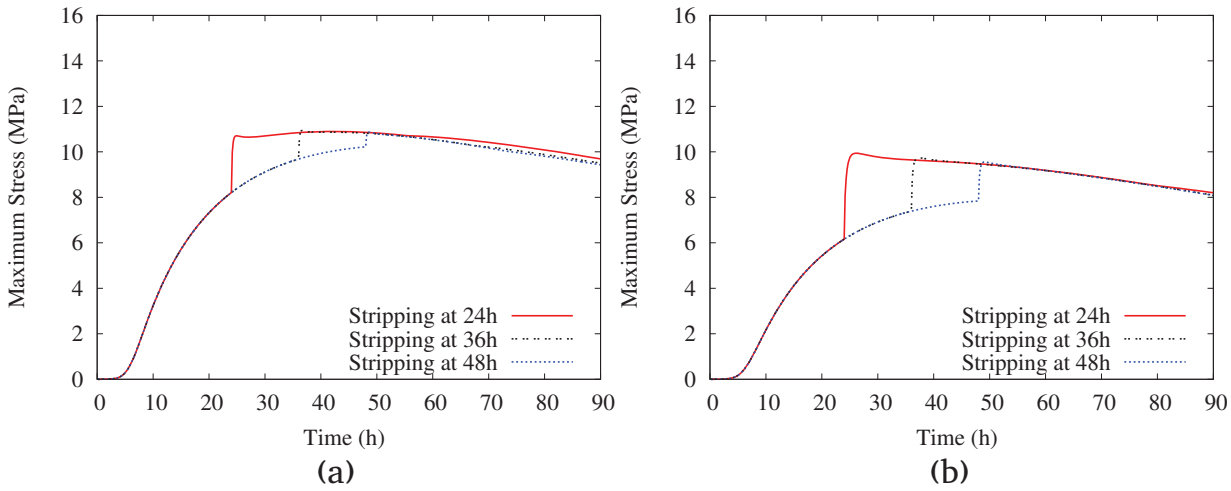

Figure 33: Evolution of the maximum stress on the surface for (a) OPC 045 and (b) OPC 055

The results obtained from the fully-coupled and weakly-coupled model (ignoring mass-transport) for a stripping time $t_s = 24$ h are shown in Figures 34 and 35. It is shown that the weakly-coupled model, with α_V calculated from Equation (44), produces similar results for ΔT as the fully-coupled model. However, the stress induced by vaporization consists of two parts: the thermal stress and the shrinkage stress. The weakly-coupled model cannot predict shrinkage, leading to underestimation of the stress increase caused by the removal of the formwork. According to Figure 35, the value of the shrinkage stress is approximately of the order of the thermal stress.

4.1.3 Relationship between the cracking risk, the size and the stripping time

Focusing on the cases discussed in this thesis, the maximum stress always occurs at the surface of the concrete member, additionally showing the smallest value of the hydration degree and, thus, the smallest strength. Accordingly, the cracking risk is defined as the ratio of the maximum stress to the tensile strength at the surface, with values greater than one indicating early-age cracking. Hereby, the tensile strength f_t is assumed to increase linearly with increasing hydration degree, i.e.,

$$f_t(\xi) = f_{t,\infty}\frac{\xi - \xi_0}{1 - \xi_0}, \tag{45}$$

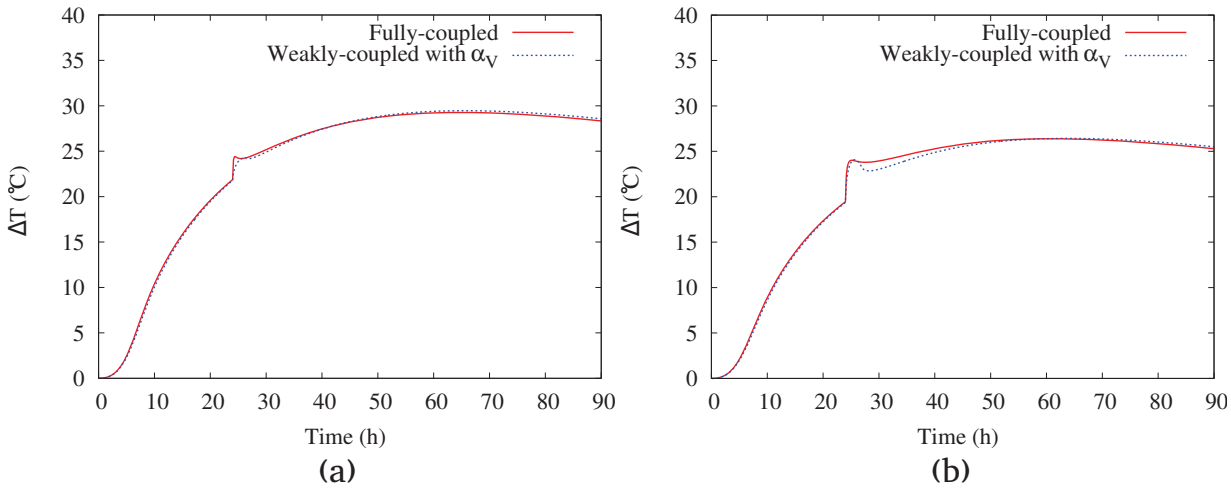

Figure 34: Evolution of ΔT (fully-coupled vs weakly-coupled), when stripping at 24 h for (a) OPC 045 and (b) OPC 055

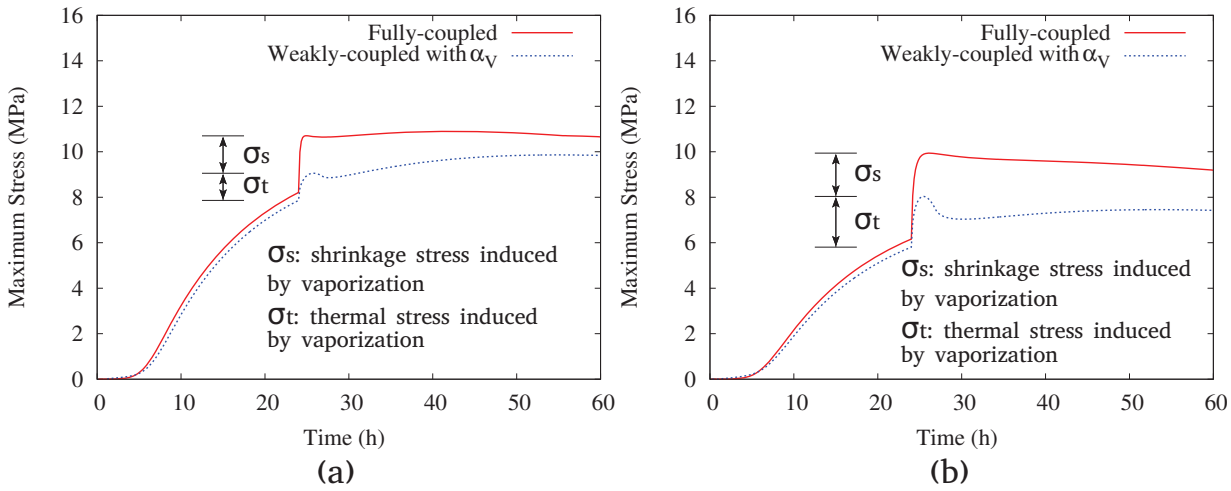

Figure 35: Evolution of the maximum stress (fully-coupled vs weakly-coupled) at the surface, when stripping at 24 h for (a) OPC 045 and (b) OPC 055

where the percolation threshold ξ_0 is set equal to 0.01. Figure 36 contains contour lines for the maximum value of the cracking risk as a function of the stripping time and the thickness of the concrete members, with $\mathscr{L}$ = H/2. From these results, the following conclusions can be drawn:

- The cracking risk decreases with postponement of stripping, with a reduction of about 20% to 40% per day.
- The cracking risk of OPC 045 is slightly higher than that of OPC 055, mainly because of its greater temperature rise associated with hydration (see Figure 30).
- Postponement of stripping has a higher impact in case of OPC 055 than in case of OPC 045, with the higher w/c ratio of OPC 055 resulting in more severe vaporization.
- For structures with a larger value of $\mathscr{L}$, postponement of stripping has limited influence, which is explained by cracking of massive concrete being mainly controlled by the thermal field, while vaporization lasts only for a short time (about three hours, see Section 4.1.2). Compared to the thermal stress in massive concrete, the additional stress caused by vaporization is found to be almost negligible.

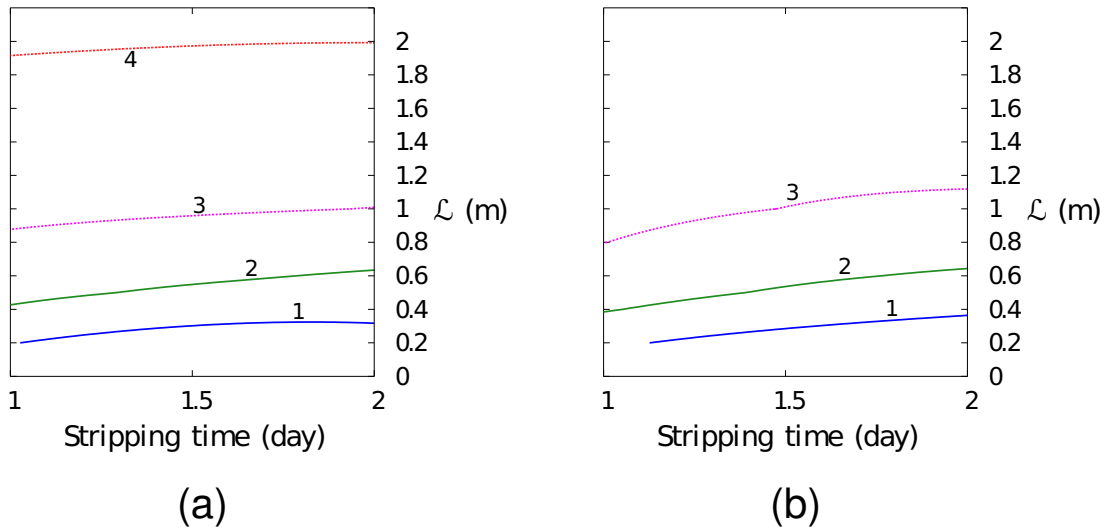

Figure 36: Contour lines of maximum cracking risk as a function of the stripping time and of $\mathscr{L}$ for (a) OPC 045 and (b) OPC 055

4.1.4 Conclusions

In this subsection, the developed multifield framework was applied to the analysis of formwork removal of early-age concrete. The main conclusions are as follows:

- The removal of the formwork causes both thermal stress and shrinkage stress. While the former can be simulated by a weakly-coupled model with a modified convection coefficient (as demonstrated in this thesis), the latter can only be assessed by means of using a fully-coupled model.
- Based on the results from parameter studies, the correlation between the cracking risk, the stripping time, and the size of the concrete member is investigated. Contour lines of the maximum cracking risk facilitate the specification of the stripping time with which the risk of early-age cracking is minimized.

4.2 Spalling risk of concrete subjected to fire loading

Employing an axisymmetric model that represents plate-like concrete structures such as slabs, walls, and tunnel linings, the effect of material properties (intrinsic permeability, porosity) and environmental conditions (saturation degree) on spalling is investigated. The obtained numerical results provide insight into the spalling risk for a wide range of material properties and environmental conditions. Based on the obtained results, the spalling risk of an Austrian highway tunnel is assessed.

4.2.1 Numerical model and parameters

Accounting for the stress state in fire-loaded concrete members, the effect of biaxial compression on the out-of-plane tensile stress at failure is considered (see Figure 37). The tensile strength of concrete subjected to biaxial compression at high temperature is given as

$$f_t(\sigma_b, T) = f_t(0, T)\frac{\sigma_b + f_b(T)}{f_b(T)}, \tag{46}$$

where $f_t(0, T)$ is the temperature-dependent uniaxial tensile strength of concrete, σ_b ($\sigma_b < 0$) is the in-plane compressive stress parallel to the heated surface (see Figure 37(a)), and $f_b(T)$ is the temperature-dependent biaxial compressive strength deduced from experimental results, given by [116, 117]:

$$\begin{cases} f_b(T) = 1.16\ f_{c,0} & T < 100°\text{C}, \\ f_b(T) = \left[-2.64 \cdot 10^{-6}\,(T-100)^2 + 1.16\right] f_{c,0} & 100°\text{C} \leq T \leq 600°\text{C}, \\ f_b(T) = 0.0 & T > 600°\text{C}. \end{cases} \tag{47}$$

As mentioned previously, fire loading and spalling in plate-like concrete structures are considered in the present numerical study (see Figure 38(a) and (b)). For this purpose, an axisymmetric model as shown in Figure 38(c) is employed, yielding a biaxial in-plane stress state, with $\sigma_r = \sigma_\varphi$.

The material parameters for concrete at room temperature are listed in Table 6. The relationship between the elastic modulus E and the temperature follows from the experimental data in [118], see Figure 39(a). The relationship between the uniaxial tensile strength $f_t(0, T)$ and the temperature is taken

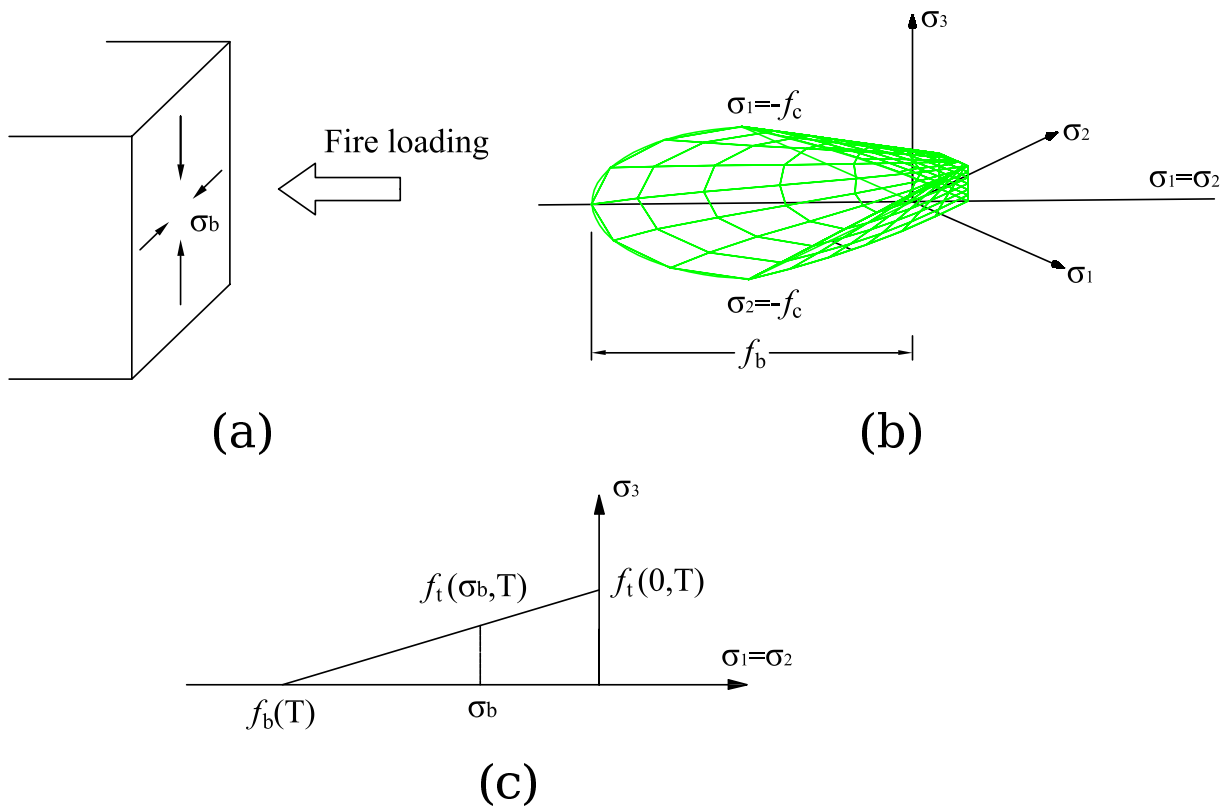

Figure 37: Decrease of tensile strength in consequence of biaxial compressive loading: (a) biaxial compression induced by fire loading, (b) yield surface at the domain $\sigma_3 > 0$, (c) simplified linear criterion corresponding to the yield surface at $\sigma_1 = \sigma_2$ and $\sigma_3 > 0$

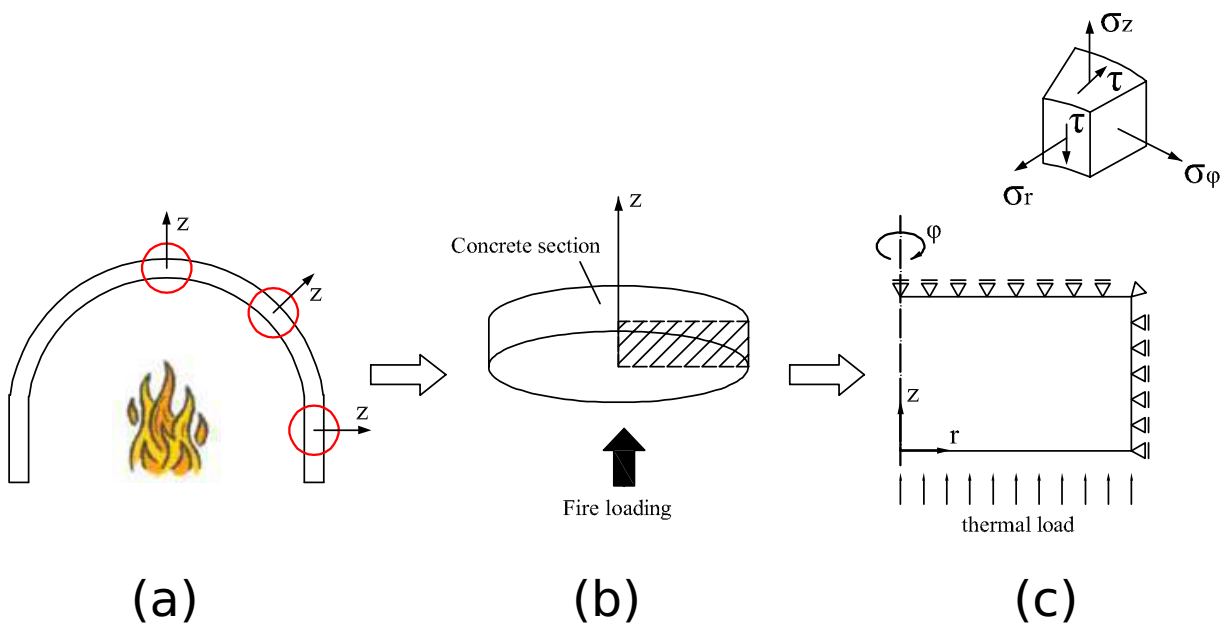

Figure 38: Numerical model for simulation of spalling: (a) tunnel lining subjected to fire loading, (b) concrete section under fire loading and (c) simplified axisymmetric model

from [119]. The relationship between the intrinsic permeability k and the temperature is given in [120]. The relationship between the thermal strain E^T and the temperature is given in [119][19].

Table 6: Material parameters (values at room temperature)

Water/cement ratio	(-)	0.45
Modulus of elasticity E	(GPa)	38.2
Poisson's ratio ν	(-)	0.2
Tensile strength $f_{t,0}$	(MPa)	3.0
Compression strength $f_{c,0}$	(MPa)	40.0
LITS factor k^{LITS}	(-)	1.0
Intrinsic permeability k_0	(m^2)	10^{-17}, 10^{-18}
Initial saturation degree $S_{w,0}$	(-)	0.4, 0.6, 0.8
Thermal conductivity λ	(J s^{-1} m^{-1} K^{-1})	1.9
Specific heat c_p	(J kg^{-1} K^{-1})	900
Initial porosity n	(-)	0.1, 0.15
Concrete density ρ	(kg m^{-3})	2400

As regards the thermal boundary condition at the heated surface, both convection and radiation are considered. The corresponding heat flux q_T is determined as

$$q_T = \alpha\ (T - T_\infty) + e\ \sigma\ (T^4 - T_\infty^4), \tag{48}$$

where $\alpha = 25$ W/(m^2 K), $e = 0.56$ is the emissivity of concrete and $\sigma = 5.67 \cdot 10^{-8}$ W/(m^2 K^4) is the Stefan-Boltzmann constant. Fire-loading is considered by means of a linear increase of T_∞ from 20 °C to 1200 °C within the first 300 s. Thereafter, T_∞ is kept constant at 1200 °C [121, 122].

4.2.2 Numerical analysis

Based on the effective-stress theory (Equation (16)) and the underlying numerical model, the stress that is responsible for spalling, σ_z, is obtained as:

$$\sigma_z = \Sigma_z + \mathrm{b}^{hom} p^g = \mathrm{b}^{hom} p^g. \tag{49}$$

Additionally, based on the in-plane biaxial stress state, the tensile strength is determined from Equation (46) as $f_t(\sigma_r, T)$, allowing to introduce the so-

[19]The curve adopted in this thesis has been suggested for concrete with siliceous aggregates.

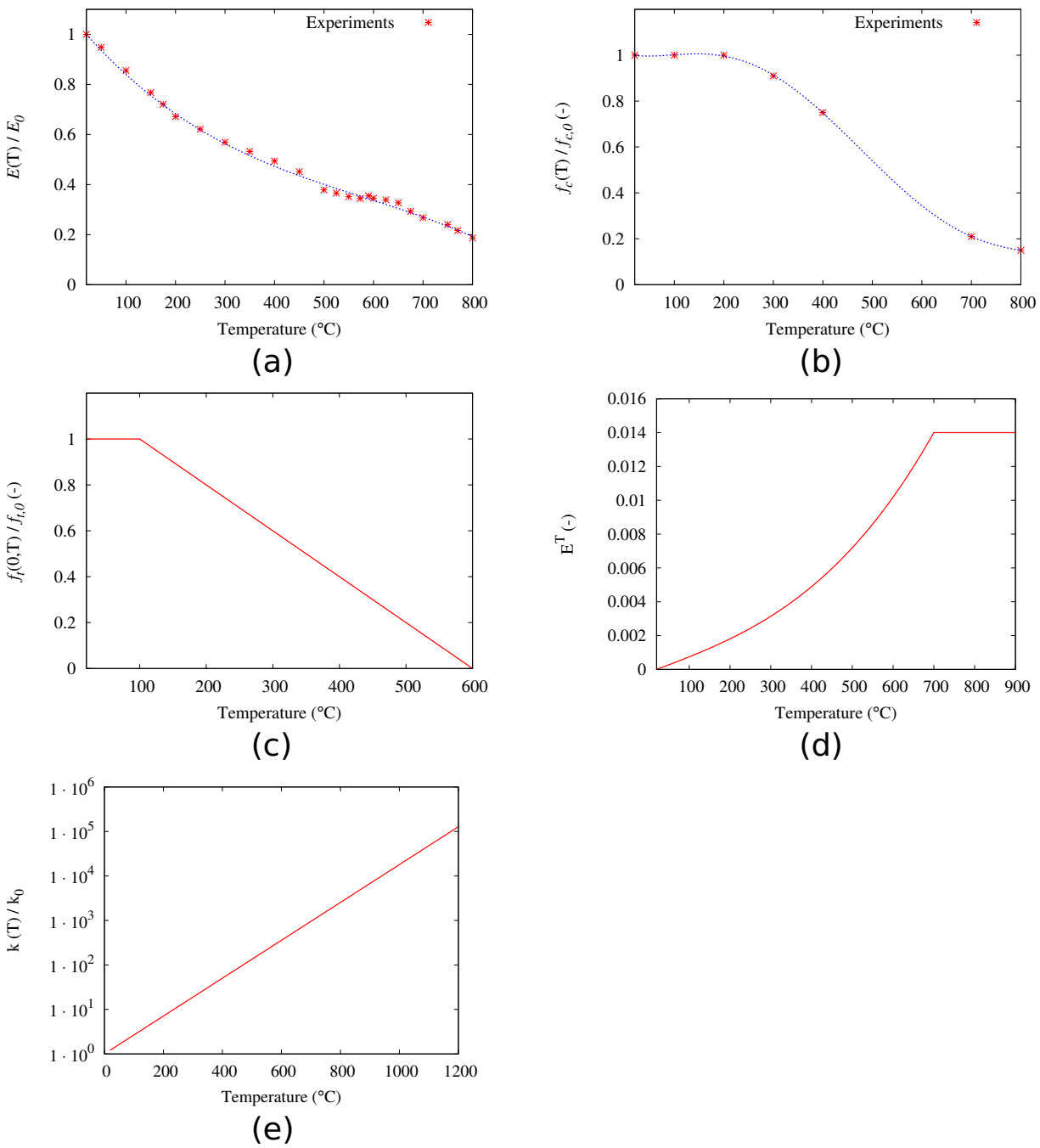

Figure 39: Parameters as functions of the temperature T: (a) elastic modulus and corresponding experimental results in [118], (b) uniaxial compressive strength and corresponding experimental results in [118], (c) uniaxial tensile strength, (d) thermal strain E^T, (e) intrinsic permeability k

called level of loading L, defined as

$$\mathrm{L} = \frac{\sigma_z}{f_t(\sigma_r, T)}. \tag{50}$$

This quantity provides insight into the risk of spalling. The stress σ_z that is building up in the course of fire loading and the corresponding level of loading are illustrated for three parameters which are used later on in the content of risk assessment. In the following, details of this assessment are described:

1. In order to illustrate the influence of the intrinsic permeability on the stress state, results after 235 s of fire loading are shown in Figure 40. According to Figure 40(b), $f_t(\sigma_r, T)$ and σ_z along the depth of the concrete member give $\mathrm{L} = 1$ for $\mathrm{k}_0 = 10^{-18}$ m^2, indicating the initiation of spalling. The results reveal that low intrinsic permeability yields an increase of the gas pressure. Consequently, the spalling risk of fire-loaded concrete is increasing.

2. Figure 41 shows the influence of the initial saturation degree on the stress state. The results reveal that a high saturation degree gives an increase of the gas pressure, favouring the initiation of spalling. For the considered saturation degrees, spalling occurs earlier with increasing saturation and, thus, at lower temperature loading.

3. Figure 42 shows the influence of the initial porosity on the stress state in the concrete. For increasing porosity and given initial saturation and, thus, increasing amount of water, the gas pressure increases, leading to earlier initiation of spalling.

According to the previous results, the risk of spalling is strongly influenced by the intrinsic permeability k_0, the initial saturation degree $S_{w,0}$, and the initial porosity n. In order to assess the risk of spalling, contour plots representing functions of $S_{w,0}$ and n are shown in Figures 43 to 45. Hereby, the zones above the contour lines indicate a high explosive spalling risk whereas the zones below the contour lines indicate a low explosive spalling risk. Furthermore, the water-mass ratio (WMR), corresponding to porosity and saturation, is included in Figures 43 to 45, enabling an assessment of the spalling risk when considering WMR only, as will be discussed in the following section.

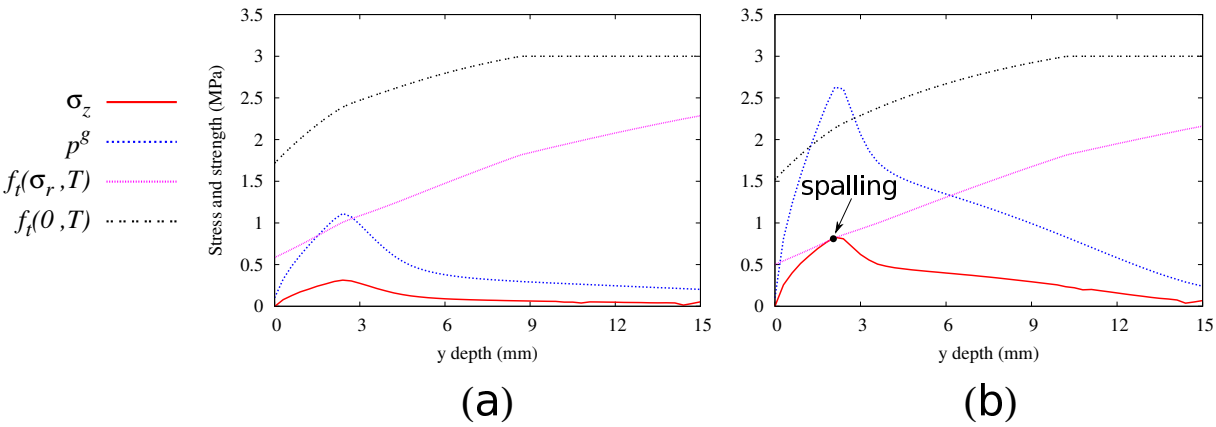

Figure 40: Stress state after 235s of fire loading: Concrete with $S_{w,0} = 0.8$, $n = 0.15$, and (a) $k_0 = 10^{-17}$ m^2, (b) $k_0 = 10^{-18}$ m^2

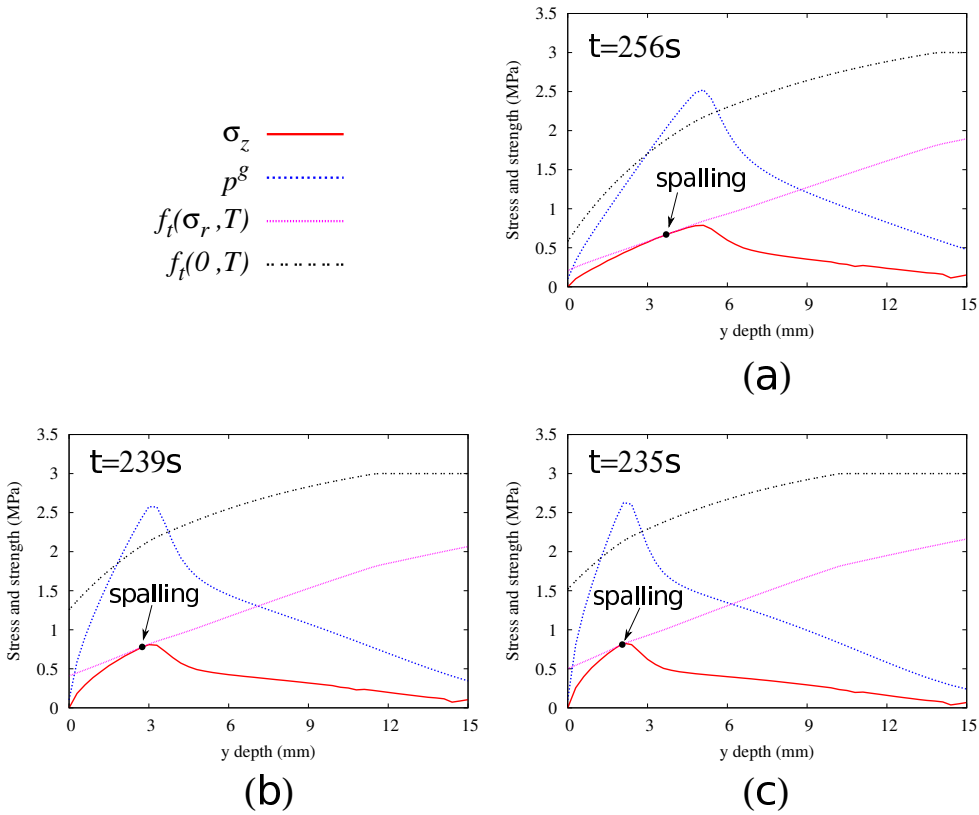

Figure 41: Stress state after different periods of fire loading: Concrete with $k_0 = 10^{-18}$ m^2, $n = 0.15$, and (a) $S_{w,0} = 0.4$, (b) $S_{w,0} = 0.6$, and (c) $S_{w,0} = 0.8$

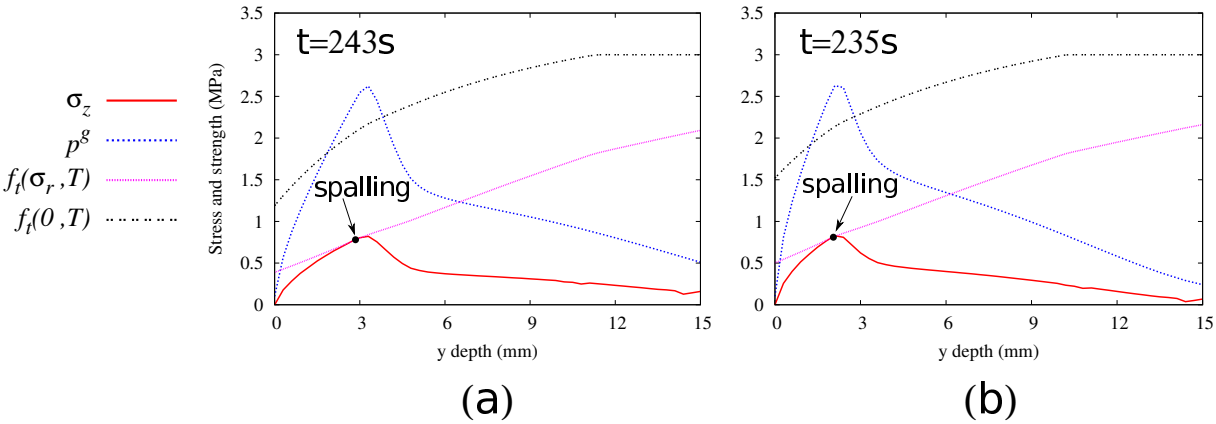

Figure 42: Stress state after different periods of fire loading: Concrete with $k_0 = 10^{-18}$ m^2, $S_{w,0} = 0.8$, and (a) $n = 0.10$, (b) $n = 0.15$

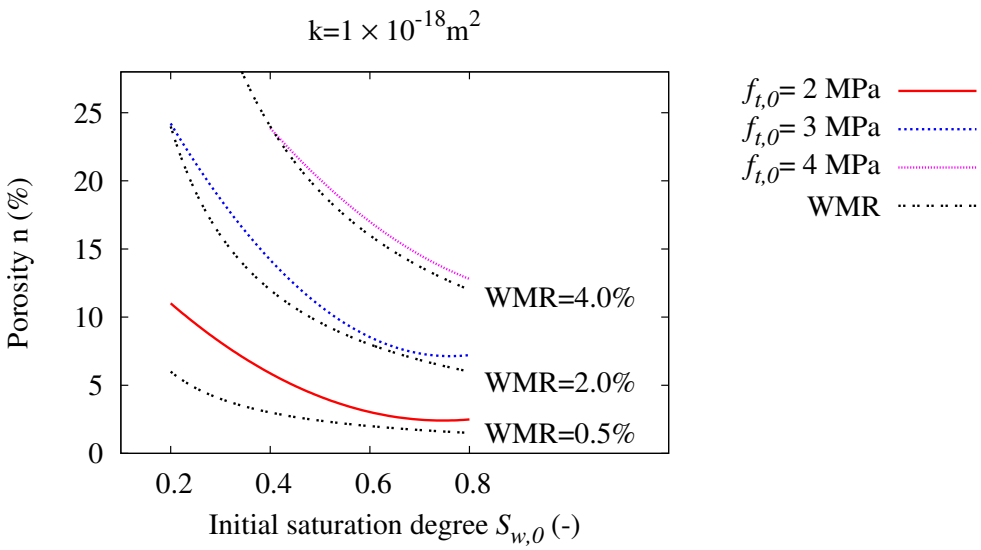

Figure 43: Spalling risk of concrete with $k_0 = 1 \cdot 10^{-18}$ m^2 as a function of $S_{w,0}$ and n (WMR: water-mass ratio, given by WMR=$n\ S_{w,0}\ \rho^w/\rho = 0.4167\ n\ S_{w,0}$, with the concrete density as $\rho = 2400$ kg/m^3, and the water density as $\rho^w = 1000$ kg/m^3)

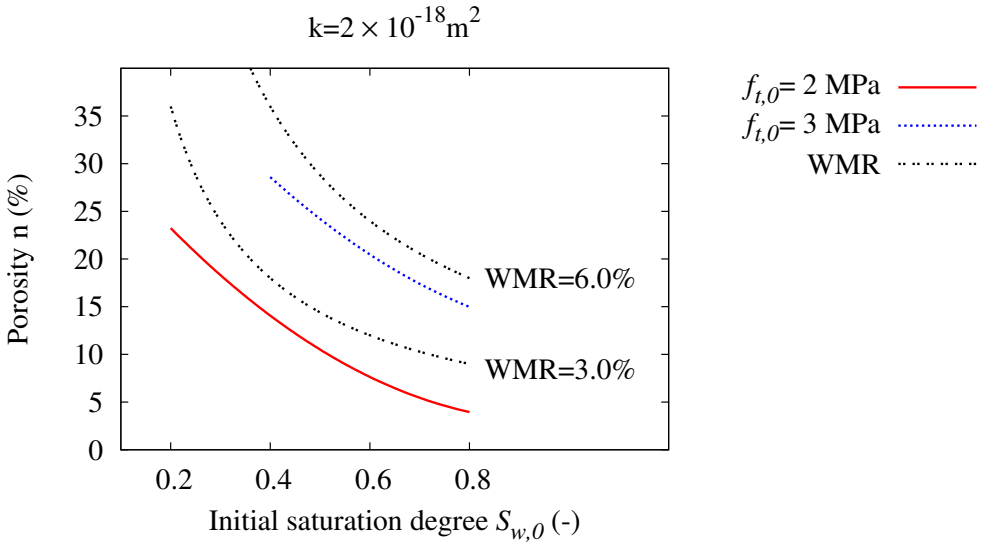

Figure 44: Spalling risk of concrete with $k_0 = 2 \cdot 10^{-18}$ m^2 as a function of $S_{w,0}$ and n

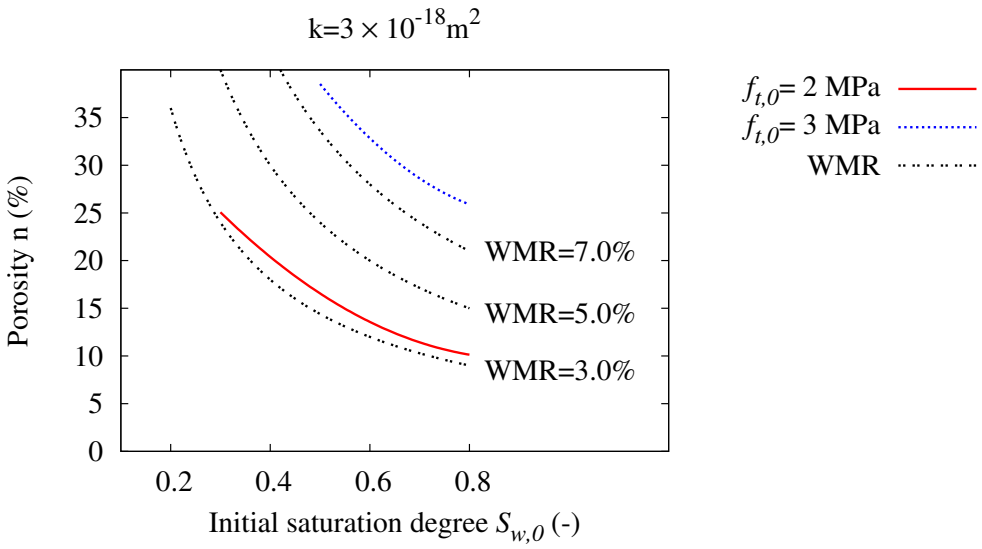

Figure 45: Spalling risk of concrete with $k_0 = 3 \cdot 10^{-18}$ m^2 as a function of $S_{w,0}$ and n

4.2.3 Application to spalling risk assessment of tunnel linings

As an example for the application of the presented concept, a tunnel in Austria, built in the 1970s, is considered for assessing the spalling risk, see Figure 46. The type of concrete used for the lining is C25/C30. The compressive strength of concrete, $f_{c,0}$, is assumed as 35 MPa and the tensile strength, $f_{t,0}$, as 3 MPa. Within two representative sections, the water content (water-mass ratio, WMR) was determined at different heights of the section, see Figure 47. The obtained results are listed in Table 7.

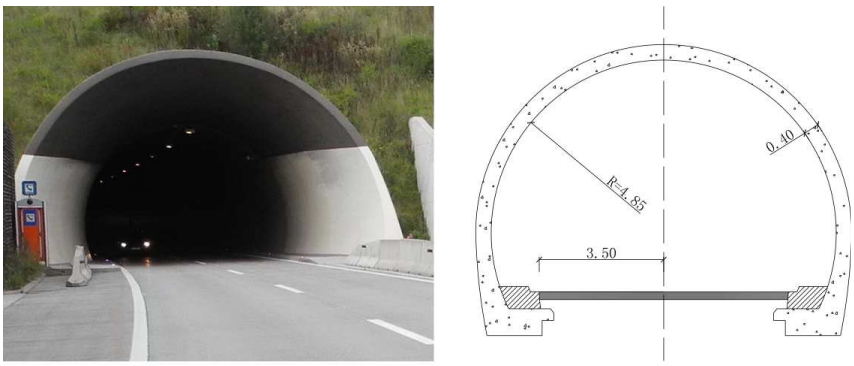

(a) (b)

Figure 46: Tunnel in Austria considered as an application example: (a) tunnel entrance, and (b) cross section of the tunnel

Figure 47: Tunnel in Austria considered as an application example: drilling work for determination of the water-mass ratio

The porosity and the intrinsic permeability were assumed on the basis of the concrete mix design. They were varied in the course of the risk as-

Table 7: Water-mass ratios of the tunnel section

Height	Section 1	Section 2
0.3m	2.5%	4.1%
1.0m	3.5%	6.3%
1.6m	3.9%	6.8%
2.0m	3.2%	6.6%

sessment. This has resulted in a contour plot (see Figure 48), where the saturation is also a variable (according to the variation of the water-mass ratio, see Table 7). Based on measured water-mass ratios, it can be concluded that the tunnel is at high risk of spalling for an intrinsic permeability smaller than $1 \cdot 10^{-18}$ m^2, since all measured water-mass ratios are found above the corresponding contour line. The tunnel is at low risk of spalling for an intrinsic permeability greater than $3 \cdot 10^{-18}$ m^2, since all measured data for the water-mass ratios are found below the corresponding contour line. Since the range of the intrinsic permeability separating the high and low risk (low spalling risk if k $> 3 \cdot 10^{-18}$ m^2, and high spalling risk if k $< 1 \cdot 10^{-18}$ m^2) in the presented case is very small, measurement of the actual intrinsic permeability of the tunnel-lining concrete is necessary before giving a definite and reliable assessment of the spalling risk of the investigated tunnel. For that purpose, various on-site and laboratory test methods are available [120, 123].

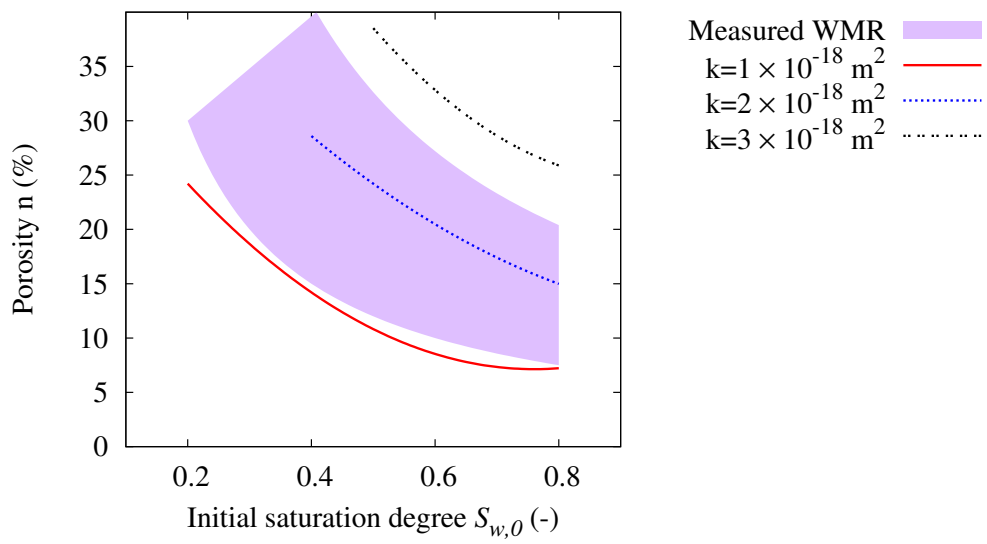

Figure 48: Spalling risk of the investigated tunnel ($f_{c,0} = 35$ MPa, $f_{t,0} = 3$ MPa)

4.2.4 Conclusions

In this section, a coupled thermo-hydro-chemo-poro-mechanical model for assessing the spalling risk of concrete subjected to fire-loading is adopted. Parameter studies have led to contour plots as functions of the main material and environmental parameters responsible for spalling. These plots have shown the following effects:

- Effect of intrinsic permeability: the risk of spalling increases with decreasing intrinsic permeability, because the gas pressure is more quickly accumulated.
- Effect of porosity: in case the saturation remains unchanged, the risk of spalling increases with increasing porosity caused by the increasing amount of water which evaporates during heating.
- Effect of saturation: the risk of spalling increases with increasing saturation, because of the increasing amount of water which evaporates during heating and the lower relative gas permeability.
- Effect of concrete strength: the risk of spalling increases with decreasing concrete strength[20].

With the obtained contour plots, the spalling risk of an Austrian tunnel was assessed by means of the measured water content (water-mass ratio) which served as the input parameter. The results from this assessment highlights the sensitivity of the high/low spalling risk with respect to the intrinsic permeability, necessitating permeability measurements (on-site or in the laboratory) for a final assessment of the spalling risk based on the presented contour plot.

[20] In reality, concrete with higher strength usually is denser, exhibiting a lower intrinsic permeability, which results in an increase of the risk of spalling.

4.3 Simulation of fracturing of concrete members

In the numerical simulations in this section, the parameter for further crack propagation within the presented SDA is set equal to $\gamma = 30°$, with $\Delta\gamma = 3.0°$ (see Figure 18). If the angle giving the minimum total energy is found at the boundaries (0° or 30°), γ will be increased and the tracking process will be repeated. For specification of the crack angle in a newly-cracked element, 10 iteration steps (as recommended in [87]) are considered.

4.3.1 Three-point bending test

The set-up and the material properties of the three-point bending test, which was experimentally investigated in [124], are shown in Figure 49. The load is applied under displacement control, with an increase of the displacement of 0.1 mm per step. For the numerical study, two different discretizations are considered (see Figure 50).

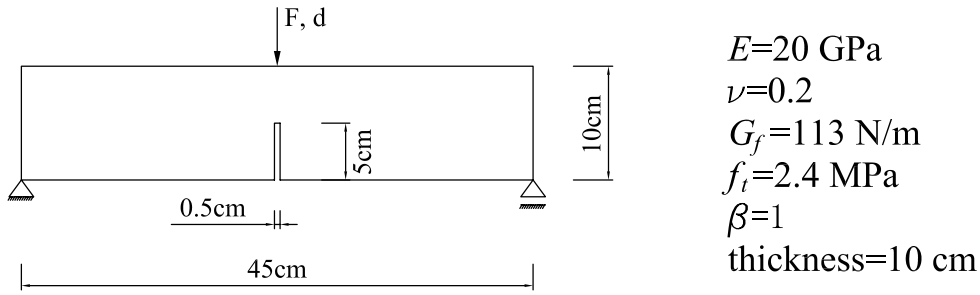

Figure 49: Three-point bending test: geometric properties and material parameters

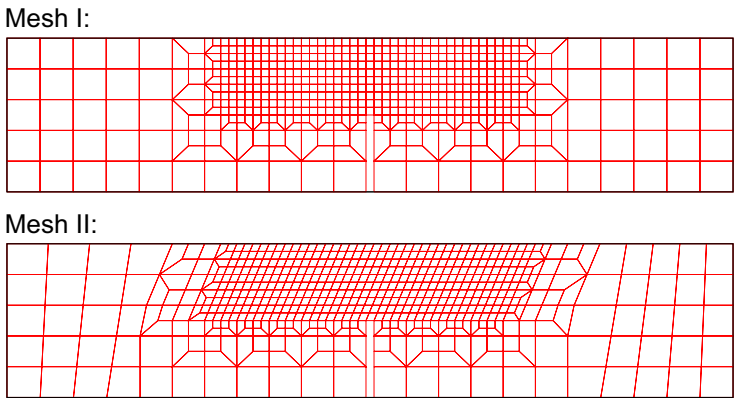

Figure 50: Three-point bending test: discretizations considered in the numerical investigation

The obtained results for the crack path and the force-displacement curve are shown in Figures 51 and 52, indicating little influence of the mesh on the crack path. Considering the force-displacement curves, both meshes provide reasonable values for the peak-load. Moreover, the results for the post-peak behaviour are also reasonable. No locking is encountered.

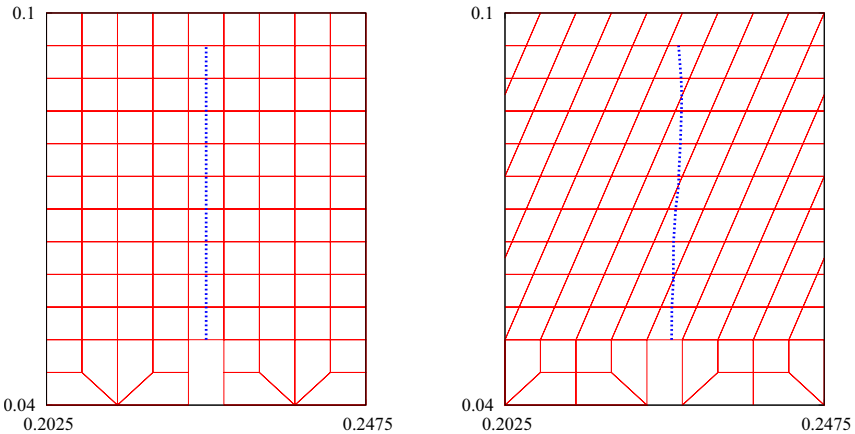

Figure 51: Three-point bending test: numerically-obtained crack paths

4.3.2 L-shaped panel test

The geometric dimensions, the material parameters, the loading and the boundary conditions of the L-shaped panel, experimentally investigated in [125], are shown in Figure 53. Four different discretizations are considered in the numerical study (see Figure 54).

The results for the crack path are shown in Figure 55. The crack paths are located in the upper area of the experimental range. This can be explained by the small shear stiffness considered in the analysis by having set $\beta = 1$, see [87].

The force-displacement curves are shown in Figure 56. For the coarse mesh (Mesh I) and the irregular mesh (Mesh IV) a slightly oscillating behaviour is observed. This can be explained by delayed plastification of elements when adopting reduced integration (elements become elastoplastic only after their center Gauss point indicates the occurrence of elastoplastic strains). For the finest mesh, no oscillations are observed in the force-displacement curve (see Mesh III in Figure 56). As regards the post-peak behaviour, similar results for all considered meshes are encountered. There is no locking.

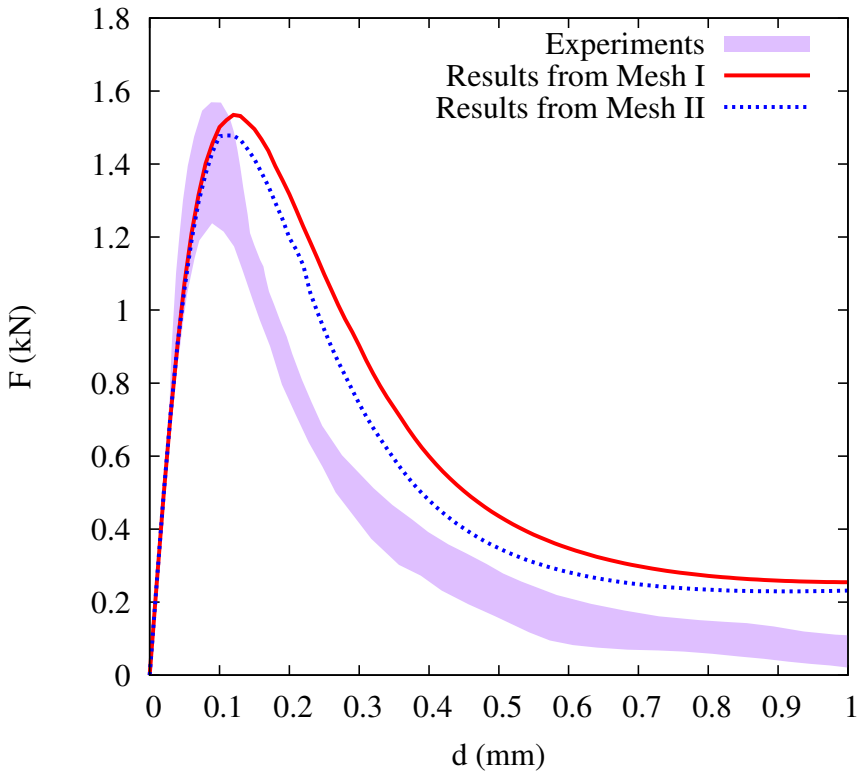

Figure 52: Three-point bending test: numerically-obtained force-displacement curves and experimental results presented in [124]

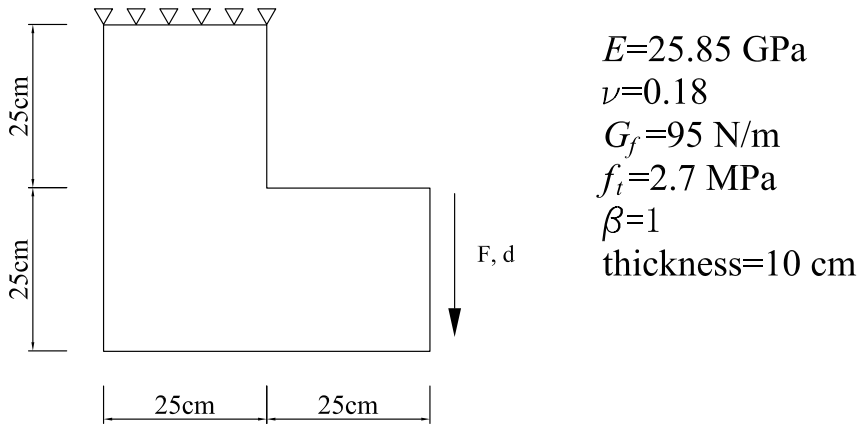

Figure 53: L-shaped panel test: geometric properties and material parameters

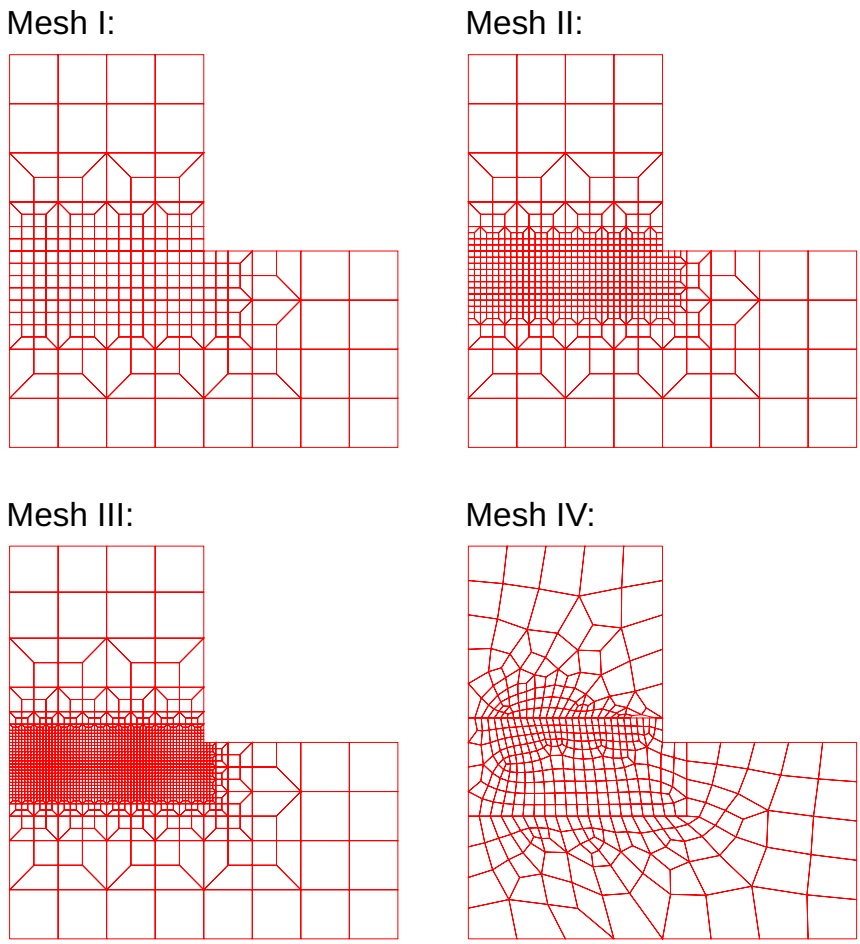

Figure 54: L-shaped panel test: discretizations considered in the numerical investigation

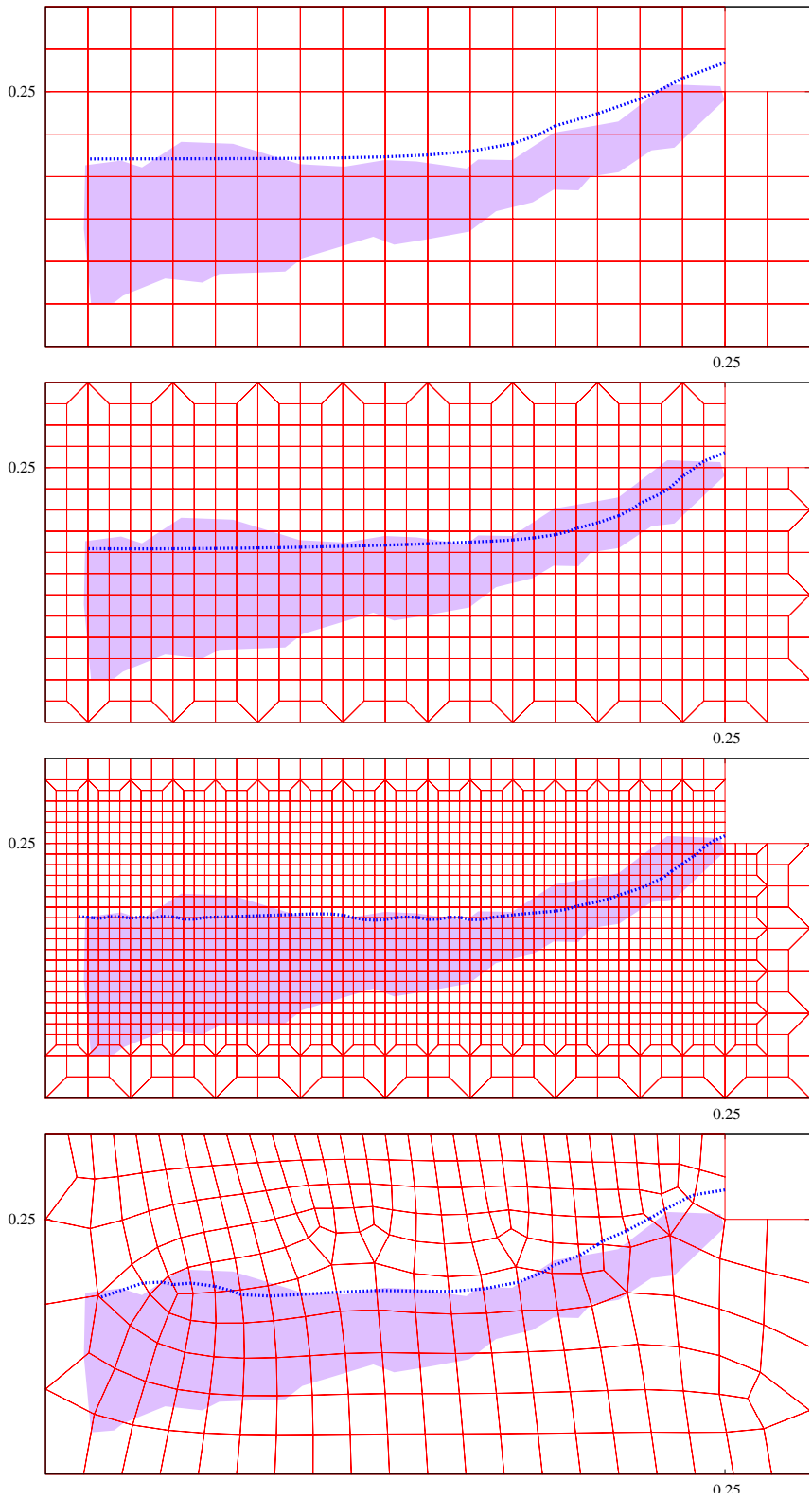

Figure 55: L-shaped panel test: numerically-obtained crack paths and experimental results (grey areas indicate locations of cracks) presented in [125]

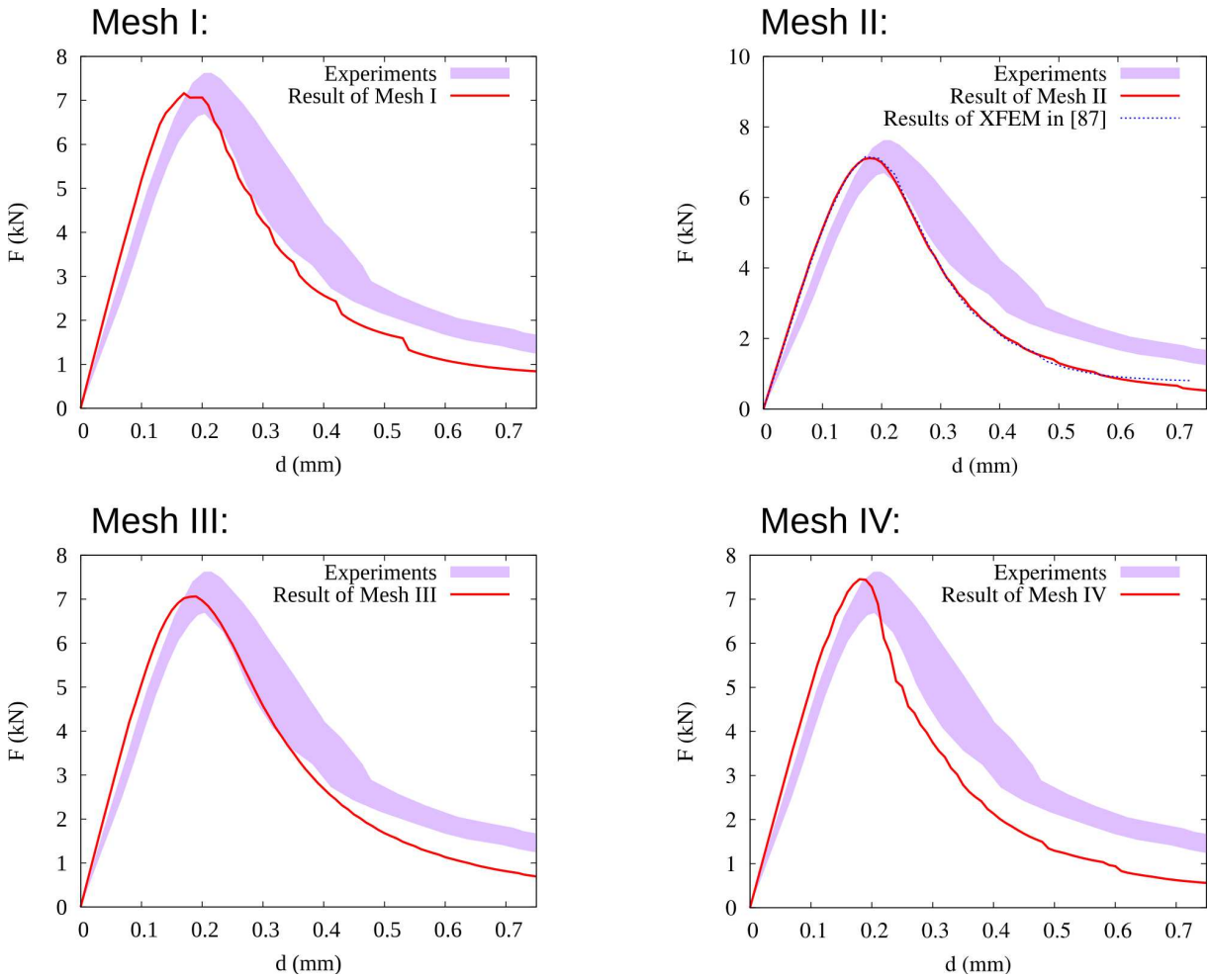

Figure 56: L-shaped panel test: numerically-obtained force-displacement curves and experimental results presented in [125]

4.3.3 Pull-out test

Because of axial symmetry (see Figure 57), the pull-out test can be simulated by a 2D axisymmetric analysis [124]. As pointed out in [124], there are two types of failure modes: tensile failure and compressive failure. However, only tensile failure will be considered in this benchmark example.

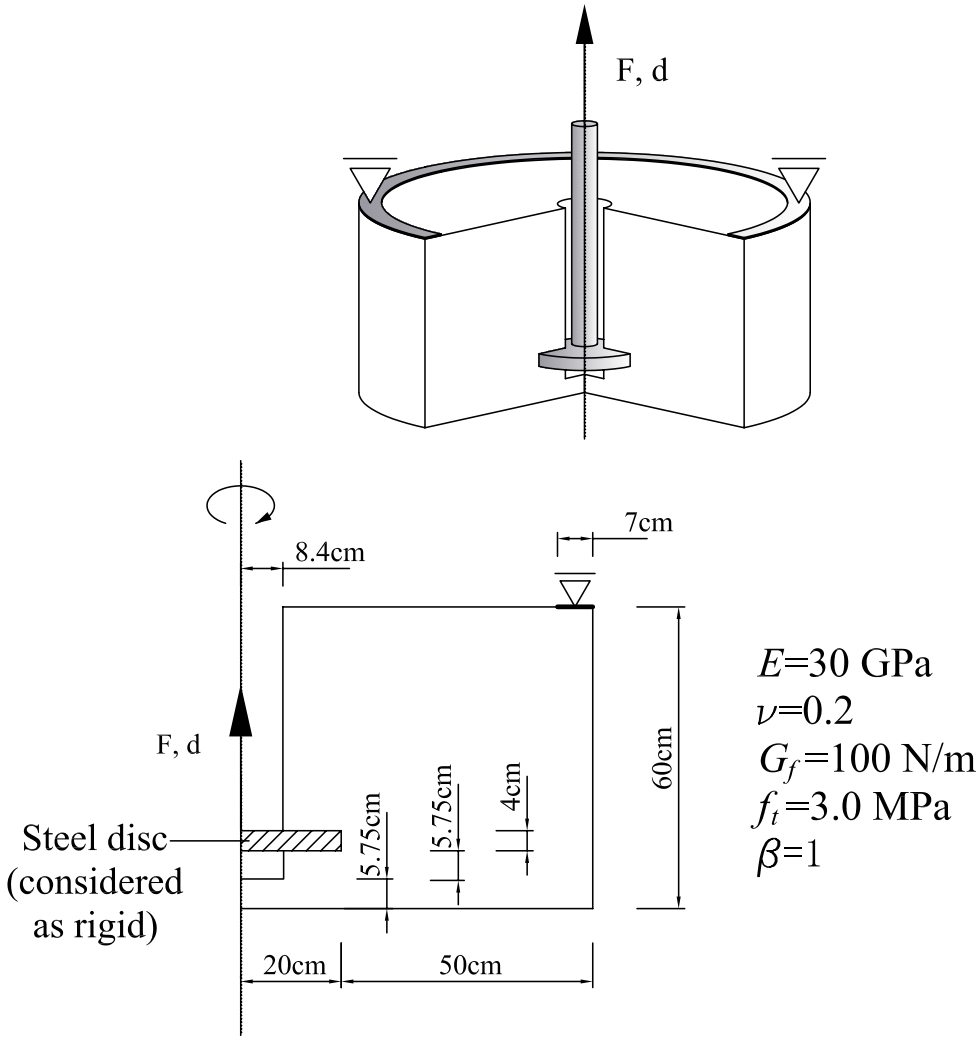

Figure 57: Pull-out test: geometric properties and material parameters

The numerically-obtained crack path and the load-displacement curve are shown in Figures 58 and 59. Consistent with investigations by other authors [90, 126], who considered one quarter of the structure, $F/4$ represents the applied load in the force-displacement curve in Figure 59, showing good agreement between the present results and the ones published in the litera-

ture [90, 126].

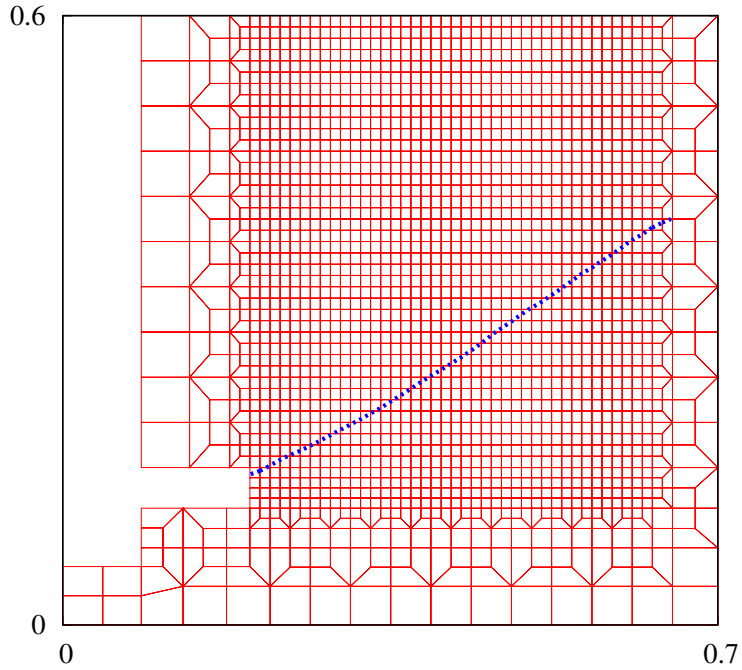

Figure 58: Pull-out test: numerically-obtained crack path

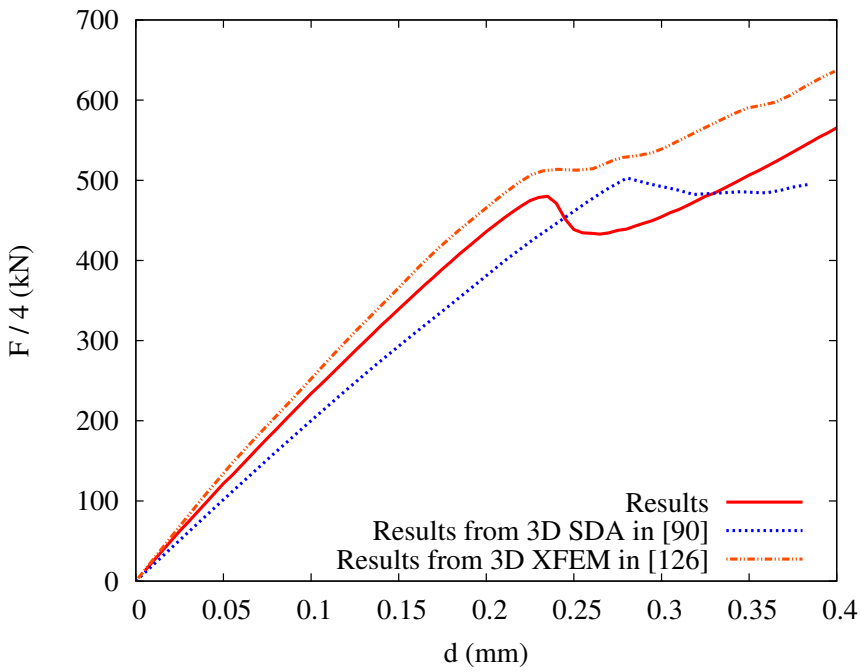

Figure 59: Pull-out test: numerically-obtained force-displacement curve and numerical results reported in [90, 126]

4.3.4 Conclusions

Based on the obtained results from numerical analysis of the three-point bending test, the L-shaped panel test, and the pull-out test, the following conclusion can be drawn:

- The energy-based crack-tracking strategy has shown robustness and reliability, giving continuous crack paths with no mesh bias.
- The SDA framework with the presented crack-tracking strategy resulted in reasonable force-displacement diagrams corresponding well to experimental data and/or numerical results obtained by other investigators. Locking did not occur.

The so-obtained SDA approach, applicable to higher-order elements, is expected to be useful for future applications to coupled displacement-permeation problems, taking fluid flow and pressure redistribution in the course of crack opening into account.

5 Concluding remarks

The assessment of the durability of structures composed of porous materials may require consideration of

- energy transport (thermal loading),
- mass transport (within the pore space of the material) and, finally,
- failure in consequence of mechanical loading (fracture).

In this thesis, the computational framework for these different aspects of durability assessment were presented, employing a multifield analysis framework and a strong-discontinuity approach (SDA), compatible with the multifield analysis framework for proper simulation of cracking within the finite-element method. Moreover, finer-scale information and application of homogenization techniques allowed consideration of changes of the material microstructure in the course of durability assessment. This situation was encountered in the first two applications reported in this thesis, concerning early-age concrete and concrete structures subjected to fire loading. For the assessment of the proposed SDA, different examples with available experimental and/or numerical reference data were analysed. Based on different applications of the proposed computational framework, the following conclusions can be drawn:

- As regards early-age concrete, the obtained results highlighted the coupled thermal shock (temperature difference between the concrete surface and the open air) and moisture shock (difference of moisture content between the concrete surface and the open air) induced by stripping, resulting in shrinkage of early-age concrete. Whereas weakly-coupled analysis (ignoring mass-transport processes) was only capable of simulating the thermal shock and, thus, underestimated the shrinkage stress on the concrete surface, the fully-coupled analysis presented in this thesis captured not only both shocks but also the interaction between them.
- In case of concrete subjected to fire loading, the performed durability assessment of an existing tunnel in Austria showed the significant impact

of the intrinsic permeability on the spalling risk in case of fire loading. In this thesis, based on the developed computational framework, a procedure for the safety assessment of existing tunnels was proposed, combining the exploration of on-site information (water-mass ratio and permeability) and computational methods.

- Finally, for the simulation of concrete fracture, continuous crack paths were obtained in all benchmark problems, with the corresponding force-displacement curves showing no stress locking. The employed energy-based crack tracking strategy increased the robustness of the SDA, with the underlying finite-element formulation applicable to the multifield framework.

The combination of both the SDA and the multiscale-multifield computational framework presented in this thesis is the starting point for future research work, that will deal with the coupling between transport processes and fracturing:

- On one hand, the underlying yield function describing the initiation of fracture may be adopted as

$$\begin{cases} \phi_n = (\mathbf{n} \otimes \mathbf{n}) : [\mathbf{\Sigma} + \mathbf{1}\ \mathrm{b}\,(p^g + \chi\ p^c)] - T_n(\zeta_n, \zeta_t) = 0, \\ \phi_t = (\mathbf{t} \otimes \mathbf{n}) : \mathbf{\Sigma} - T_t(\zeta_n, \zeta_t) = 0, \end{cases} \tag{51}$$

  where p^g and p^c represent the gas and the capillary pressure in the pores.

- On the other hand, the intrinsic permeability of concrete may be increased in case of cracking, with the permeability along the crack direction depending on the crack opening ζ_n [m] [127] (see Figure 60):

$$\begin{cases} \mathrm{k}_n = \mathrm{k}, \\ \mathrm{k}_t = \mathrm{k} \cdot 10^{24000\ \zeta_n}. \end{cases} \tag{52}$$

This coupling is illustrated by means of re-analysis of the L-shaped panel dealt with in this thesis, considering an additional gas-pressure loading at the location of crack initiation (see Figure 61 and Table 8). The so-obtained load-displacement curves and the gas-pressure distributions for different instants

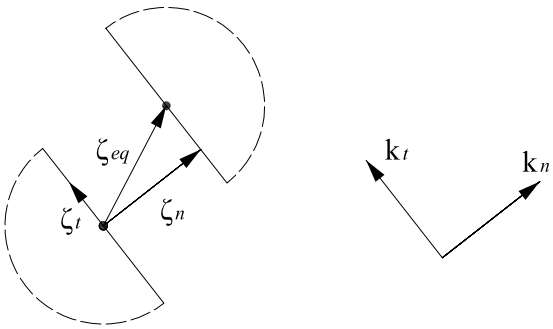

Figure 60: Intrinsic permeability of concrete with crack opening

of loading are shown in Figures 62 and 63. For the case of such loading situations, with the gas pressure contributing to the fracturing process and the opening crack affecting the gas transport, both computational models and experiments for proper validation are still in the initial stage and topics of ongoing and future research.

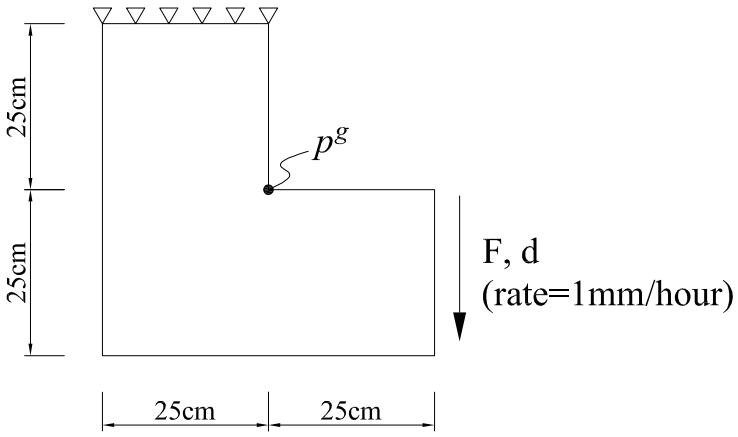

Figure 61: L-shaped panel with gas permeation: geometric properties and gas pressure loading

Table 8: Material parameters

Modulus of elasticity E	(GPa)	25.85
Poisson's ratio ν	(-)	0.18
Tensile strength f_t	(MPa)	2.7
Fracture energy G_f	(N m^{-1})	95
Biot's coefficient b	(-)	0.379
Saturation degree S_w	(-)	0.001
Initial pore pressure p_0^g	(Pa)	101325
Intrinsic permeability $\mathbf{k}$	(m^2)	10^{-17}
Porosity n	(-)	0.1

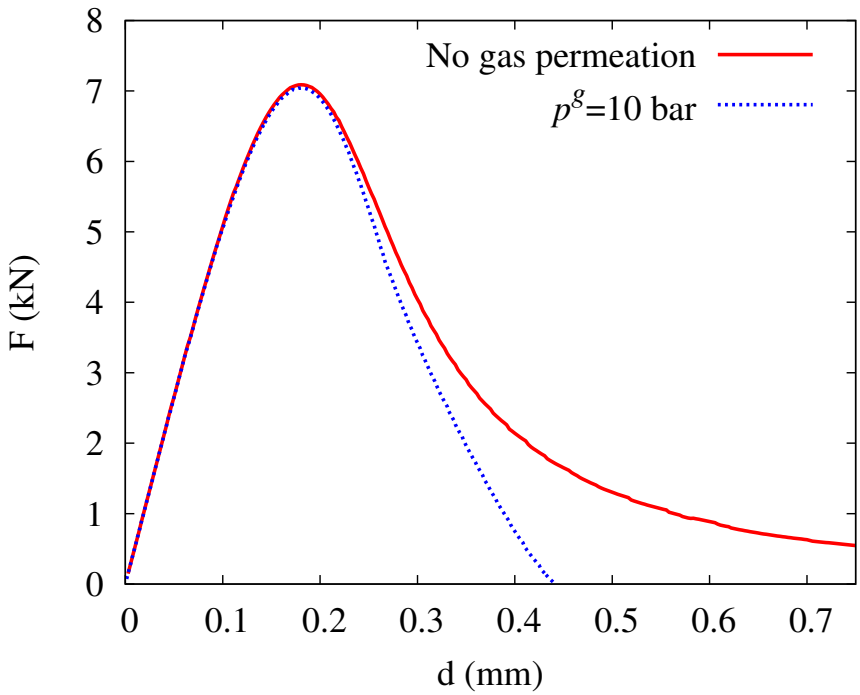

Figure 62: L-shaped panel with gas permeation: force-displacement curves

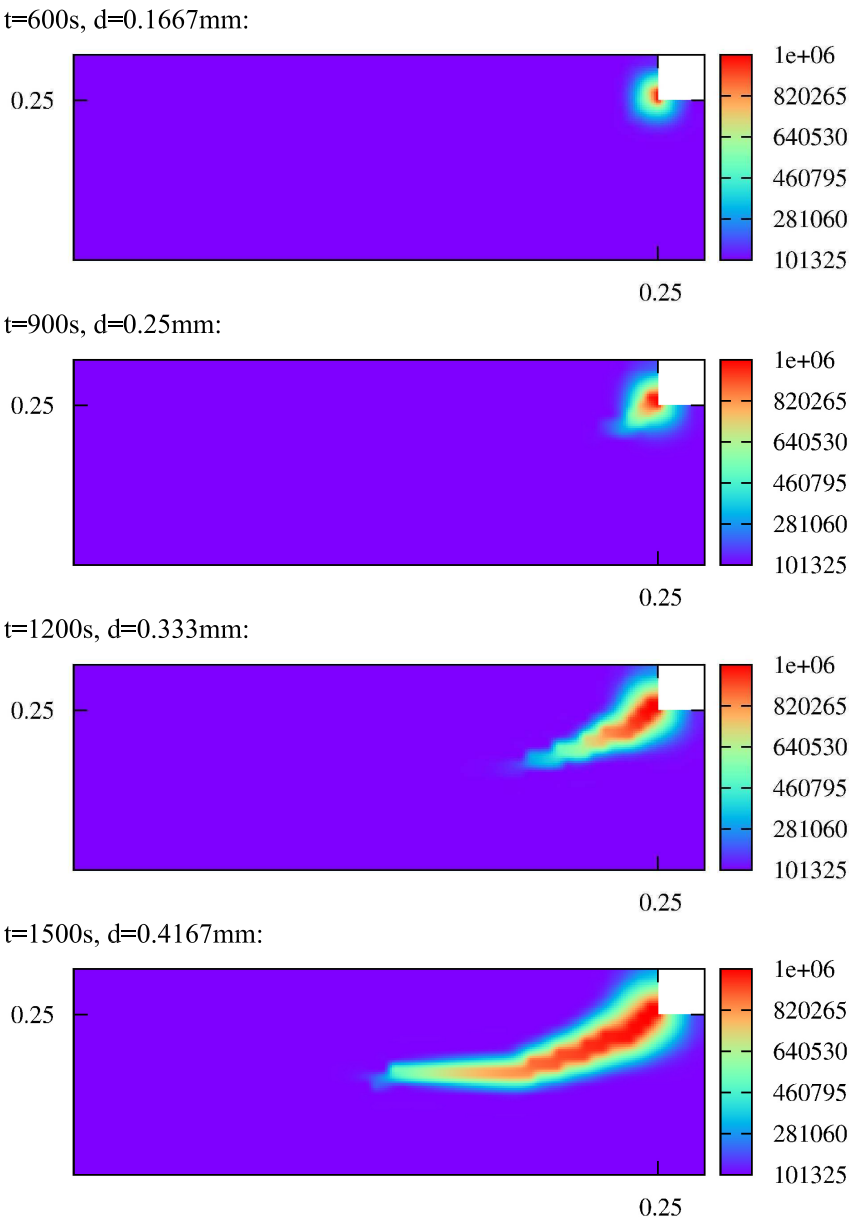

Figure 63: L-shaped panel with gas permeation: evolution of gas pressure (Pa)

6 Bibliography

[1] B. Karihaloo and X. Huang, "Tensile response of quasi-brittle materials," *Pure and Applied Geophysics (pageoph)*, vol. 137, pp. 461–487, 1991.

[2] M. Cervera, J. Oliver, and T. Prato, "Thermo-chemo-mechanical model for concrete I: hydration and aging," *Journal of Engineering Mechanics (ASCE)*, vol. 9, pp. 1018–1027, 1999.

[3] F.-J. Ulm and O. Coussy, "Couplings in early-age concrete: From material modeling to structural design," *International Journal of Solids and Structures*, vol. 35, pp. 4295–4311, 1998.

[4] F.-J. Ulm and O. Coussy, "Modeling of thermo-chemo-mechanical couplings of concrete at early ages," *Journal of Engineering Mechanics (ASCE)*, vol. 7, pp. 785–794, 1995.

[5] Z. Bazănt and L. Najjar, "Nonlinear water diffusion in nonsaturated concrete," *Materials and Structures*, vol. 25, pp. 3–20, 1972.

[6] T. Ishida, K. Maekawa, and T. Kishi, "Enhanced modeling of moisture equilibrium and transport in cementitious materials under arbitrary temperature and relative humidity history," *Cement and Concrete Research*, vol. 4, pp. 565–578, 2007.

[7] V. Baroghel-Bouny, M. Mainguy, T. Lassabatere, and O. Coussy, "Characterization and identification of equilibrium and transfer moisture properties for ordinary and high-performance cementitious materials," *Cement and Concrete Research*, vol. 29, pp. 1225–1238, 1999.

[8] B. Schrefler and D. Gawin, "The effective stress principle: Incremental or finite form?," *International Journal for Numerical and Analytical Methods in Geomechanics*, vol. 20, pp. 785–814, 1996.

[9] D. Gawin, F. Pesavento, and B. Schrefler, "Hygro-thermo-chemo-mechanical modelling of concrete at early ages and beyond. Part II:

shrinkage and creep of concrete," *International Journal for Numerical Methods in Engineering*, vol. 67, pp. 332–363, 2006.

[10] Y. Yuan and Z. Wan, "Prediction of cracking within early-age concrete due to thermal, drying and creep behavior," *Cement and Concrete Research*, vol. 7, pp. 1053–1059, 2002.

[11] D. Gawin, F. Pesavento, and B. Schrefler, "Hygro-thermo-chemo-mechanical modelling of concrete at early ages and beyond. Part I: hydration and hygro-thermal phenomena," *International Journal for Numerical Methods in Engineering*, vol. 67, pp. 299–331, 2006.

[12] F.-J. Ulm and O. Coussy, "What is a "massive" concrete structure at early ages? Some dimensional arguments," *Journal of Engineering Mechanics (ASCE)*, vol. 5, pp. 512–522, 2001.

[13] Z. Bazănt, "Analysis of Pore Pressure, Thermal Stress and Fracture in Rapidly Heated Concrete," in *Proceedings of the International Workshop on Fire Performance of High-Strength Concrete* (L. Phan, N. Carino, D. Duthinh, and E. Garboczi, eds.), (Gaithersburg, Maryland), pp. 155–164, 1997.

[14] F.-J. Ulm, O. Coussy, and Z. Bazănt, "The "Chunnel" fire I: chemo-plastic softening in rapidly heated concrete," *Journal of Engineering Mechanics (ASCE)*, vol. 125, pp. 272–282, 1999.

[15] Z. Bazănt and G. Zi, "Pore pressure and drying of concrete at high temperature," *Journal of the Engineering Mechanics Division*, vol. 104, pp. 1059–1079, 1978.

[16] Y. Anderberg, "Spalling phenomena in HPC and OC," in *Proceedings of the International Workshop on Fire Performance of High-Strength Concrete* (L. Phan, N. Carino, D. Duthinh, and E. Garboczi, eds.), (Gaithersburg, Maryland), pp. 69–73, 1997.

[17] P. Kalifa, F.-D. Menneteau, and D. Quenard, "Spalling and pore pressure in HPC at high temperatures," *Cement and Concrete Research*, vol. 30, pp. 1915–1927, 2000.

[18] F.-J. Ulm, P. Acker, and M. Lévy, "The "Chunnel" fire II: analysis of concrete damage," *Journal of Engineering Mechanics (ASCE)*, vol. 125, pp. 283–289, 1999.

[19] A. Abdel-Rahman and G. Ahmed, "Computational heat and mass transport in concrete walls exposed to fire," *Numerical Heat Transfer, Part A: Applications*, vol. 29, pp. 373–395, 1996.

[20] R. Tenchev, L. Li, and J. Purkiss, "Finite element analysis of coupled heat and moisture transfer in concrete subjected to fire," *Numerical Heat Transfer, Part A: Applications*, vol. 39, pp. 685–710, 2001.

[21] Y. Ichikawa and G. England, "Prediction of moisture migration and pore pressure build-up in concrete at high temperatures," *Nuclear Engineering and Design*, vol. 228, pp. 245–259, 2004.

[22] R. Tenchev and P. Purnell, "An application of a damage constitutive model to concrete at high temperature and prediction of spalling," *International Journal of Solids and Structures*, vol. 42, pp. 6550–6565, 2005.

[23] J. H. Chung, G. Consolazio, and M. McVay, "Finite element stress analysis of a reinforced high-strength concrete column in severe fires," *Computers and Structures*, vol. 84, pp. 1338–1352, 2006.

[24] D. Gawin, F. Pesavento, and B. Schrefler, "Comments to the paper ''An application of a damage constitutive model to concrete at high temperature and prediction of spalling'' by Rosen Tenchev and Phil Purnell," *International Journal of Solids and Structures*, vol. 44, pp. 4234–4237, 2007.

[25] D. Gawin and B. Schrefler, "Thermo-hydro-mechanical analysis of partially saturated porous materials," *Engineering Computations*, vol. 13, pp. 113–143, 1996.

[26] B. Schrefler, C. Majorana, G. Khoury, and D. Gawin, "Thermo-hydro-mechanical modelling of high performance concrete at high temperatures," *Engineering Computations*, vol. 19, pp. 787–819, 2002.

[27] B. Schrefler, "Multiphase flow in deforming porous material," *International Journal for Numerical Methods in Engineering*, vol. 60, pp. 27–50, 2004.

[28] D. Gawin, F. Pesavento, and B. Schrefler, "Towards prediction of the thermal spalling risk through a multi-phase porous media model of concrete," *Computer Methods in Applied Mechanics and Engineering*, vol. 195, pp. 5707–5729, 2006.

[29] D. Gawin, F. Pesavento, and B. Schrefler, "Modelling of hygro-thermal behaviour of concrete at high temperature with thermo-chemical and mechanical material degradation," *Computer Methods in Applied Mechanics and Engineering*, vol. 192, pp. 1731–1771, 2003.

[30] F. Pesavento, *Non-linear modelling of concrete as multiphase porous material in high temperature conditions.* PhD thesis, University of Padua, Italy, 2000.

[31] M. Zeiml, *Concrete subjected to fire loading — From experimental investigation of spalling and mass-transport properties to structural safety assessment of tunnel linings under fire.* PhD thesis, Vienna University of Technology, Austria, 2008.

[32] F.-J. Ulm and O. Coussy, "Strength growth as chemo-plastic hardening in early age concrete," *Journal of Engineering Mechanics (ASCE)*, vol. 12, pp. 1123–1132, 1996.

[33] R. Lackner and H. A. Mang, "Chemoplastic material model for the simulation of early-age cracking: From the constitutive law to numerical analyses of massive concrete structures," *Cement&Concrete Composites*, vol. 26, pp. 551–562, 2004.

[34] P. Tennis and H. Jennings, "A model for two types of calcium silicate hydrate in the microstructure of Portland cement pastes," *Cement and Concrete Research*, vol. 30, pp. 855–863, 2000.

[35] F.-J. Ulm, G. Constantinides, and F. Heukamp, "Is concrete a poromechanics material?—A multiscale investigation of poroelastic properties," *Materials and Structures*, vol. 37, pp. 43–58, 2004.

[36] C. Pichler, R. Lackner, and H. Mang, "A multiscale micromechanics model for the autogenous-shrinkage deformation of early-age cement-based materials," *Engineering Fracture Mechanics*, vol. 74, pp. 34–58, 2007.

[37] T. Mori and K. Tanaka, "Average stress in matrix and average elastic energy of materials with misfitting inclusions," *Acta Metallurgica*, vol. 21, pp. 571–574, 1973.

[38] A. Zaoui, "Structural morphology and constitutive behaviour of micro-heterogeneous materials," in *Continuum micromechanics* (P. Suquet, ed.), Springer, 1997.

[39] L. Dormieux and E. Lemarchand, "Homogenization approach of advection and diffusion in cracked porous material," *Journal of Engineering Mechanics (ASCE)*, vol. 127, pp. 1267–1274, 2001.

[40] C. Pichler, G. Metzler, C. Niederegger, and R. Lackner, "Thermo-mechanical optimization of porous building materials based on micromechanical concepts: Application to load-carrying insulation materials," *Composites: Part B*, vol. 43, pp. 1015–1023, 2012.

[41] A. Hershey, "The elasticity of an isotropic aggregate of anisotropic cubic crystals," *Journal of Applied Mechanics*, vol. 21, pp. 236–240, 1954.

[42] E. Kroener, "Berechnung der elastischen Konstanten des Vielkristalls aus den Konstanten des Einkristalls [Computation of the elastic constants of a polycrystal based on the constants of the single crystal]," *Zeitschrift für Physik*, vol. 151, pp. 504–518, 1958.

[43] D. Gross and T. Seelig, *Bruchmechanik, mit einer Einfuhrung in die Mikromechanik [Fracture mechanics, containing an introduction to continuum micromechanics].* Springer, 2001.

[44] O. Bernard, F.-J. Ulm, and E. Lemarchand, "A multiscale micromechanics-hydration model for the early-age elastic properties of cement-based materials," *Cement and Concrete Research*, vol. 33, pp. 1293–1309, 2003.

[45] D. Bentz, "Transient plane source measurements of the thermal properties of hydrating cement pastes," *Materials and Structures*, vol. 40, pp. 1073–1080, 2007.

[46] C. Pichler, "Numerical simulation of tunnels accounting for thermochemomechanical couplings: assessment of the benefits from ground improvement by means of jet grouting and of the loading of tunnel linings under fire exposure," Master's thesis, Vienna University of Technology, 2002.

[47] I. Vlahinic, H. Jennings, J. Andrade, and J. Thomas, "A novel and general form of effective stress in a partially saturated porous material: The influence of microstructure," *Mechanics of Materials*, vol. 43, pp. 25–35, 2011.

[48] D. Gawin, F. Pesavento, and B. Schrefler, "Modelling of deformations of high strength concrete at elevated temperatures," *Materials and Structures*, vol. 37, pp. 218–236, 2004.

[49] S. Thelandersson, "Modeling of combined thermal and mechanical action in concrete," *Journal of Engineering Mechanics (ASCE)*, vol. 113, pp. 893–906, 1987.

[50] T. Ring, M. Zeiml, R. Lackner, and J. Eberhardsteiner, "Experimental investigation of strain behavior of heated cement paste and concrete," *Strain*, vol. 49, pp. 249–256, 2013.

[51] T. Ring, M. Zeiml, and R. Lackner, "Underground concrete frame structures subjected to fire loading: PartII – Re-analysis of large-scale fire tests," *Engineering Structures*, In Press 2012.

[52] D. Ngo and A. Scordelis, "Finite element analysis of reinforced concrete beams," *Journal of American Concrete Institute*, vol. 64, pp. 152–163, 1967.

[53] Y. Rashid, "Ultimate strength analysis of prestressed concrete pressure vessels," *Nuclear Engineering and Design*, vol. 7, pp. 334–344, 1968.

[54] R. Goodman, R. Taylor, and T. Brekke, "A model for the mechanics of jointed rock," *Journal of the Soil Mechanics and Foundations Division (ASCE)*, vol. 99, pp. 637–660, 1968.

[55] L. Herrmann, "Finite element analysis of contact problems," *Journal of Engineering Mechanics (ASCE)*, vol. 104, pp. 1043–1059, 1978.

[56] P. Feenstra and R. Borst, "A plasticity model and algorithm for Mode-I cracking in concrete," *International Journal for Numerical Methods in Engineering*, vol. 38, pp. 2509–2529, 1995.

[57] A. Ingraffea and V. Saouma, "Numerical modelling of discrete crack propagation in reinforced and plain concrete," in *Fracture Mechanics of Concrete* (G. C. Sih and A. Ditomasso, eds.), pp. 171–225, Dordrecht: Martinus Nijhoff, 1985.

[58] N. Sukumar, N. Moes, B. Moran, and T. Belytschko, "Extended finite element method for three-dimensional crack modelling," *International Journal for Numerical Methods in Engineering*, vol. 48, pp. 1549–1570, 2000.

[59] J. Melenk and I. Babuska, "The partition of unity finite element method: Basic theory and applications," *Computer Methods in Applied Mechanics and Engineering*, vol. 139, pp. 289–314, 1996.

[60] M. Jirásek, "Computational Resolution of Strong Discontinuities," in *Fifth World Congress on Computational Mechanics (WCCM V)* (H. Mang, F. Rammerstorfer, and J. Eberhardsteiner, eds.), Vienna University of Technology, 2002.

[61] R. I. Borja, "Assumed enhanced strain and the extended finite element methods: A unification of concepts," *Computer Methods in Applied Mechanics and Engineering*, vol. 197, pp. 2789–2803, 2008.

[62] J. Oliver, A. Huespe, and P. Sanchez, "A comparative study on finite elements for capturing strong discontinuities E-FEM vs X-FEM," *Computer Methods in Applied Mechanics and Engineering*, vol. 195, pp. 4732–4752, 2006.

[63] C. Johnson and R. Scott, "A Finite Element Method for Problems in Perfect Plasticity Using Discontinuous Trial Functions," in *Nonlinear finite element analysis in structural mechanics* (W. Wunderlich, E. Stein, and K.-J. Bathe, eds.), pp. 307–324, Springer, 1981.

[64] E. N. Dvorkin, A. M. Cuitino, and G. Gioia, "Finite Elements with Displacement Interpolated Embedded Localization Lines Insensitive to Mesh Size and Distortions," *International Journal for Numerical Methods in Engineering*, vol. 30, pp. 541–564, 1990.

[65] E. N. Dvorkin and A. P. Assanelli, "2D finite elements with displacement interpolated embedded localization lines: The analysis of fracture in frictional materials," *Computer Methods in Applied Mechanics and Engineering*, vol. 90, pp. 829–844, 1991.

[66] M. Klisinski, K. Runesson, and S. Sture, "Finite element with inner softening band," *Journal of Engineering Mechanics (ASCE)*, vol. 117, pp. 575–587, 1991.

[67] T. Belytschko, J. Fish, and B. E. Engelmann, "A Finite element with embedded localization zones," *Computer Methods in Applied Mechanics and Engineering*, vol. 70, pp. 59–89, 1988.

[68] J. Simo and S. Rifai, "A class of mixed assumed strain methods and the method of incompatible modes," *International Journal for Numerical Methods in Engineering*, vol. 29, pp. 1595–1638, 1990.

[69] J. Simo, J. Oliver, and F. Armero, "An analysis of strong discontinuities induced by strain-softening in rate-independent inelastic solids," *Computational Mechanics*, vol. 12, pp. 277–296, 1993.

[70] J. Simo and F. Armero, "Geometrically non-linear enhanced strain mixed methods and the method of incompatible modes," *International Journal for Numerical Methods in Engineering*, vol. 33, pp. 1413–1449, 1992.

[71] J. Oliver, "Modelling strong discontinuities in solid mechanics via strain softening constitutive equations. Part I: Fundamentals," *International*

Journal for Numerical Methods in Engineering, vol. 39, pp. 3575–3600, 1996.

[72] H. Horii and T. Ichinomiya, "Observation of fracture process zone by laser speckle technique and governing mechanism in fracture of concrete," *International Journal for Fracture*, vol. 51, pp. 19–29, 1991.

[73] F. Wittmann and X. Hu, "Fracture process zone in cementitious materials," *International Journal of Fracture*, vol. 51, pp. 3–18, 1991.

[74] K. Otsuka and H. Date, "Fracture process zone in concrete tension specimen," *Engineering Fracture Mechanics*, vol. 65, pp. 111–131, 2000.

[75] J. Oliver, M. Cervera, and O. Manzoli, "Strong discontinuities and continuum plasticity models: the strong discontinuity approach," *International Journal of Plasticity*, vol. 15, pp. 319–351, 1999.

[76] M. Jirásek and T. Zimmermann, "Embedded crack model: I. Basic formulation," *International Journal for Numerical Methods in Engineering*, vol. 50, pp. 1269–1290, 2001.

[77] J. Mosler, "On advanced solution strategies to overcome locking effects in strong discontinuity approaches," *International Journal for Numerical Methods in Engineering*, vol. 63, pp. 1313–1341, 2005.

[78] J. Mosler and G. Meschke, "3D modelling of strong discontinuities in elastoplastic solids: fixed and rotating localization formulations," *International Journal for Numerical Methods in Engineering*, vol. 57, pp. 1553–1576, 2003.

[79] R. Radulovic, O. Bruhns, and J. Mosler, "Effect 3D failure simulations by combining the advantages of embedded strong discontinuity approaches and classical interface elements," *Engineering Fracture Mechanics*, vol. 78, pp. 2470–2485, 2011.

[80] M. Jirásek and T. Zimmermann, "Embedded crack model: II. Combination with smeared cracks," *International Journal for Numerical Methods in Engineering*, vol. 50, pp. 1291–1305, 2001.

[81] Y. Theiner and G. Hofstetter, "Numerical prediction of crack propagation and crack widths in concrete structures," *Engineering Structures*, vol. 31, pp. 1832–1840, 2009.

[82] J. Oliver, A. Huespe, E. Samaniego, and E. Chaves, "On strategies for tracking strong discontinuities in computational failure mechanics," in *Fifth World Congress on Computational Mechanics (WCCM V)* (H. Mang, F. Rammerstorfer, and J. Eberhardsteiner, eds.), 2002.

[83] P. Dumstorff and G. Meschke, "Crack propagation criteria in the framework of X-FEM-based structural analyses," *International Journal for Numerical and Analytical Methods in Geomechanics*, vol. 31, pp. 239–259, 2007.

[84] J. Sancho, J. Planas, D. Cendón, E. Reyes, and J. Gálvez, "An embedded crack model for finite element analysis of concrete fracture," *Engineering Fracture Mechanics*, vol. 74, pp. 75–86, 2007.

[85] M. Cervera, L. Pela, R. Clemente, and P. Roca, "A crack-tracking technique for localized damage in quasi-brittle materials," *Engineering Fracture Mechanics*, vol. 77, pp. 2431–2450, 2010.

[86] J. Oliver and A. Huespe, "Theoretical and computational issues in modelling material failure in strong discontinuity scenarios," *Computer Methods in Applied Mechanics and Engineering*, vol. 193, pp. 2987–3014, 2004.

[87] G. Meschke and P. Dumstorff, "Energy-based modeling of cohesive and cohesionless cracks via X-FEM," *Computer Methods in Applied Mechanics and Engineering*, vol. 196, pp. 2338–2357, 2007.

[88] C. Feist and G. Hofstetter, "An embedded strong discontinuity model for cracking of plain concrete," *Computer Methods in Applied Mechanics and Engineering*, vol. 195, pp. 7115–7138, 2006.

[89] C. Feist, *A Numerical Model for Cracking of Plain Concrete Based on the Strong Discontinuity Approach*. PhD thesis, University of Innsbruck, 2004.

[90] C. Feist and G. Hofstetter, "Three-dimensional fracture simulations based on the SDA," *International Journal for Numerical and Analytical Methods in Geomechanics*, vol. 31, pp. 189–212, 2007.

[91] J. Oliver, "A consistent characteristic length for smeared cracking models," *International Journal for Numerical Methods in Engineering*, vol. 28, pp. 461–474, 1989.

[92] G. Camacho and M. Ortiz, "Computational modelling of impact damage in brittle materials," *International Journal of Solids and Structures*, vol. 33, pp. 2899–2938, 1996.

[93] S. Mariani and U. Perego, "Extended finite element method for quasi-brittle fracture," *International Journal for Numerical Methods in Engineering*, vol. 58, pp. 103–126, 2003.

[94] T. Belytschko, D. Organ, and C. Gerlach, "Element-free Galerkin methods for dynamic fracture in concrete," *Computer Methods in Applied Mechanics and Engineering*, vol. 187, pp. 385–399, 2000.

[95] J. Simo and T. Hughes, *Computational Inelasticity*, vol. 7. Springer, 1998.

[96] R. I. Borja, "A finite element model for strain localization analysis of strongly discontinuous fields based on standard Galerkin approximation," *Computer Methods in Applied Mechanics and Engineering*, vol. 190, pp. 1529–1549, 2000.

[97] J. Mosler and G. Meschke, "Analysis of mode I failure in brittle materials using the strong discontinuity approach with higher order elements," in *European Congress on Computational Mechanics*, 2001.

[98] G. Meschke and P. Dumstorff, "How does the crack know where to propagate? - A X-FEM-based study on crack propagation criteria," in *Nonlocal modelling of Failure of Materials*, pp. 201–218, Proceeding of an International Workshop (Nonlocal Modeling of Material's Failure, NMMF 2007), 2007.

[99] J. F. Unger, S. Eckardt, and C. Könke, "Modelling of cohesive crack growth in concrete structures with the extended finite element method," *Computer Methods in Applied Mechanics and Engineering*, vol. 196, pp. 4087–4100, 2007.

[100] P. Jäger, P. Steinmann, and E. Kuhl, "Modeling three-dimensional crack propagation - A comparison of crack path tracking strategies," *International Journal for Numerical Methods in Engineering*, vol. 76, pp. 1328–1352, 2008.

[101] J. Oliver and A. Huespe, "Continuum approach to material failure in strong discontinuity settings," *Computer Methods in Applied Mechanics and Engineering*, vol. 193, pp. 3195–3220, 2004.

[102] M. Stolarska, D. Chopp, N. Moes, and T. Belytschko, "Modelling crack growth by level sets in the extended finite element method," *International Journal for Numerical Methods in Engineering*, vol. 51, pp. 943–960, 2001.

[103] M. Xie and W. Gerstle, "Energy-based cohesive crack propagation modeling," *Journal of Engineering Mechanics (ASCE)*, vol. 121, pp. 1349–1358, 1995.

[104] M. Jirásek, "Comparative study on finite elements with embedded discontinuities ," *Computer Methods in Applied Mechanics and Engineering*, vol. 188, pp. 307–330, 2000.

[105] T. C. Gasser and G. A. Holzapfel, "Geometrically non-linear and consistently linearized embedded strong discontinuity models for 3D problems with an application to the dissection analysis of soft biological tissues," *Computer Methods in Applied Mechanics and Engineering*, vol. 192, pp. 5059–5098, 2003.

[106] J. Mosler and G. Meschke, "Embedded crack vs. smeared crack models: a comparison of elementwise discontinuous crack path approaches with emphasis on mesh bias," *Computer Methods in Applied Mechanics and Engineering*, vol. 193, pp. 3351–3375, 2004.

[107] European Committee for Standardization (CEN), *Eurocode 2 – Bemessung und Konstruktion von Stahlbeton- und Spannbetontragwerken – Teil 1-1: Allgemeine Bemessungsregeln und Regeln für den Hochbau [Eurocode 2 – Design of reinforced and prestressed concrete structures – Part 1-1: General rules for design and rules for building constructures] (in German)*, 2009.

[108] B. Pichler and C. Hellmich, "Upscaling quasi-brittle strength of cement paste and mortar: A multi-scale engineering mechanics model," *Cement and Concrete Research*, vol. 41, pp. 467–476, 2011.

[109] D. Bentz and P. Stutzman, *SEM analysis and computer modelling of hydration of Portland cement particles.* ASTM STP 1215: Petrography of Cementitious Materials, 1994.

[110] G. Khoury and C. Majorana, "Effect of Heat on Concrete," (Udine), International Centre for Mechanical Science, 2003.

[111] C. A. Menzel, "Causes and prevention of crack development in plastic concrete," in *Proceedings of the Portland Cement Association*, pp. 130–136, 1954.

[112] P. Uno, "Plastic shrinkage cracking and evaporation formulas," *ACI Materials Journal*, vol. 95, pp. 365–375, 1998.

[113] M. Al-Fadhala and K. C. Hover, "Rapid evaporation from freshly cast concrete and the Gulf environment," *Construction and Building Materials*, vol. 15, pp. 1–7, 2001.

[114] A. A. Almusallam, "Effect of environmental conditions on the properties of fresh and hardened concrete," *Cement&Concrete Composites*, vol. 23, pp. 353–361, 2001.

[115] ACI 305R-96, "Hot Weather Concreting," *Manual of Concrete Practice, Part 2.*, 1996.

[116] K.-C. Thienel and F. Rostasy, "Strength of concrete subjected to high temperature and biaxial stress: Experiments and modelling," *Materials and Structures*, vol. 28, pp. 575–581, 1995.

[117] Z. He and Y. Song, "Failure mode and constitutive model of plain high-strength high-performance concrete under biaxial compression after exposure to high temperatures," *Acta Mechanica Solida Sinica*, vol. 21, pp. 149–159, 2008.

[118] T. Ring, M. Zeiml, and R. Lackner, "Underground concrete frame structures subjected to fire loading: Part I – Large-scale fire tests," *Engineering Structures*, In Press 2012.

[119] European Committee for Standardization (CEN), *Eurocode 2 – Bemessung und Konstruktion von Stahlbeton- und Spannbetontragwerken – Teil 1-2: Allgemeine Regeln – Tragwerksbemessung für den Brandfall [Eurocode 2 – Design of reinforced and prestressed concrete structures – Part 1-2: General rules – Structural fire design] (in German)*, 2007.

[120] M. Zeiml, D. Leithner, R. Lackner, and H. Mang, "How do polypropylene fibers improve the spalling behavior of in-situ concrete," *Cement and Concrete Research*, vol. 36, pp. 929–942, 2006.

[121] L. Didier and H. Alfred, "PIARAC design criteria for resistance to fire for road tunnel structures," *Magazine of routes/roads from PIARC*, vol. 10, pp. 64–71, 2004.

[122] J.-H. J. Kim, Y. M. Lim, J. P. Won, and H. G. Park, "Fire resistant behavior of newly developed bottom-ash-based cementitious coating applied concrete tunnel lining under RABT fire loading," *Construction and Building Materials*, vol. 24, pp. 1984–1994, 2010.

[123] M. Zeiml, R. Lackner, D. Leithner, and J. Eberhardsteiner, "Identification of residual gas-transport properties of concrete subjected to high temperatures," *Cement and Concrete Research*, vol. 38, pp. 699–716, 2008.

[124] J. Rots, *Computational Modeling of Concrete Fracture.* PhD thesis, Delft University of Technology, 1988.

[125] B. Winkler, *Traglastuntersuchungen von unbewehrten und bewehrten Betonstrukturen auf der Grundlage eines objektiven Werkstoffgesetzes für Beton.* PhD thesis, University of Innsbruck, 2001.

[126] T. C. Gasser and G. A. Holzapfel, "Modeling 3D crack propagation in unreinforced concrete using PUFEM," *Computer Methods in Applied Mechanics and Engineering*, pp. 2859–2896, 2005.

[127] V. Picandet, A. Khelidj, and H. Bellegou, "Crack effects on gas and water permeability of concretes," *Cement and Concrete Research*, vol. 39, pp. 537–547, 2009.

Curriculum Vitae

Personal Data

Name:	Yiming ZHANG
Gender:	male
Place/Date of Birth:	Shanghai, June 5, 1984

Education

2002-2006	Diploma studies in Civil Engineering, Tongji University, Shanghai, China
2006-2009	Master studies in Structure Engineering, Tongji University, Shanghai, China
2009-2013	Doctoral studies at Vienna University of Technology, Austria, Dissertation at the Institute for Mechanics of Materials and Structures and since May 2013, studies at University of Innsbruck

Presentations

June, 2011 "Minimizing Drying-shrinkage Cracking within the Production Process and Its Effect on the Working Process of Tunnel Segments", International Conference on Computational Modeling of Fracture and Failure of Materials and Structures (CFRAC 2011)

April, 2012 "Spalling Risk Assessment of Concrete Subjected to Different Fire Scenarios", Microdurability 2012

July, 2013 "A Coupled Thermo-Hygro-Chemo-Mechanical Model for The Simulation of Spalling of Concrete Subjected to Fire Loading", 5th BIOT Conference on Poromechanics (BIOT-5)

Publications

[1] Y. Zhang, R. Lackner, M. Zeiml, and H. Mang, "Spalling risk assessment of concrete subjected to different fire scenarios," in Proceedings of the Second International Conference on Microstructural-related Durability of Cementitious Composites (G. Ye, K. Breugel, W. Sun, and C. Mia, eds.), CD-Rom, Paper number 217, RILEM, 2012.

[2] Y. Zhang, M. Zeiml, C. Pichler, R. Lackner, and H. Mang, "A coupled thermo-hygro-chemo-mechanical model for the simulation of spalling of concrete subjected to fire loading," in Poromechanics V (C. Hellmich, B. Pichler, and D. Adam, eds.), pp. 2113-2122, 2013.

[3] Y. Zhang, C. Pichler, Y. Yuan, M. Zeiml, and R. Lackner, "Micromechanics-based multifield framework for early-age concrete," Engineering Structures, vol. 47, pp. 16-24, 2013.